Dielectric and Magnetic Material Characterization Techniques up to 1,5 THz

M.P. Bezhko

Keysight Technologies, Moscow, Russia, mikhail.bezhko@keysight.com

Abstract

Every material has a unique set of electrical characteristics that are dependent on its dielectric properties. Accurate measurements of these properties can provide scientists and engineers with valuable information to properly incorporate the material into its intended application.

In this report a short overview of variety of methods, instruments and fixtures to measure the dielectric properties of materials in broad frequency range up to 1,5 THz is presented.

Introduction

A wide variety of industries need a better understanding of the materials they are working with to shorten design cycles, improve incoming inspection, process monitoring, and quality assurance. Every material has a unique set of electrical characteristics that are dependent on its dielectric properties. Accurate measurements of these properties can provide scientists and engineers with valuable information to properly incorporate the material into its intended application for more solid designs or to monitor a manufacturing process for improved quality control.

A dielectric materials measurement can provide critical design parameter information for many electronics applications. For example, the loss of a cable insulator, the impedance of a substrate, or the frequency of a dielectric resonator can be related to its dielectric properties. The information is also useful for improving ferrite, absorber and packaging designs. More recent applications in the area of aerospace, automotive, food and medical industries have also been found to benefit from knowledge of dielectric properties.

Keysight Technologies, Inc. offers a variety of instruments, fixtures, and software to measure the dielectric properties of materials. Keysight measurement instruments, such as network analyzers, impedance analyzers and LCR meters range in frequency up to 1.5 THz. Fixtures to hold the material under test (MUT) are available that are based on coaxial probe, parallel plate, coaxial/waveguide transmission lines, free space and resonant cavity methods. In this report a short overview of measurement techniques, instruments and fixtures to measure the dielectric properties of materials in broad frequency range up to 1,5 THz is presented. Detailed description of measurement techniques and fixtures were presented in Keysight literature [1, 2, 3, 4].

Measurement techniques

There are several measurement techniques that exist for measuring dielectric properties of materials, most frequently used methods are presented in Fig.1.
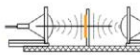

Fig.1. Materials measurement techniques

Transmission line method

The sample is placed in a guided transmission line such as a coaxial airline or waveguide straight section or suspended in free space between two antennae. Several algorithms to calculate permittivity and permeability from S-parameter measurements are available to choose from. Coaxial airlines or rectangular waveguide transmission lines are used as sample holders. The transmission line method works best for materials that can be precisely machined to fit inside the sample holder. The Keysight software N1500A includes an algorithm that corrects for the effects of air gap between the sample and holder, reducing the largest source of error with the transmission line technique. With special fixtures and measurement equipment this method could cover frequencies from 200MHz to 1.1 THz.

Free space method

In this method, materials are placed between two antennas for a non-contacting measurement. The free space method works best for large flat solid materials, but granular and powdered materials can also be measured in a fixture. It is very useful for many

applications such as non-destructive testing, measuring materials that must be heated to very high temperatures, or measuring a large area of material that is non-uniform such as honeycomb or a composite. Depending on measurement system, this method could cover frequency range from few GHz till 1.5 THz. As a reference samples for calibration accuracy verification, PTFE samples could be used. Typical measurement results of 1.5mm thick PTFE sample in a frequency range from 0,75 to 1,1 THz are presented in Fig.2. Special quasi-optical beam focusing systems could be used to improve measurement accuracy and repeatability.
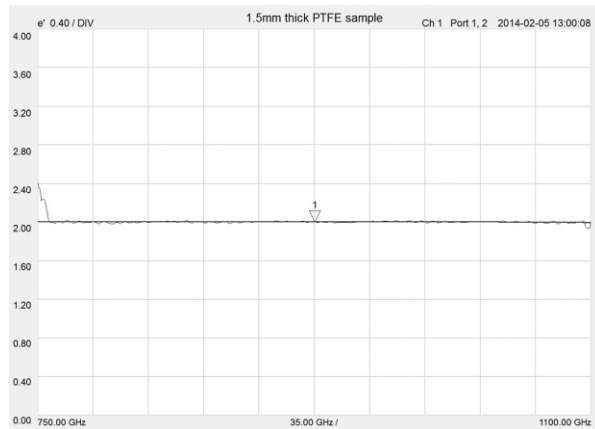
Fig.2. Real part of permittivity for 1.5mm PTFE sample

Resonant cavity method

Resonant cavity method is the best suitable for thin films, substrate materials, and other low loss dielectric materials. The resonant cavity method uses a network analyzer to measure resonant frequency and Q of a resonant cavity fixture, first empty and then loaded with the sample under test. Permittivity can then be calculated from these measurements, knowing the volume of the sample, and some other parameters about the resonant cavity. Because it is a resonant method, only one frequency point is reported. However, it is much more sensitive and has better resolution than the other techniques. Typical resolution for this method is 10^{-4} where the broadband method is 10^{-2}.

Coaxial probe method

The coaxial probe method is best for liquids and semi-solid (powder) materials. A typical measurement system consists of a vector network analyzer or impedance analyzer, a coaxial probe and software. Depending on the analyzer and probe used, we can measure from 10 MHz to 50 GHz. Measurements are conveniently made by immersing the probe into liquids or semi-solids – no special fixtures or containers are

required. Measurements are non-destructive and can be made in real time. These important features allow the dielectric probe kit to be used in process analytic technologies.

Parallel plate capacitor method

The parallel plate method, also called the three-terminal method in ASTM standard D150 [5], involves sandwiching a thin sheet of material or liquid between two electrodes to form a capacitor. The measured capacitance is then used to calculate permittivity. The method works best for accurate, low frequency measurements of thin sheets or liquids. A typical measurement system using the parallel plate method consists of an LCR meter or impedance analyzer. Keysight offers several test fixtures such as 16451B, 16452A and 16543A depending on material types and applied frequency ranges that can cover up to 1 GHz.

Conclusion

Many factors such as accuracy, convenience, and the material shape and form are important in selecting the most appropriate material measurement technique. Keysight offers a wide variety of solutions to measure the dielectric properties for most types of materials in a broad frequency range up to 1.5 THz.

References:

1. Keysight Technologies "Basics of Measuring the Dielectric Properties of Materials", 5989-2589EN (2017)

2. Keysight Technologies "N1500A Materials Measurement Suite", 5992-0263EN (2018)

3. Keysight Technologies "Measuring Dielectric Properties Using Keysight's Materials Measurement Solutions", 5991-2171EN (2018)

4. Keysight Technologies "Solutions for Measuring Permittivity and Permeability with LCR Meters and Impedance Analyzers", 5980-2862EN (2014)

5. ASTM, Test methods for A-C loss characteristics and permittivity (dielectric constant) of solid electrical insulating materials, ASTM Standard D 150, American Society for Testing and Materials

The first observation of the free induction signals of OH radicals in the terahertz region.
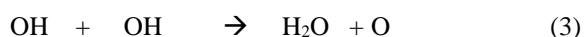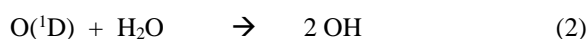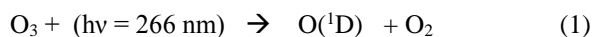
E.N.Chesnokov[1], L.N.Krasnoperov[2], V.V.Kubarev[3], P.V.Koshlyakov[1].

[1]Institute of Chemical Kinetics and Combustion, Novosibirsk, Russia, chesnok@kinetics.nsc.ru
[2]New-Jersey Institute of Technology., Newark,USA
[3] Institute of Nuclear Physics, Novosibirsk,Russia

Hydroxyl radical OH is the main oxidizing agent in combustion processes and in atmospheric chemistry. The rotational spectrum of OH is comparatively simple - there are less than 10 absorption lines in the therahertz region, corresponding to transitions between the lower rotational states of the radical. The FID signal was observed at the OH absorption line at 83.8 cm^{-1}, that corresponds to the transition from the lowest rotational state of OH. Hydroxyl radicals were generated in the following sequence of chemical reactions:

$$O_3 + (h\nu = 266\,nm) \rightarrow O(^1D) + O_2 \qquad (1)$$

$$O(^1D) + H_2O \rightarrow 2\,OH \qquad (2)$$

$$OH + OH \rightarrow H_2O + O \qquad (3)$$

The concentration of OH radicals was ~ 10^{15} cm-3, lifetime ~ 300 …. 700 mks.

The pulse of UV laser (266 nm) was synchronized with the FEL pulses. Shape of the FEL pulse with FID signal after the optical cell was recorded by an ultrafast Schottky diode detector and 30GHz oscilloscope.

Fig.1 shows the first experimentally observed FID signal of a hydroxyl radical, accumulated at 500 mks after the UV pulse The moment t = 0 corresponds to the input FEL pulse. The signal from the laser pulse was accumulated separately, in the absence of radicals., and was subtracted .
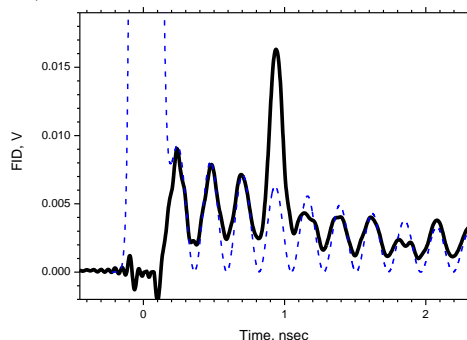

Fig. 1. Experimentally observed FID signal of OH radical. Exciting laser pulse was acc accumulated separately and subtracted. Dashed line – numeric modeling of the FID.

Absorption line of the OH radical is a Λ- doublet with a splitting of 4.3 GHz. The width of the FEL spectrum exceeds this splitting, therefore the laser simultaneously excites both components of the doublet. The FID signal contains characteristic beats with a period of 0.23 ns.

By changing delay between UV pulse and moment of measurements we can see the growing of OH concentration and at big delays decay of the OH concentration.

During the lifetime of the OH radical, many pulses of FEL pass through the cell, each of which initiates a FID signal. We could register a sequence of 10 pulses simultaneously, obtaining separate frames of the birth and death of the radical

The influence of the magnetic field on the FID signal was studied by numerical simulation. A longitudinal magnetic field leads to a rotation of the polarization plane of the signal. The angle of rotation depends on the time after the FEL pulse. The effect of a nonmonotonic rotation of the polarization was predicted - after a certain time after the pulse, the direction of rotation changes
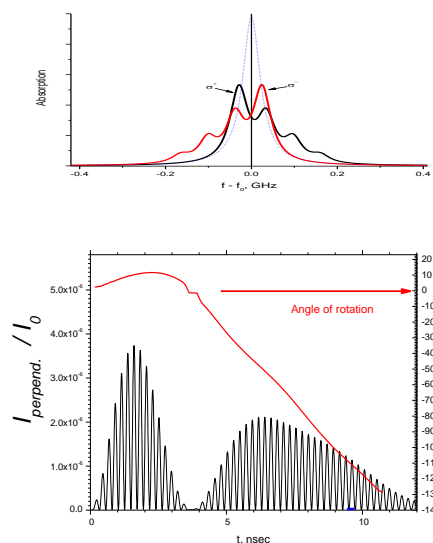
Fig. 2. Influence of magneticfield 100 G on OH spectrum (upper plot) and on FID signal. Red line shows the rotation angle of polarization plane of the FID vs.time.

References

1. *Chesnokov E. N., Kubarev V. V., Koshlyakov P. V., Kulipanov G. N.* Direct observation of the terahertz optical free induction decay of molecular rotation absorption lines in the sub-nanosecond time scale// Appl. Phys. Lett.2012, V. 101, 131109.

2. *Chesnokov E. N., Kubarev V. V., Koshlyakov P. V.,.* Rotation commensurate echo of asymmetric molecules-Molecular fingerprints in the time domain// Appl. Phys. Lett.2014, V. 105, 261107.

Closing the terahertz gap: a composite approach toward measuring continuous dielectric functions from microwave to visible wavelengths

Robert D. Dawson[1], Alexander V. Boris[1]

[1]Max Planck Institute for Solid State Research, Stuttgart, Germany, r.dawson@fkf.mpg.de

Many correlated electron materials are known to harbor low-lying states at terahertz (THz) frequencies which often couple to higher-energy spectral features. However, technical limitations have made it difficult to obtain optical responses across large bandwidths without gaps in the THz range. We present a technique which combines microwave interferometry, time-domain THz spectroscopy, and ellipsometry to obtain the full complex optical response function without gaps from microwave to visible wavelengths.

The study of quantum and correlated electron materials remains one of the largest research thrusts in physics and materials science today. This attention is due to the intriguing unconventional nature of this class of materials, which results from novel electron and quasiparticle entanglement and topological properties. These unconventional properties give rise to a menagerie of exotic and competing phases, such as those which make up the complex phase diagram of the high-temperature copper-oxide superconductors, and in general remain to be fully understood [1].

A key aspect of correlated electron materials is that they possess states lying at low energies which couple to higher energy spectral features as a consequence of their strong electron interactions. This aspect manifests in the optical response functions of the materials as pronounced shifts of the optical conductivity spectral weight across large frequency ranges as a function of temperature, chemical doping, and applied magnetic field. In the case of the copper-oxide high temperature superconductors, for example, optical conductivity spectral weight up to mid-infrared energies participates in the superconductivity-induced changes of the material response, while low-energy signatures of the ground state remain at microwave frequencies and below. This implies that in order to properly capture the nature of the low-energy phase transitions in the cuprates, and quantum materials in general, the low-energy optical response must be related to the optical response at energy scales which do not correspond to the characteristic gap energy, but rather to the maximum energies of the fundamental interactions which drive the phase transitions.

However, the presence of both high- and low-energy spectral features in the optical response of correlated electron materials further complicates the study of their underlying physics because the response of robust phases tends to strongly mask the more delicate spectral fingerprints of the competing orders. Optical techniques which rely on Kramers-Kronig transformations to extract the full material response, such as infrared reflectivity, may thus not resolve these fine spectral features, since extrapolations of the data above and below the measured frequency range may introduce artifacts into the calculated response functions. A full and accurate understanding of the optical response of correlated electron materials therefore requires a technique which is not only very broad in its spectral range, but also directly sensitive to both the dissipative and inductive parts (the real and imaginary parts, respectively) of the material dielectric function.

Here, we present a composite optical spectroscopy technique to extract the continuous dielectric functions of thin film materials between 0.6 meV and 6.5 eV. The technique is based on the independent measurement of the complex dielectric function in the microwave regime via quasi-optical interferometry and in the far-infrared through visible spectrums by means of spectroscopic ellipsometry, but takes the crucial step of connecting the microwave regime to the far-infrared regime through the application of high-resolution time-domain THz spectroscopy. Until recently, technological limitations have hindered the development of high-power emitters and detectors operating in the THz regime, but recent advances in large-area electro-optic antennas [2] and asynchronous optical sampling techniques [3, 4] have allowed THz spectroscopy to be applied to high-resolution studies of the low-energy electrodynamics of solids. The main advantage of time-domain THz spectroscopy is that it probes both the amplitude and phase response of materials by directly obtaining the temporal profile of the THz electric field as it passes through a sample. Therefore, by combining quasi-optical microwave interferometry and ellipsometry with time-domain THz spectroscopy, it is possible to extract both the real and imaginary parts of material dielectric response functions at all frequencies between 0.6 meV and 6 eV without the need for Kramers-Kronig relations.

We perform initial measurements of the complex dielectric function in the microwave range from 0.6–1.6 meV (5–13 cm^{-1}) using a microwave interferometer in the Mach-Zehnder geometry with a backward wave oscillator as the radiation source. The change in transmission and the phase shift induced by the sample are measured separately as a function of frequency and then inverted together to obtain the complex optical response $\sigma_1(\omega)$ and $\varepsilon_1(\omega)$ in the measured frequency range.

Next, the complex optical response is obtained from near-IR to visible frequencies by means of spectroscopic ellipsometry. Far-IR measurements in the range 10–90 meV (80–700 cm^{-1}) are measured with a homebuilt ellipsometer using a Bruker IFS 66v/S Fourier transform IR spectrometer and a synchrotron radiation source at the IR-1 beamline of the Karlsruhe Research Accelerator at the Karlsruhe Institute of

Technology. Measurements in the mid- and near-IR (90 meV–1.2 eV, 700–10000 cm^{-1}) are performed at the MPI for Solid State Research in Stuttgart with a homebuilt ellipsometer based on a Vertex 80v Fourier transform IR spectrometer, while measurements in the visible range (0.6–6.5 eV) are performed with a commercially-available Woollam variable angle spectroscopic ellipsometer. After data collection in all spectral ranges, the measurements of the ellipsometric angles Ψ and Δ from each instrument are collated and appended, and then used to directly calculate the complex optical response $\sigma_1(\omega)$ and $\varepsilon_1(\omega)$ in the frequency range 10 meV to 6.5 eV.

Time-domain THz spectroscopy measurements are performed in the transmission configuration using a LaserQuantum HASSP spectrometer, operating at 1 GHz repetition rate. The data collection scheme is based on the asynchronous optical sampling technique [3, 4] which removes the need for a physical moving time delay stage and extends the width of the measurable temporal window to 1 ns. A LaserQuantum TeraSED large-area, interdigitated-type antenna is used for THz generation, which provides a usable THz bandwidth of 0.2–6.5 THz (0.8–27 meV). THz measurements of epitaxial thin films (20–100 nm) grown on 0.5–1 mm thick substrates are carried out several times in an alternating sample-reference order to reduce the effects of measurement drift over time, with an identical bare substrate used as the reference. The time-domain waveform of each sample and reference are windowed with identical Gaussian-shaped window functions to remove the train of reflected pulses which originate from reflections of the main THz pulse from optical components within the spectrometer. Complex-valued transfer functions are then calculated from each sample-reference pair and averaged. Finally, the complex index of refraction $n + \mathrm{i}k$ is calculated from the averaged transfer function by inversion of the Fresnel transmission coefficient for a thin film on a thick dielectric slab.

The substrate thickness mismatch between the sample substrate and reference substrate must be considered when calculating the complex index of refraction, since thickness variations on the order of a micron or less can correspond to changes in the transmission amplitude and phase similar in magnitude to those induced by the thin films. Initial measurements of the thickness of both the sample and the reference are therefore made with a high-precision Nikon TC-101A micrometer with accuracy better than 10 nm. Furthermore, small diffraction effects due to shape variances in the measurement aperture between sample and reference also can correspond to significant changes in the complex film transmission. To reduce artifacts due to this effect, a single-fixed-aperture measurement scheme was developed which featured a single copper aperture of diameter 3–9 mm rigidly fixed to a large copper sample cage. The sample and reference were then mounted onto a small frame with a thin Mylar sheet, and could be moved freely into and out of the beam path.

The values of $\sigma_1(\omega)$ and $\varepsilon_1(\omega)$ calculated from time-domain THz spectroscopy were merged with those from microwave interferometry and IR ellipsometry by introducing a complex-valued substrate thickness mismatch constant into the phase of the Fresnel transmission coefficient, and allowing it to vary slightly as a fitting parameter. Correct values of the substrate thickness mismatch were taken as the values which produced smooth agreement between THz data and microwave or IR data where the measurements overlapped.

Finally, the validity of the measurement method is checked by carrying out a Kramers-Kronig consistency analysis of the measured complex optical response. The measured $\sigma_1(\omega)$ data is extrapolated from the lowest measured frequency to $\omega = 0$ with a material-dependent model assumption, and then its Kramers-Kronig transformation is calculated. A high degree of agreement between the calculated transformation and the measured $\varepsilon_1(\omega)$ indicates success of the composite measurement method. The Kramers-Kronig consistency analysis also allows the sensitivity of this measurement technique to be extended to frequencies below the lowest measured energy, because the extrapolation procedure definitively assigns optical conductivity spectral weight to the low energy domain.

In conclusion, we have presented here a composite wide-band technique to directly obtain both the real and imaginary parts of the continuous complex dielectric function of materials from 0.6 meV to 6.5 eV. This technique is based on the combination of independent quasi-optical, time-domain THz, and spectroscopic ellipsometry measurements. While not required to extract the full material optical response, a Kramers-Kronig consistency check is performed to assess the validity of the method. Due to the extremely wide-band nature of the technique and its non-reliance on Kramers-Kronig analysis, the technique is well-suited to the study of optical properties of quantum and correlated electron materials, and indeed is already showing some promising results on epitaxial thin films of copper oxide high-temperature superconductors.

References

1. *Keimer, B., Moore, J. E.* The physics of quantum materials // Nature Physics 2017. V. 13, P. 1045–1055.

2. *Beck, M., Schäfer, H., Klatt, G., Demsar, J., Winnerl, S., Helm, M., Dekorsky, T.* Impulsive terahertz radiation with high electric fields from an amplifier-driven large-area photoconductive antenna // Optics Express 2010. V. 18, No. 9, P. 9251–9254.

3. *Bartels, A., Cerna, R., Kistner, C., Thoma, A., Hudert, F., Janke, C., Dekorsy, T.* Ultrafast time-domain spectroscopy based on high-speed asynchronous optical sampling // Rev. Sci Instrum. 2017. V. 78, P. 035107.

4. *Klatt, G., Gebs, R., Janke, C., Dekorsy, T., Bartels, A.* Rapid-scanning terahertz precision spectrometer with more than 6 THz spectral coverage // Optics Express 2009. V. 17, No. 25, P. 22847–22854.

Absorbance of oxipane material in THz frequency range

D. A. Gomon, P. S. Demchenko, M. K. Khodzitsky

ITMO University, Saint-Petrsburg, Russia, GomonDA89@ya.ru

Introduction.

The THz range is typically defined as 0.1–10 THz. A lot of molecules (biological molecules for example) have strong electromagnetic response in this frequency range. That why THz radiation is widely used in such areas as telecommunications, radar and imaging systems, material spectroscopy, medical diagnosis and therapy.[1-7]

Creating a compact reliable source of terahertz (THz) radiation is one of the most formidable tasks of contemporary applied physics.[8,9] One of the latest trends in THz technology[10] is to use carbon nanotubes, cylindrical molecules with nanometer diameter and micrometer length,[10-14] as building blocks of high-frequency devices.

This work devoted to study "oxipane" optical properties (such absobance, permittivity, refractive index) in THz frequency range. Material "oxipane" may be effective absorber for using in biological destructive THz frequencies screening.

Experimental setup.

A 3D-image of the THz TDS setup is shown in Figure 1 [15, 16]. The femtosecond IR laser parameters are the following: a central wavelength of 1040 nm; a full width at half maximum (FWHM) of 5 nm; an average output power of 1.1 W; and a pulse width of 120 fs. The femtosecond infrared laser beam is split in two beams: probe and pump with a ratio of 10% to 90%, respectively. The optical delay line controls optical path of the pump beam. The beam is modulated by a chopper (Ch) at 667 Hz. The generator of the THz radiation (InAs crystal) takes place in a magnetic system with a field of 2 T. After passing through an IR radiation filter, the THz beam incidents on the sample.
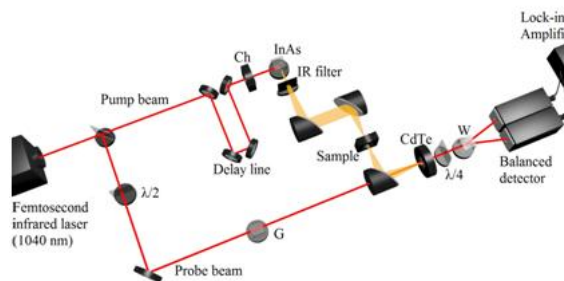
Fig. 1. Schematic of the THz TDS setup with optical illumination. Ch – optical chopper, InAs – THz radiation generator (InAs crystal in a magnetic field of 2 T), G – Glan prism, CdTe – nonlinear crystal, $\lambda/2$ and $\lambda/4$ – half-wave and quarter-wave plates, W – Wollaston prism.

The THz radiation induces birefringence in the electro-optical crystal (CdTe) for the infrared probe beam. Probe IR beam is split by Wollaston prism (W) into two beams with orthogonal polarization, which are detected by balanced photodiodes (balanced detector). The Fourier transform of the temporal waveform $E(t)$ gives the spectral distribution of the THz pulse in the frequency domain. The THz field in the frequency domain is a complex value, containing the amplitude and the phase information which may be used to calculate all complex optical properties of a sample.

Description of oxipane properties.

Oxipane is an innovation high-temperature non-woven material from chopped polyacrylonitrile fiber. Oxipane could be used as a protective layer for different applications:

1. *Heat protection:* Can be used as an efficient heat protection in the temperature regime below 300-450 °C, as an incombustible lining for sewing working clothes, as a fire barrier membrane in the production of soft furniture and seats in public transport, and for filtration of hot gases.

Oxipane or non-woven materials with oxipane additives are used as protective membranes in seats of airplanes, trains, and other public transport. The use of oxipane retards fire propagation and, as a consequence, ejection of toxic substances.

2. *Manufacturing of gas filters:* Oxipane filters vapors and aerosols of acids, alkalis, and solvents, including those heated to 450 °C.

The use of filters based on oxipane makes it possible to improve ecological environment on territories adjacent to metallurgical complexes, enterprises producing cement, pulp-and-paper mills, chemical complexes, and a series of other enterprises related to production of harmful products.

That why oxipane is perspective candidate for s*ewing of working clothes:* An oxipane lining possess a low heat conductance and, as a consequence, possesses a decrease in the thermal effect on the human organism.

Material oxipane may present effective absorptance in THz frequency range. That means that oxipane could be used for THz frequencies screening.

Formulas and results.

Oxipane characteristics such as real part of refractive index, the absorption coefficient, real and imaginary part of permittivity were calculated by formulas [17].

Real part of refractive index:

$$n_{real}(f) = 1 + \frac{c(\varphi_{sam}(f) - \varphi_{ref}(f))}{2\pi l f},$$

where c is the speed of light in vacuum, *l* is the thickness of medium, f is the frequency, φ(ω) is phase data.
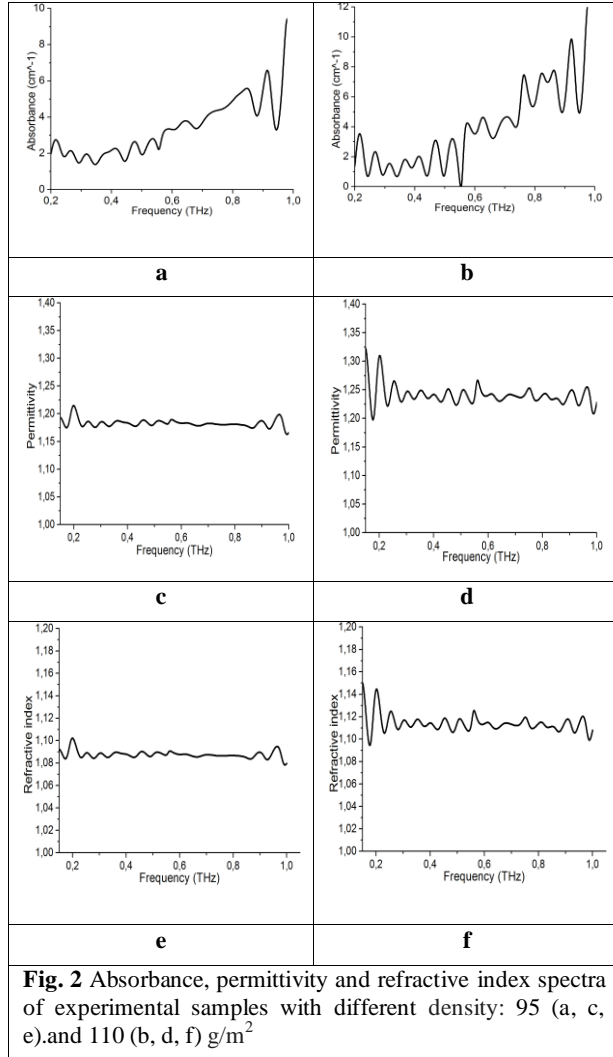
The absorption coefficient:

$$\alpha(f) = \frac{1}{l} ln(\frac{E_{0\,ref(f)}}{E_{0\,sam(f)}})^2,$$

$E_{ref}(\omega)$ and $E_{sam}(\omega)$ reference and sample waveforms were converted by Fourier transformation.

Real and imaginary part of permittivity:

$$\varepsilon_{real}(f) = n_{real}^2(f) - n_{imag}^2(f)$$
$$\varepsilon_{imag}(f) = 2n_{real}(f)n_{imag}(f)$$

a **b**

c **d**

e **f**

Fig. 2 Absorbance, permittivity and refractive index spectra of experimental samples with different density: 95 (a, c, e).and 110 (b, d, f) g/m^2

In this paper we investigate the oxipane optical properties (such absorbance, permittivity, refractive index) in THz frequency range using THz time domain spectroscopy [18]. We studied two oxipane samples with different density: (95 and 110 g/m^2). Their absorbance, permittivity and refractive index spectra are shown in Fig. 2.

Conclusions.

Oxipane optical parameters spetra were investigated in 0,15-1 THz range. Absorption coefficient shows increasing character with values from 1,5 to 10 cm^{-1} and from 0 to 12 cm^{-1} for examples with density of 95 g/m^2 and 110 g/m^2 respectively. Permittivity shows small fluctuations with average value 1,17 and 1,24 for examples with density of 95 g/m^2 and 110

g/m^2 respectively. Refractive index also shows small fluctuations with average value of 1,09 and 1,11 for examples with density of 95 g/m^2 and 110 g/m^2 respectively.

That means that oxipane is an perspective candidate for tunable THz components.

Reference.

[1] T. Kleine-Ostmann and T. Nagatsuma, "A review on terahertz communications research," *Journal of Infrared, Millimeter, and Terahertz Waves*, vol. 32, no. 2, pp. 143–171, jan 2011.

[2] W. Menzel, "Millimeter-wave radar for civil applications," in *Radar Conference (EuRAD), 2010 European*. IEEE, pp. 89–92, oct 2010.

[3] J. El Haddad, B. Bousquet, L. Canioni, and P. Mounaix, "Review in terahertz spectral analysis," *TrAC, Trends Anal. Chem.*, vol. 44, pp. 98–105, mar 2013.

[4] P. H. Siegel, "Terahertz technology in biology and medicine," *IEEE Transactions on Microwave Theory and Techniques*, vol. 52, no. 10, pp. 2438–2447, oct 2004.

[5] M. Borovkova, M. Serebriakova, V. Fedorov, E. Sedykh, V. Vaks, A.Lichutin, A. Salnikova, and M. Khodzitsky, "Investigation of terahertz radiation influence on rat glial cells," *Biomedical optics express,*vol. *8*, no.1, pp. 273-280, jan 2017.

[6] Lee, M.; Wanke, M. C. Science 2007, 316, 64.

[7] Borovkova, Mariia, et al. "Complementary analysis of Mueller-matrix images of optically anisotropic highly scattering biological tissues." *Journal of the European Optical Society-Rapid Publications* 14.1 (2018): 20.

[8] Ferguson, B.; Zhang, X. C. Nat. Mater. 2002, 1, 26.

[9] Dragoman, D.; Dragoman, M. Prog. Quantum Electron. 2004, 28, 1.

[10] Saito, R.; Dresselhaus, G.; Dresselhaus, M. S. Physical Properties of Carbon Nanotubes; Imperial College Press: London, 1998.

[11] Carbon Nanotubes: Synthesis, Structure, Properties, and Applications; Dresselhaus, M. S., Dresselhaus, G., Avouris, Ph., Eds.; Springer-Verlag: Berlin, 2001.

[12] Reich, S.; Thomsen, C.; Maultzsch, J. Carbon Nanotubes: Basic Concepts and Physical Properties; Wiley: Berlin, 2004.

[13] Smirnov, Serguei, et al. "Optically Controlled Dielectric Properties of Single-Walled Carbon Nanotubes for Terahertz Wave Applications." *Nanoscale* (2018).

[14] Anantram, M. P.; Le´onard, F. Rep. Prog. Phys. 2006, 69, 507.

[15] V.Y. Soboleva, D.A. Gomon, E.A. Sedykh, V.K. Balya, and M.K. Khodzitskii, "Development of narrow bandpass filters based on cross cavities for the terahertz frequency range," *Journal of Optical Technology*, vol. 84, no. 8, pp. 521-524, 2017.

[16] D.A. Gomon, E.A. Sedykh, M.K. Khodzitsky, K.I. Zaitsev, I.T. Monroy, S. Rodriguez, A.V. Vozianova, "Influence of the Geometric Parameters of the Electrical Ring Resonator Metasurface on the Performance of Metamaterial Absorbers for Terahertz Applications," *Chinese Optics*, vol. 11, no. 1, pp. 47-59, 2018.

[17] C. How Gan, "Analysis of surface plasmon excitation at terahertz frequencies with highly doped graphene sheets via attenuated total reflection," *Applied Physics Letters*, vol. 101, no. 11, pp. 111609-4, sep 2012.

[18] Zaitsev, K. I., et al. "Terahertz spectroscopy of pigmentary skin nevi in vivo." *Optics and Spectroscopy* 119.3 (2015): 404-410.

Terahertz spectroscopy of graphene-based materials on different substrates under external infrared optical pumping

Alexander Grebenchukov[1], Anton Zaitsev[1], Petr Demchenko[1], Mikhail Novoselov[1], Evgeniya Kovalska[2], Anna Baldycheva[2], Mikhail K. Khodzitsky[1]

[1]ITMO University, St. Petersburg, Russian Federation, grebenchukov_a@mail.ru
[2]University of Exeter, Exeter, United Kingdom

In recent years, two-dimensional (2D) materials have attracted heightened interest of researchers including the field of terahertz (THz) science [1]. Despite significant progress in this direction, especially, in the study of the first 2D material – graphene, there is still a need to search for new materials with superior characteristics. Such new 2D materials can be potentially useful for advanced THz photonics devices due to their unique properties. From this point of view, detailed study of their THz properties such as photoconductivity and optical properties is a prerequisite for their successful use [2].

In this work, we study infrared optical pump induced changes in terahertz conductivity of 5-layered (FLG) and 80-layered (MLG) pristine and chemically modified (by $FeCl_3$ intercalation) graphene on dielectric and semiconductor substrates using terahertz time-domain spectroscopy.

The scheme of system used is depicted on the Fig. 1. The 980 nm continuous-wave (CW) laser was used as a pumping source.
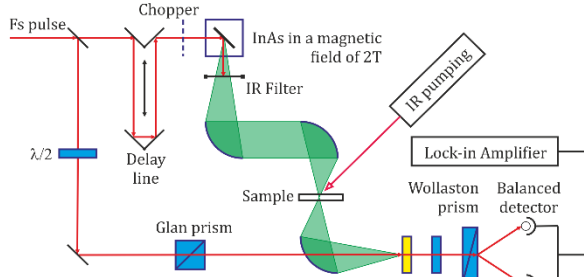
**Fig. 1.** Scheme of the experimental THz-TDS setup.

To obtain complex sheet conductivity dispersions, an effective medium model and a thin-film approximation [3] were used (when the sample thickness is much smaller than the operational wavelength):

$$\frac{\hat{E}_{sam}(\omega)}{\hat{E}_{sub}(\omega)} = \frac{\hat{n}(\omega)+1}{\hat{n}(\omega)+1+Z_0\ \hat{\sigma}(\omega)}, \qquad (1)$$

where $\hat{E}_{sam}(\omega)$ and $\hat{E}_{sub}(\omega)$ are the complex amplitudes of the signals transmitted through the sample on a substrate (full structure) and bare substrate correspondingly, $\hat{n}(\omega)$ is the substrate refractive index, $Z_0 = 377$ Ohm is the free space impedance. The complex amplitudes mentioned above were obtained by the fast Fourier method (FFT) from the THz signal timeforms, which were previously processed to avoid spectral distortions resulting from diffraction on a substrate and reflections in its volume. This method allows to get both an amplitude and phase of a THz

wave transmitted through the air, substrate and a sample.

The extracted complex sheet conductivity dispersions are depicted in the next Figures.
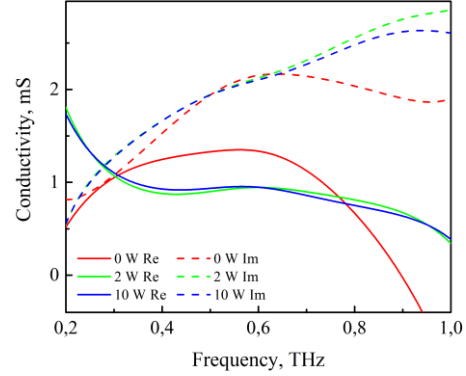
Fig. 2. Complex sheet conductivity dispersions of FLG on quartz substrate for the different pumping power values.
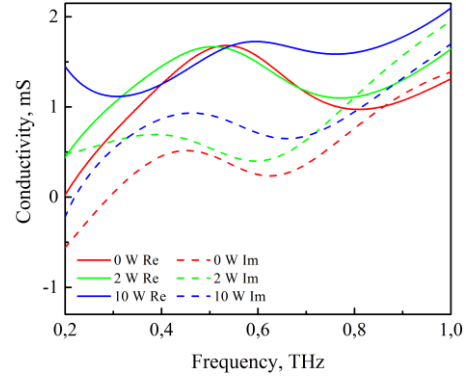
Fig. 3. Complex sheet conductivity dispersions of FLG on PET substrate for the different pumping power values.

It is seen that conductivity behavior strongly depends on a type of dielectric substrate, and the losses in the abovementioned structures are low (for the case of pristine FLG).
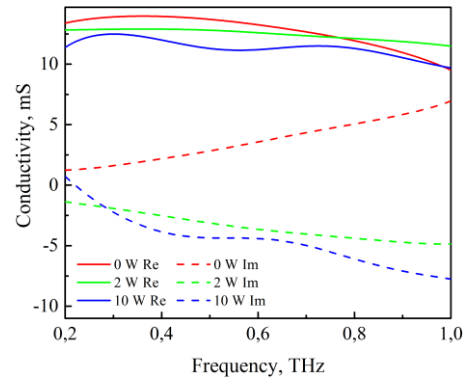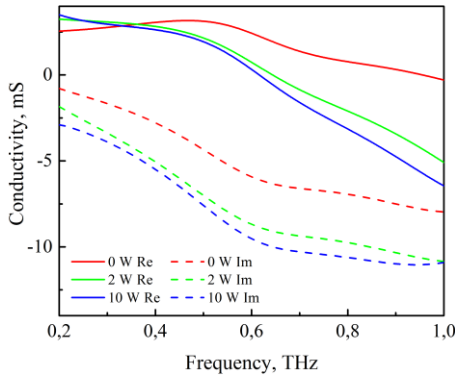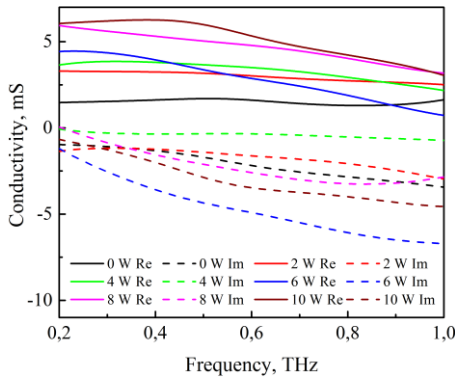
Fig. 4. Complex sheet conductivity dispersions of FeCl₃-FLG on quartz substrate for the different pumping power values.
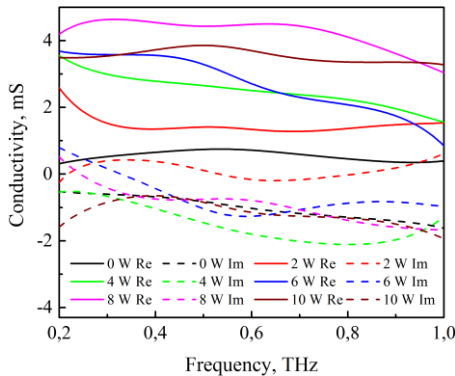

Fig. 5. Complex sheet conductivity dispersions of FeCl₃-FLG on PET substrate for the different pumping power values.

The losses in the FeCl₃-FLG on PET substrate are much smaller than for the case of quartz substrate, and both real and imaginary parts of conductivity can be effectively tuned. The real part of conductivity in FeCl₃-FLG on quartz substrate doesn't change with optical pumping, but the imaginary part can be tuned more effectively than in case of PET substrate.
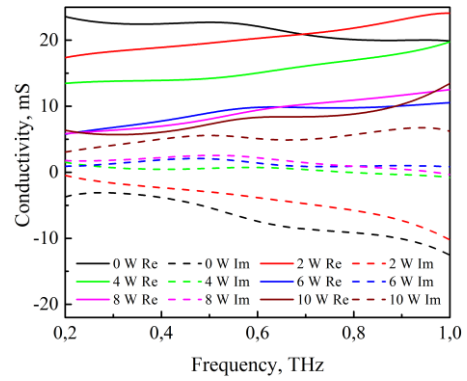

Fig. 6. Complex sheet conductivity dispersions of FLG on Si substrate for the different pumping power values.
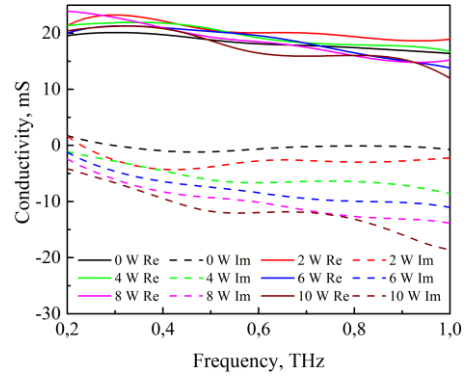

Fig. 7. Complex sheet conductivity dispersions of FeCl₃-FLG on Si substrate for the different pumping power values.

Without pumping, the losses in intercalated MLG sample on a Si substrate are much lower than in pristine one, and the real part of conductivity can be tuned in the wider range. The tunability of imaginary part is slightly higher for the case of pristine MLG.

Fig. 8. Complex sheet conductivity dispersions of MLG on Si substrate for the different pumping power values.

Fig. 9. Complex sheet conductivity dispersions of MLG on TPX substrate for the different pumping power values.

Both the real and imaginary parts of complex conductivity can be effectively tuned in the pristine MLG on Si substrate, and only the imaginary part can be tuned in the case of TPX substrate (the losses in MLG on this substrate are static). For the both cases, the losses are high, but the parameters tunability also has high quality.

Results indicate that the conductivity of investigated materials strongly depends on pumping intensity, number of layers, presence of impurities and the type of underlying substrate. Using this materials, the amplitude and phase of THz radiation can be efficiently adjusted. The findings are helpful for designing of optically tunable terahertz devices based on new two-dimensional materials beyond graphene monolayer.

References

1. *Robin, T., Bouye, C., Cochard, J.* Terahertz applications: trends and challenges // THz, RF, mm, and sub-mm Wave Tech. and Appl. VII. SPIE. 2014. No. 8985. P. 898512.

2. *Wang, Y., Jabbour, C., Zide, J. M. O.* Materials for 1.55 μm-pumped terahertz photoconductive switches: a review // THz Emit., Rec., and Appl. VIII. SPIE. 2017. No. 10383. P. 103830N.

3. *Zhou, Q., et al.* Ultrafast carrier dynamics and terahertz conductivity of photoexcited GaAs under electric field // Applied Physics Letters. 2008. V. 93, No. 10. P. 102103.

Geometry impact on polarizing properties of terahertz chiral metasurface

Maxim Masyukov[1], Anna Vozianova[1], Alexander Grebenchukov[1],

and Mikhail Khodzitsky[1]

[1]Terahertz Biomedicine Laboratory, ITMO University, Saint Petersburg, Russia

Introduction

Metamaterials is a class of composite structured materials with specific properties which cannot be found in nature. Usually these materials consist of unit cells, or meta-atoms, consequently the properties of metamaterial depend on the array of such unit cells. The ability of transformation of the unit cell allows to design and convert metamaterials for the necessary frequency range. Applications of metamaterials in terahertz frequency range attract more and more attention due to an ability to cover a lack of simple and chip elements and systems for terahertz frequencies, such as multispectral imaging systems [1], [2] tunable reflectors[3], switchers[4], filters[5], perfect absorbers [6] polarization converters, mirrors, etc. Such problem is being solved by using chiral metamaterials. In this work we studied the possibility of the transmitted wave polarization changing by metasurfaces with different geometry. The results of the research can be used for THz polarimetry biomedical diagnostics [7-8].

The unit cell under the investigation

The sketch of the unit cell of metasurface under study is shown in Fig. 1. The rosette consists of four planar aluminium half-rings rotated around the normal line placed in the center of the unit cell. The outer radius Rmax is 150 μm, the width of petals is 25 μm. The rosette is patterned on a dielectric (ε=3.5) substrate, which thickness is defined as h=65 μm and the side size is a=600 μm.
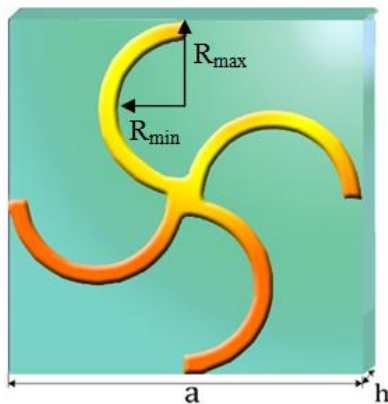
Fig. 1. The unit cell of the metasurface.

The scheme of virtual experiment

The numerical simulations were performed in CST Microwave Studio based on Finite-Elements method [9]. The linearly polarized waves become elliptically polarized ones after the propagation through the metasurface (Fig.2). To characterize the polarization state of the transmitted wave the co- and cross-polarization spectra T_{xx} and T_{xy} were found.
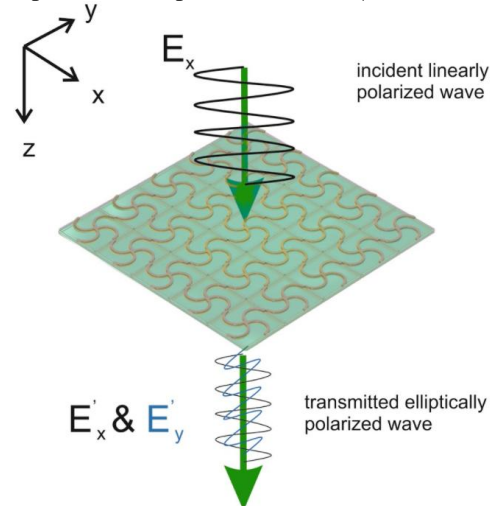
Fig. 2. The scheme of virtual experiment.

The impact of geometry changes on polarization properties of the transmitted waves was investigated in two cases. In the first one, the ellipse aspect ratio (hereinafter referred to as "the ratio") forming the petal of the gammadion was the changed parameter. In the second case the angle α of the rosette rotation was varied. In this paper, four different cases have been studied: α_1 =0 degrees, α_2 =15 degrees, α_3 =30 degrees, α_4 =45 degrees. These manipulations can be seen in Fig. 3.
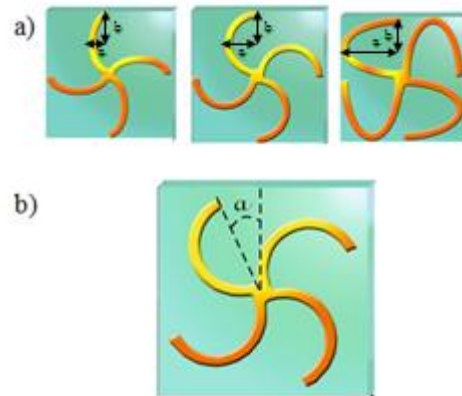
Fig. 3. Chiral unit cell geometry changes: a) from left to right: ellipse aspect ratio b/a_1=2, b/a_2=1, b/a_3=0.5; b) the angle α of the rotation of the rosette.

Results

The ellipticity angle are derived using Jones matrix [10] in terms of transmission of the left- and right-handed circularly polarized waves (T++,T−−) in the frequency 0.1 – 0.8 THz. The ellipticity angle shows a type of polarization: thus, the value of $|\eta|=45$ degrees corresponds to the circular polarization of the electromagnetic waves, and signs "+" or "-" before the value refers to the right-handed or left handed type of polarization state respectively; values between $\eta=\pm45$ degrees are related to elliptical polarization state, except the case when $\eta=0$ for linear polarization.The results can be seen in Fig. 4.

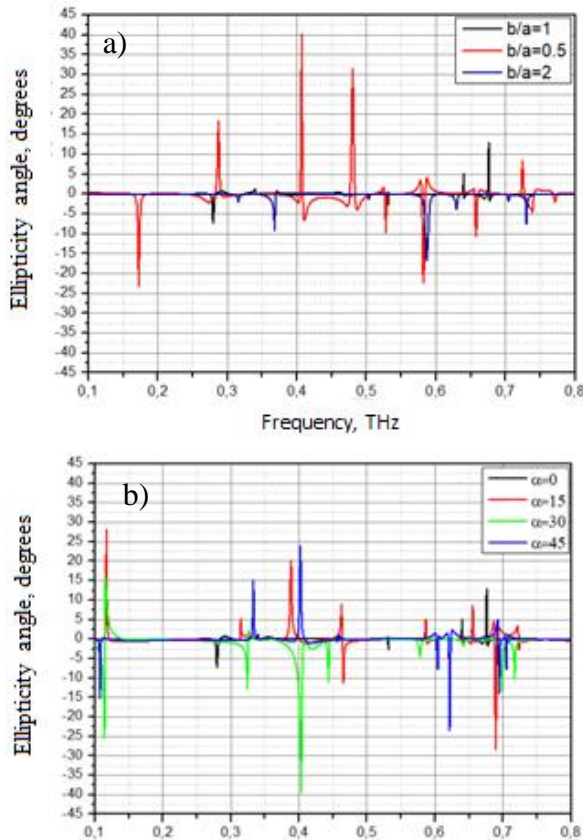**Fig. 4.** The ellipticity angle spectra of the metasurfaces with different geometry: a) metasurfaces with different ellipse aspect ratio b/a; b) metasurfaces with different rotation angle of the rosette.

The varying of the ratio leads to shifting of the values of these frequencies and changing of the metasurface polarization properties. As it shown in the Fig. 4-a, the small ratio leads to bigger polarization conversion. Also it should be noticed that the sign of the ellipticity angle is changed. When b/a=0.5, the ellipticity angle reaches its maximum of 45 degrees at 0.41 THz. So, the polarization is almost right-handed circular one in this case.

The similar situation with rotation of the chiral rosette is observed (Fig. 4-b). There is a noticeable change in the ellipticity angle with changing the angle α. When α=45 degrees, the minimum of the ellipticity is -39 degrees at 0.41 THz, which means that the polarization state is very close to left-handed circular one.

Conclusions

In this work geometry impact on polarizing properties of terahertz chiral at the operating frequencies range of 0.1-0.8 THz was studied. The rotation of the chiral rosette and changing of the ellipse ratio leads to the changing of the ellipticity angle. Therefore it is possible to predict the required polarizing properties of metasurface and make an elliptic polarizer or linear polarization rotator, or make one metasurface which can be used as both of them depending on the geometrical properties of the rosette.

References

1. *Khorasaninejad M*. et al. Multispectral chiral imaging with a metalens // Nano let. 2016. V. 16, No. 7. P. 4595-4600.
2. *Plum E*. Extrinsic chirality: Tunable optically active reflectors and perfect absorbers // App. Phys. Let. 2016.V. 108, No. 24. P. 241905.
3. *Plum E*. et al. Metamaterial with negative index due to chirality //Phys. Rev. B. 2009. V. 79. No 3. P. 035407.
4. *Grebenchukov Alexander, et al.* Optically controlled narrowband terahertz switcher based on graphene // Chin. Opt. 2018. V.11. No.2. P. 2095.
5. *Soboleva V. Y.* et al. Development of narrow bandpass filters based on cross cavities for the terahertz frequency range // Journal of Optical Technology. 2017. V. 84. No. 8. P. 521-524.
6. *Gomon Daniel*, et al. Influence of the geometric parameters of the electrical ring resonator metasurface on the performance of metamaterial absorbers for terahertz applications // Chinese Opt. 2018. V .11, No.1. P. 47-59.
7. *M. Borovkova*, et al. Terahertz time-domain spectroscopy for noninvasive assessment of water content in biological samples // Biomedical Opt. Exp. 2018. V. 9, No.5.P. 2266-2276.
8. *S. I. Gusev*, et al., Influence of glucose concentration on blood optical properties in THz frequency range // Chinese Opt. 2018. V. 11, No. 2. P. 182-189.
9.URL: https://www.cst.com/products/cstmws/solvers/frequencydomainsolver
10. *Menzel C., Rockstuhl C., Lederer F.* Advanced Jones calculus for the classification of periodic metamaterials // Phys. Rev. A. 2010.V. 82., No. 5. P. 0538.

Water and Conductivity in Bioorganic Materials: Complicated Interplay

Konstantin Motovilov[1], Zarina Gagkaeva[1], Artem Grebenko[1], Maxim Savinov[2], Vadim Grinenko[3,4], Aleksei Pronin[5], Vyacheslav Dremov[1], Anton Bubis[1], Piotr Barzilovich[1], Elena Zhukova[1], Zakhar Bedran[1], Lenar Kadyrov[1], Bernard Mostert[6], Boris Gorshunov[1]

[1] Moscow Institute of Physics and Technology, 141701, Institutsky lane 9, Dolgoprudny, Russia, k.a.motovilov@pm.me
[2]Institute of Physics AS CR, Praha 8, Czech Republik
[3]Institute for Solid State and Materials Physics, TU Dresden, 01069, Dresden, Germany
[4]Institute for Metallic Materials, IFW Dresden, 01069, Dresden, Gemany
[5]A.M.Prokhorov General Physics Institute, RAS, 119991, Vavilov street 38, Moscow, Russia
[6]Department of Chemistry, Swansea University, Singleton Park, SA2 8PP, Wales, United Kingdom

It was realized gradually that for the creation of new bioelectronic devices we need to understand the principal limitations of the transport characteristics of existing biological materials, including proteins and pigments. Deep understanding of this problem pushed different scientific groups to apply the best practices of solid state physics to biologically derived materials and to expand the ranges of temperatures and humidities in their studies far beyond common physiological ranges.

For many decades proteins and pigments were studied by methods of solid state physics without thorough control of sample humidity and often in very narrow temperature intervals. For these reasons application of theoretical models developed to describe the mechanisms of charge transport and relaxation processes in these materials was limited. However, the recent studies of conductivity in bacterial filaments [1] and films [2], proteins [3], artificial peptides [4] and synthetic eumelanin [5] revealed crucial importance of the thorough control of humidity.

It was found that the effect of water on bioorganic material is not limited solely to the creation of a network of hydrogen bonds, which allows accelerated transfer of protons by the Grotthuss mechanism. Water has a direct effect on the efficiency of electron/hole transfer, causes oxidation-reduction reactions, doping materials with charge carriers. In addition, an increase of water concentration can do both increase and decrease the level of order in the bioorganic system.

In recent years a rich phenomenology of universal dielectric phenomena in bioorganic systems, previously known only for inorganic phases, has been discovered and studied. It became clear that water directly affects the frequency of the boson peak [6], the transitions between NCL regime, hopping regime and Drude-like regime of conductivity in bio-organic phases [3]. Application of wide-range spectroscopy (from 1 Hz to 10^{14} Hz) made it possible to connect the water binding features detected in the terahertz range with the transport regimes observed in the radio frequency range.

This report will present the results of the transport studies we have obtained on such objects as extracellular bacterial filaments, cytochrome c, bovine serum albumin, extracellular matrix of the bacteria *Shewanella oneidensis* MR-1 and melanin. The investigations were carried out over a wide range of temperatures (5-300 K) and were supplemented by measurements of the specific heat and a number of other parameters.

In the report, an attempt will be made to comprehend in a single manner the diverse and at the same time the general phenomenology that is observed in this list of materials.

References

1. *Grebenko et al.* Impedance spectroscopy of single bacterial nanofilament reveals water-mediated charger transfer // PLOS ONE. 2018. V. 13, No. 1. e0191289.

2. *Ing et al.* Geobacter sulfurreducens pili support ohmic electronic conduction in aqueous solution // Phys Chem Chem Phys. 2017. V. 19.

3. *Motovilov et al.* Observation of dielectric universalities in albumin, cytochrome c and Shewanella oneidensis MR-1 extracellular matrix // Scientific Reports. 2017. V. 7. 15731.

4. *Amit et al.* Hybrid proton and electron transport in peptide fibrils // Advanced Functional Materials. 2014. V. 24, No. 37. P. 5873-5880.

5. *Mostert et al.* Role of semiconductivity and ion transport in the electrical conduction of melanin // PNAS. 2012. V. 109, No. 23. P. 8943-8947.

6. *Perticaroli et al.* Rigidity, secondary structure, and the universality of the boson peak in proteins // Biophys. J. 2014. V. 106. No. 12. P. 2667-2674.

Terahertz plasmonics: achievements and prospects

A. K. Nikitin[1,2], B. A. Knyazev[2,3], V. V. Gerasimov[2,3]

[1] Scientific and Technological Center of Unique Instrumentation, Russian Academy of Sciences, Moscow, Russia,
alnikitin@mail.ru
[2] Novosibirsk State University, Novosibirsk, Russia
[3] Budker Institute of Nuclear Physics, Siberian Branch of Russian Academy of Sciences, Novosibirsk, Russia

I. Brief theory and definitions

Plasmons are collective oscillations of the free electron gas density. Just as light consists of photons, the plasma oscillation consists of plasmons. Plasmon coupled with photon forms another quasiparticle called a plasmon-polariton. Plasmon-polaritons propagating along a "metal-dielectric" interface are called surface plasmon-polaritons (SPPs). They represent themselves a complex of an evanescent p-polarized electromagnetic wave coupled with a wave of density of free charges on surface of a (semi) conductor.

The field of optics studying surface plasmons is often described as Plasmonics, by analogy with electronics [1]. "SPPs is the best known method for confining and guiding EM radiation into the smallest possible volume" [2].

By solving Maxwell's equations with the appropriate boundary conditions, one can find out that: 1) field of surface plasmons is p-polarized, in order to build polarization of the metal surface; 2) they can exist provided the metal dielectric constant is negative; 3) their dispersion relation (between the tangential component of the SPP wave number k_x and the angular frequency ω of their field) for a "metal-dielectric" interface has the form [2]:

$$k_x = \frac{\omega}{c} \cdot \sqrt{\frac{\varepsilon_M \cdot \varepsilon_D}{\varepsilon_M + \varepsilon_D}} \,, \qquad (1)$$

here c is the speed of light in free space; ε_M and ε_D are the dielectric constants of the metal and the dielectric.

The complex value of ε_M makes k_x a complex quality as well, with a real component k_x' that defines the dispersion of SPPs and an imaginary component k_x'' that is proportional to the Joule losses of the SPPs.

The dispersion curves for SPPs on a metal adjoining vacuum or a dielectric are presented in Fig.1. The dotted lines indicate so called "light lines" depicting the dispersion of plane waves in a relevant medium. As one can see, the real component of the SPP wave number is close to the light lines at low frequencies; SPPs have light-like characteristics in the terahertz (THz) range that is THz SPPs are weakly bounded to the interface and propagate a long distance (meters). The value of k_x' deviates from the respective light line as the frequency increases, which is accompanied by stronger confinement (in the dielectric) of the SPPs to the interface. Note, that as ω approaches the value $\omega_{SPP} = \omega_p / \sqrt{1 + \varepsilon_D}$ (here ω_p is the plasma frequency of the metal) the value of $\varepsilon_M \to 0$ and the deviation of k_x' from k_o (the wave number of a plane wave in vac-

uum) infinitely increases, while the propagation length of the SPPs is drastically reduced [2]. Thus one may state that in the low-frequency limit (THz range) SPPs acquire the photonic character, while in the high-frequency limit ($\omega \to \omega_{SPP}$) they resemble a mechanical wave (plasmonic character).
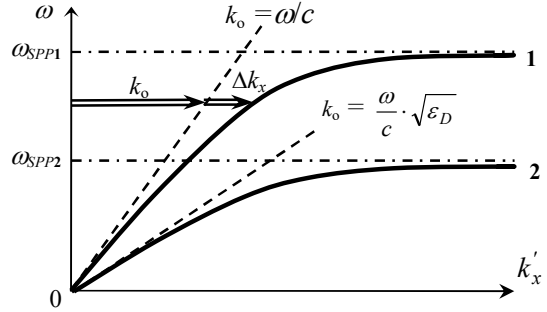
Fig. 1. The dispersion curves of SPPs on interfaces "metal – vacuum" (curve 1) and "metal – dielectric with ε_D" (curve 2).

From the expression for ω_{SPP} it follows that there are at least two ways for controlling confinement (as well as the propagation length) of SPPs to the surface: 1) to change the value of ω_p by, for example, replacing the metal with a semiconductor; 2) to cover the surface with a dielectric layer (curve 2 in Fig.1).

II. Achievements in THz plasmonics

Metals have very large permittivity at THz frequencies, typically 5 to 6 orders of magnitude larger than at optical frequencies. This reduces the penetration depth of the SPP field into the metal and results in a weak confinement of the field to the surface, as well as in an increase of the SPP propagation length L due to the reduction of ohmic loses in the metal.

According to the Drude model for the dielectric permittivity of metals values of $L \sim \lambda^2$ (here λ is the radiation wavelength). But already first experiments with SPPs excited by THz gas lasers revealed great discrepancy between the calculated and measured L values. In the experiments, THz SPPs ran distances an order or even two orders smaller than those predicted by the theory: real THz SPPs ran from a few to tens of centimeters [3]. As it was found out later, the main reason for this was not only the difference between the dielectric permeability of the metal surface and its bulk value, but also the significant radiative losses arising from scattering of SPPs on the surface inhomogeneities [4]. To reduce the losses it was suggested to cover the surface with a thin (~$\lambda/100$) dielectric layer shifting in this way the dispersion curve from the light line and thus making the "SPPs – bulk radiation" process less probable.

Later on it was proposed to employ the newly developed time-domain spectroscopy (TDS) technique for experimental studies of THz SPPs [5, 6]. Using the technique Prof. D. Grischkowsky with colleagues estimated average values of L and SPP field penetration depth δ into air; they also discovered the capability of THz SPPs to jump through cm air gaps between the adjacent metal plates. The TDS is beneficial in many respects when investigating bulk samples, but this method has obvious pitfalls of dispersion origin when SPPs are under study. Using monochromatic radiation produced by lasers, one can avoid problems with dispersion of broadband SPPs, uncertainty in phase shifts at the coupling and decoupling elements, as well as the necessity of the inverse Fourier transform in data processing.

Intensive studies of THz SPPs are conducted with the Novosibirsk free-electron laser (Novo FEL) at the Siberian Synchrotron and Terahertz Radiation Centre [7]. Here they managed to master the end-fire coupling method for effective conversion of FEL radiation into THz SPPs employing cylindrical segments as coupling elements; this made it possible to measure carefully field distribution along the SPP track, to study diffraction of THz SPPs on the rectangular sample edge, to detect bulk waves emitted from the SPP track, to investigate explicitly the process of SPP passing from one to another substrate via air gaps, to establish capability of THz SPPs to be reflected by plane mirrors and to be divided by plane beam splitters [4, 8, 9]. Based on these achievements we have developed and tested the device for measuring the propagation length of THz SPPs in which the input and output elements are fixed; this enables one to perform measurements with a high signal-to-noise ratio.
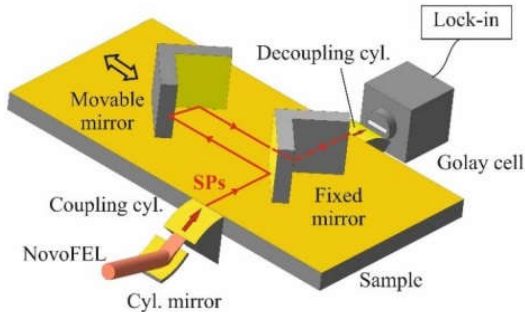
Fig. 2. Device with fixed coupling elements for measuring the propagation length of THz SPPs.

Recently one more way for controlling the value of ω_p, and thus the value of ω_{SPP}, was discovered; this method consists in creating periodic structures (holes, recesses, or objects) of subwavelength dimensions on the metal surface [10]. Such SPPs were called "spoof" or "designed" surface plasmons. The method allows confining THz SPPs not only on metals, but also on graphene, as well as on superconductors [1, 2]. Moreover, it turned out that conductive layers "decorated" with ordered holes have the ability to selectively transmit THz radiation with the transmission efficiency proportional to $(r/\lambda)^4$ (here r is the radius of each hole).

III. Prospects of THz plasmonics

We can distinguish the following promising areas of THz plasmonics development:

1) SPP communication channels based on extended metal-dielectric structures (wires) with rectangular or circular cross-section. The advantages of this method of information transmission are the following: first, the speed of THz SPPs is the maximum possible (it almost equals the speed of light); secondly, it leads to an extremely low group velocity dispersion, allowing essentially undistorted pulse propagation;

2) design of SPP interferometers that will make it possible to create surface plasmon Fourier spectrometers of the THz range;

3) intensive study of "spoof" surface plasmons (especially on graphene) and their interaction with bulk THz radiation;

4) generation of THz SPPs on semiconductor surfaces by radiation with $\omega \approx \omega_p$ condensing the light in the vicinity of the surface and thus paving the way to THz microscopy with super high resolution;

5) study of "localized" SPPs (LSPPs) in semiconductor micron-size particles which, in contrast to metal ones, are pervious for THz radiation. Exciting LSPPs one may concentrate the radiation energy in a very limited space.

References

1. *Maier, S. A.* Plasmonics: Fundamentals and Applications. Springer, 2007. – 224 p.

2. *Gomez, R. J., Berrier A.* Fundamental aspects of surface plasmon polaritons at THz frequencies // In "Handbook of THz technology". Eds by Saeedkia D. Woodhead Publ. Series in Electronic and Optical Materials, 2013. – 688 p.

3. *Koteles, E. S., McNeill,* W. H. Far infrared surface plasmon propagation // Intern. J. Infrared Millim. Waves. 1981. V. 2. P. 361-371.

4. *Gerasimov, V.V., Knyazev, B.A., Lemzyakov, A.G., Nikitin, A.K., Zhizhin, G.N.* Growth of THz surface plasmon propagation length due to thin-layer dielectric coating // JOSA (B). 2016. V. 33. Is. 11. P. 2196-2203.

5. *Jeon, T.-I., Grischkowsky, D.* THz Zenneck surface wave (THz surface plasmon) propagation on a metal sheet // Appl. Phys. Lett. 2006. V. 88. 061113.

6. *Nazarov, M. M., Mukina, L. S., Shuvaev, A.V., Sapozhnikov, D. A., Shkurinov, A. P., Trofimov, V. A.* Excitation of surface EM waves studied by THz spectrochronography // Laser Phys. Lett. 2005. V. 2, No. 10. P. 471–475.

7. *Kulipanov, G. N., Bagryanskaya, E. G., Chesnokov, E. N. et al.* Novosibirsk free electron laser — facility description and recent experiments // IEEE Trans. on THz Science and Technology. 2015. V. 5. No. 5. P. 798-809.

8. *Gerasimov, V.V., Knyazev, B.A., Nikitin, A.K., Zhizhin, G.N.* Experimental investigations into capability of THz surface plasmons to bridge macroscopic air gaps // Optics Express. 2015. V. 23. No. 26. P. 33448-33459.

9. *Gerasimov, V.V., Knyazev, B.A., Nikitin, A.K.* Reflection of THz surface plasmon-polaritons by a flat mirror // Quantum Electronics. 2017. V. 47. No. 1. P. 65–70.

10. *Pendry, J. B., Martín-Moreno, L., García-Vidal, F. J.* Mimicking surface plasmons with structured surfaces // Science. 2004. V. 305. No. 5685. P. 847-848.

Ceramic materials for microwave applications

V. V. Parshin[1], Evgeny Serov[1], P.V. Netcvetaeva[2]

[1]Institute of Applied Physics of RAS, N.Novgorod, Russia, serov@ipfran.ru
[2]OJSC "Magneton Plant", St. Petersburg, Russia

The refractive index (n) and absorption (tanδ) investigations in different kind of ceramic materials produced in Russia and Germany were made by using the open Fabry-Perot resonator with Q factor of approximately 10^6 in the frequency range 50-200 GHz in IAP RAS [1]. The low frequency measurements were made using cavity resonator by producer of materials [2].

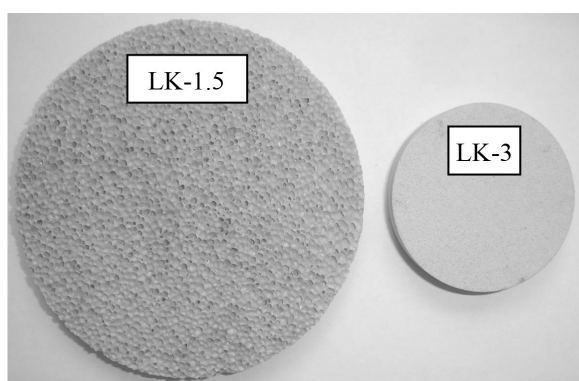Photos of ceramic samples of LK grade produced by JSC "Magneton Plant" (St. Petersburg) are shown in Fig. 1.

Fig. 1. Vacuum tight foam ceramics produced by JSC "Magneton Plant" with extra low refractive index values

Table 1

	n / ε f = 9.4 GHz	tanδ [10⁻⁴] f = 9.4 GHz	ρ [g/cm³]
LK-1.5	1.22 / 1.5	≤ 5	0.48
LK-2	1.41 / 2	≤ 8	0.8
LK-2.5	1.58 / 2.5	≤ 12	1.2
LK-3	1.73 / 3	≤ 15	1.5

Dielectric parameters of vacuum tight foam ceramics obtained at low frequencies are presented in Table 1. The loss tangent frequency dependencies of grades LK-2.5 and LK-3 are presented in Fig. 2. The vacuum tight foam ceramics are very interesting materials for microwave applications because it is possible to slightly change the foam content and by this way to get the needed refractive index value. But measurements are meaningless above 200 GHz due to strong losses increasing mainly due to scattering by "foam". By this reason the grades LK-1.5 and LK-2 are not for using at MM waves.

At the range 100−200 GHz the refractive index increases practically linearly from n=1.58 (9.4 GHz) to n=1.61 (170 GHz) for LK-2.5 and from n=1.73 (9.4 GHz) to n=1.763 (192GHz) for LK-3.

The main parameters of ceramics produced by "Magneton Plant" are presented in Table 2. (at 170 GHz). The loss tangent frequency dependencies of "traditional" ceramics are practically linear at MM waves and refractive indices are practically constant.
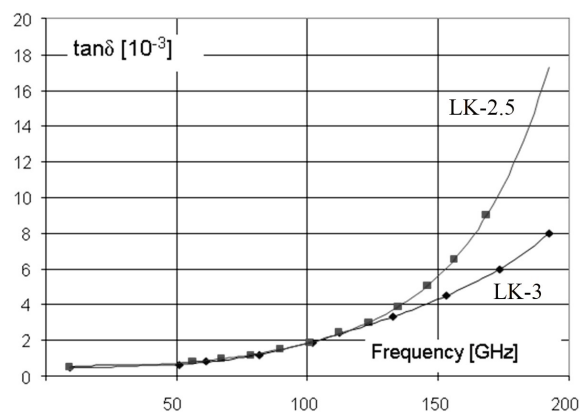

Fig. 2. The loss tangent frequency dependencies of grades LK-2.5 and LK-3

Table 2

Grade	n	tanδ [10⁻⁴]	ρ [g/cm³]
MST-7.3	2.685	8.5	3.18
MST-10	3.185	9	3.37
BK-100M	3.165	4	3.98
TK-20	4.416	50	3.78
TK-40	6.255	37	4.78
LK-2.5	1.61	9	1.2
LK-3	1.76	50	1.5
ST-3	1.707	20	1.15
ST-4	1.995	21	1.35
ST-10	3.194	36	2.00

MST grades are the ceramic materials with very stable refractive index values which are traditionally used as constructive elements in microwave technology. Materials can be made in the different form including very complicated ones.

TK grades are thermally stable microwave ceramics which are widely used to create matching and structural elements, substrates for integrated circuits, filters, dielectric resonators with increased requirements for thermostability of dielectric characteristics.

ST grades are microwave dielectrics based on polymers filled with titanium dioxide. In a large-scale production the materials of this series are the basis for the manufacture of products of complex shape with high accuracy by injection molding methods.

BK corundum ceramics are the alumina-based material with various modifying additives. It is traditionally used for manufacturing of substrates for integrated microwave circuits, substrates for high voltage stabilizers, microstrip device supports, as well as high-voltage insulators and energy output windows for medium-power generators.

The main parameters of ceramics produced by "Friatec" (Germany, http://www.friatec.de) are presented in Table 3. Fig. 3. presents the results of loss tangent measurements. It is the traditional ceramics on the base of different kind of oxides with different

additives for "improving" of electromechanical properties.

Materials (170 GHz)	n	tanδ [10⁻⁴]	k [W/cm·K]	α [10⁻⁶ K⁻¹]	E GPa
Degussit (AlN)	2.91	5.8	1.8-2	3.6	330
Frialit HP79 (Si₃N₄)	2.07	70			
Degussit Al23 HF (Al₂O₃)	3.14	2.7	0.35	7.3	380
Degussit Al23 (Al₂O₃)	3.313	3.6	0.35	8.2	350
Frialit 99.7 HF (Al₂O₃)	3.15	2.7	0.35	7.3	350
Frialit 99.7 (Al₂O₃)	3.15	6	0.35	7.3	350
Frialit FZT (ZrO₂)	3.36	9	0.25	7.5	460
Frialit FZM (ZrO₂+Mg)	5.46	40	0.03	10.4	500

- FRIALIT 99.7 hf (Al2O3)
- DEGUSSIT AL23 HF (white Al2O3).
- The "Aliaxis" measurements.
- DEGUSSIT AL23 or FRIALIT 99.7 (Ivory Al2O3).
- FRIALIT 99.7 or Plate 99.7 (Ivory).
- plate FRIALIT FZT (white), Al2O3 reinforced by ZrO2
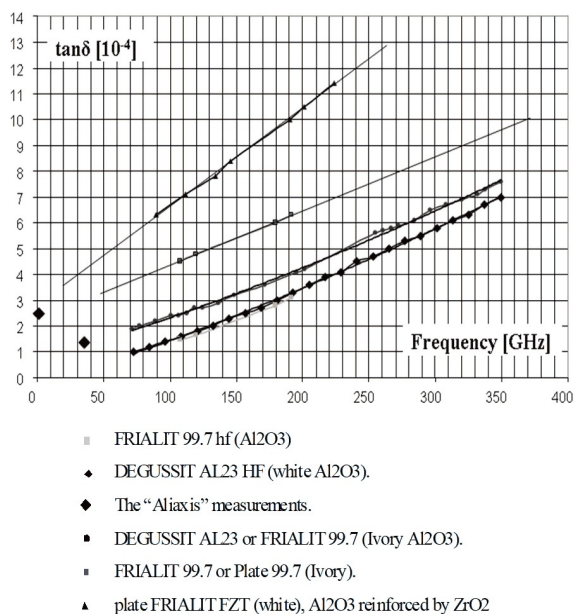
Fig. 3. Loss tangent frequency dependencies of "Friatec" samples

Conclusion

At present, the JSC "Magneton Plant" (St. Petersburg) (http://www.magneton.ru) has mastered the mass production of 35 grades of dielectric materials continuously overlapping the range of dielectric constant (ε) values from 1.5 to 120. Work is in progress to start producing the grades with the values of ε ≈ 140, as well as to increase the thermal resistance of dielectric materials based on polymers to temperatures of 120 ÷ 250°C [1].

As a result of the research, it can be concluded that a number of materials, with low absorption, are quite suitable for use in MM and partially in the SubMM ranges for various structures interacting with electromagnetic wave.

References

1. *Parshin, V. V., Tretyakov, M. Yu., Koshelev, M. A., Serov, E.A.* Modern resonator spectroscopy at submillimeter wavelengths // IEEE Sensors Journal. 2013. V. 13, No 1. P. 18-23.

2. *Firsenkov, A. I., Kanivetc, A. J., Kasatkina, T. C., Ershova, O. M., Ivanova, L. P., Ershova, P. V.* Microwave dielectric materials produced by JSC "Magneton Plant" // Proceeding of IV-th All Russian conference Microwave Electronics and microelectronics. St.-Petersburg: ETU «LETI» publishing house , 2015. – V 2. – P. 55-59.

Modelisation of a gas phase polarization induced by a 200 GHz chirped pulse

R. Bocquet[1], D. Fontanari[1], C. Bray[1], G. Mouret[1], A. Cuisset[1], G. Dhont[1], K. Hickson[2] and F. Hindle[1]

[1]LPCA, Université du Littoral Côte d'Opale, 59140 Dunkerque, France, robin.bocquet@univ-littoral.fr

[2]Institut des Sciences Moléculaires, Université de Bordeaux, Talence, F-33400, France

Introduction

A millimeter wave chirped pulse spectrometer (mmWCP) has been developed to study chemical reactivity at low temperature using the CRESU technique [1]. The project goal is to detect and quantify gas species created during reactivity at thermodynamic conditions close to interstellar media, requiring the combination of the 2 techniques cited above. The first part of the project, undertaken at the LPCA, is the realization and the development of the mmWCP operating between 190 - 210 GHz [2]. One of the interests of this instrument is its capability to simultaneously and rapidly measure numerous molecular transitions of different species in gas phase by probing individual rotational transitions. However, during the trials of the experiment, we were confronted with the difficulty of determining the rotational line intensities according to their position within the chirped pulse. For this reason, we have undertaken a theoretical study to get obtain an analytical expression for the detected signal as a function of the line position in the pulse.

Experimental set up

A mmWCP instrument operates in 2 phases. The first is the polarization of the gas under study by the CP source. The second phase is the recording the Free Induction Decay (FID) signal after extinction of the CP source.
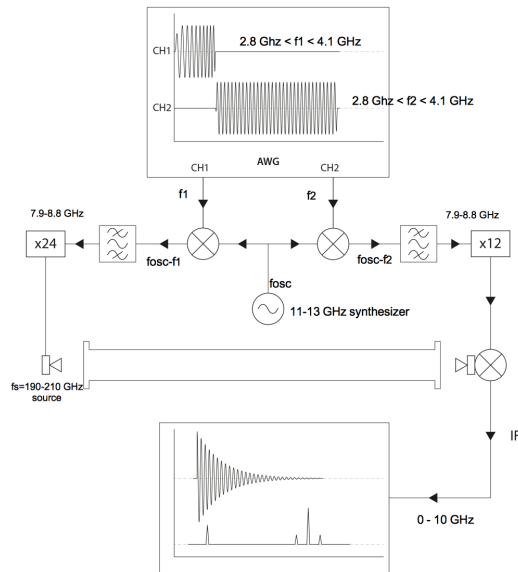

Fig. 1. mmWCP experiment

The mmWCP is generated by mixing the AWG CH1 with a fixed oscillator before being frequency-multiplied to the 190 to 210 GHz range. It is launched into free space using a diagonal horn antenna and propagated through the sample chamber. A second diagonal horn antenna is used to couple the molecular FID signal to the sub-harmonic mixer. The other ports of the mixer are used to provide the local oscillator (LO) signal and extract the intermediate frequency (IF). The IF signal is recorded using a fast oscilloscope while being triggered by a timing signal generated by the AWG. A large number of measurement cycles are averaged before applying a FFT to obtain the spectrum. The experiment can detect line intensities of the order of 10^{-26} cm^{-1}/molec.cm^{-2} in few seconds and has the possibility to scan over 10 GHz in one shot [2].

Theory

Polarization phase - The measured molecular signal is proportional to the gas polarization at the end of the chirped pulse T_c. At this stage we used the optical Bloch equations [3, 4] to describe the evolution of an isolated molecular system for which 2 energy levels |a> and |b> are probed. We will suppose that the system is submitted to an electric field **E** with a linear time dependent pulsation:

The optical Bloch equations are then given by :

$$\mathring{z}(t) = -(\tau_2 + i\omega_0)z(t) - i\varepsilon(t)W(t)$$
$$\mathring{W}(t) = -\tau_1(W(t) - W_{eq}) + \frac{1}{2i}(\varepsilon^*(t)z(t) - \varepsilon(t)z^*(t)) \tag{1}$$

$$\varepsilon(t) = \Omega_0 e^{-i[(\omega_0 - c\Delta\omega)t + \frac{\Delta\omega}{2T_c}t^2]} \tag{2}$$

$$\Omega_0 = \frac{\mu_{ab}.E_0}{\hbar} \quad \text{and} \quad \omega(t) = \omega_0 - c\Delta\omega + \frac{\Delta\omega}{T_c}t \tag{3}$$

where z(t) is the polarization, W(t) the difference population of the 2 levels, W_{eq} the difference at the thermodynamic equilibrium, τ_1 and τ_2 are the inverse of relaxation times of levels and dipoles respectively, Ω_0 is the Rabi frequency, T_c is the duration of the chirp, c is a unitless parameter describing the molecular resonance position in the chirped pulse ($0<c<1$ and $\omega(cT_c) = \omega_0$) and $\Delta\omega$ is the pulsation extension of the chirp.

In order to find a solution, at least in a first approximation, we solve in the equations (1) the one containing $\mathring{z}(t)$ while considering W(t) given, and the other one while considering z(t) given. Two uncoupled first-order differential equations are therefore obtained providing a general formulation of the solution. Then, considering the initial conditions (z(0)=0 and W(0)=W_{eq}), we have

$$z(t) = -i\int_0^t e^{-(i\omega_0 + \tau_2)(t-x)}\varepsilon(x)W(x)dx$$
$$W(t) = W_{eq} + \frac{1}{2i}\int_0^t e^{-\tau_1(t-x)}(\varepsilon^*(x)z(x) - \varepsilon(x)z^*(x))dx \tag{4}$$

We can write the 2 functions as series:

$$z(t) = z^{(0)}(t) + z^{(1)}(t) + z^{(2)}(t) + \dots$$
$$W(t) = W^{(0)}(t) + W^{(1)}(t) + W^{(2)}(t) + \dots$$

and find the solutions by successive approximations:

$$z^{(n+1)}(t) = -i\int_0^t e^{-(i\omega_0+\tau_2)(t-x)}\varepsilon(x)W^{(n)}(x)\,dx$$
$$W^{(n+1)}(t) = \frac{1}{2i}\int_0^t e^{-\tau_1(t-x)}(\varepsilon^*(x)z^{(n)}(x)-\varepsilon(x)z^{(n)*}(x))\,dx \quad (5)$$

Taking the initial conditions ($z(0)=0$ and $W(0)=W_{eq}$), only the odd terms of the z-series and the even terms of the W-series remain. We will work with $z^{(1)}(t)$ and $W^{(0)}(t)=W_{eq}$ and do a changing variable to simplify the equations (rotating frame):

$$\xi^{(1)}(t)=z^{(1)}(t)e^{i[(\omega_0-c\Delta\omega)t+\frac{\Delta\omega}{2T_c}t^2]} \quad (6)$$

Then we can show that for $t=T_c$:

$$\xi^{(1)}(T_c)\approx\rho_{app}e^{i\theta_{app}}+\tilde{\xi} \quad (7)$$

with

$$\rho_{app} = \frac{\sqrt{2\pi}\,\Omega_0 W_{eq}}{\sqrt{\Delta\omega}}\sqrt{T_c}\exp[\frac{-T_c}{T_2}(1-c)]$$
$$\theta_{app} = (1-c)^2\frac{\Delta\omega}{2}T_c-\frac{3}{4}\pi \quad (8)$$
$$\tilde{\xi} = \frac{W_{eq}\Omega_0}{\Delta\omega}(\frac{1}{1-c}+\frac{1}{c}\exp[i\frac{\Delta\omega}{2}T_c(1-2c)])\exp[\frac{-T_c}{T_2}(1-c)]$$

ρ_{app} (which is positive) represents the amplitude of $\zeta^{(1}(T_c)$, θ_{app} its phase and $\tilde{\xi}$ induces a small oscillation. In particular ρ_{app}, tends to 0 when T_c tends to 0, increases until it reaches a maximum when $T_c=\frac{T_2}{2(1-c)}$ with value $\frac{\sqrt{2\pi}}{e}\frac{\sqrt{T_c}}{\Delta\omega}W_{eq}\Omega_0$ and then it decreases toward 0 as $T_c\rightarrow+\infty$. The approximation which retains ρ_{app} is already very good to describe the system behavior.

Free Induction Decay (FID) – In this phase, the Rabi frequency vanishes and the optical Bloch equations simplify [3]. Using an heterodyne detection scheme, we can demonstrate that the output signal is :

$$S(t')=B\sqrt{\frac{T_c}{\Delta\omega}}e^{\frac{-T_c}{T_2}(1-c)}[e^{\frac{-t'}{T_2}-\frac{t'^2\Delta\omega_D^2}{4}}\cos(\omega_{IF}t'+\Phi)] \quad (9)$$

where $t'=t-T_c$ and B is a constant depending of the experiment (amplifiers, mixers …). Applying a FFT, we can access the signal amplitude at the intermediate frequency:

$$A_{TF}(\nu_{IF})=\frac{B}{\sqrt{\Delta\omega}}\sqrt{T_c}\exp[\frac{-T_c}{T_2}(1-c)] \quad (10)$$

Experimental results

We compared the theoretical model we obtained with experimental data recorded with carbonyl sulfide gas (OCS). We chose the 17->16 rotational line centered at 206.745 GHz. The output signal amplitude at the IF have been measured for different gas pressure and different positions of the molecular resonance in the CP described by the c parameter. The figure 2 compares experimental measurements and analytical modelisations for 3 different c values. A very good agreement is obtained between experimental data (blue points) and model (red curve) for a 1 GHz extension chirp and for a 100 µbar gas pressure (collisional width larger than Doppler width).

Conclusion

We used a mathematical method by successive approximations to solve the optical Bloch equations and to get an analytical formula giving the output signal of a chirped pulse experiment. This will be useful for absolute intensity lines measurements and to optimize the pulse duration to obtain the best signal to noise ratio.

(a) c = 0.1

(b) c=0.5

(c) c = 0.9
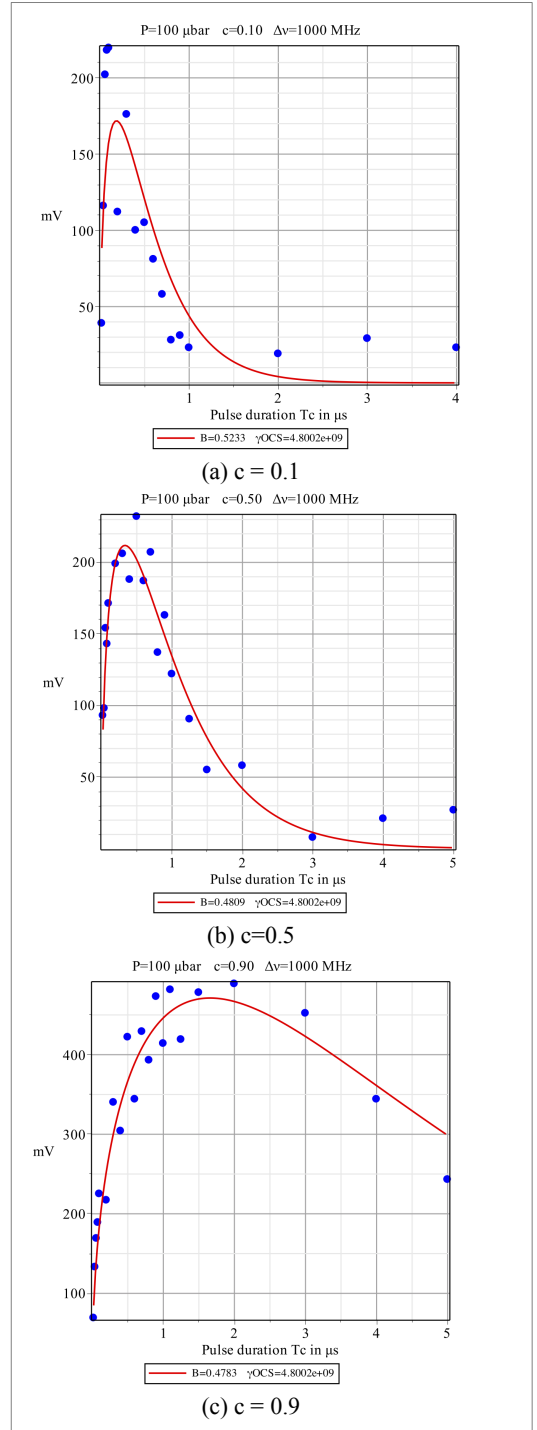
Fig. 2. Output signal amplitude $A_{TF}(\nu_{IF})$, function of pulse duration T_c, recorded for OCS at 206.745 GHz with line resonance position c as parameter. Comparison of experimental data (blue points) and model (red curve) from equation (10)

References

1. *K. M. Hickson, P. Caubet and J.-C. Loison, J. Phys. Chem. Lett, 4, 2843, 2013.*

2. *F. Hindle, C. Bray, K. Hickson, D. Fontanari, M. Mouelhi, A. Cuisset, G. Mouret, and R. Bocquet, Journal of Infrared, Millimeter, and Terahertz Waves, vol. 39, no. 1, pp. 105–119, 2018.*

3. *P. Meystre and M. Sargent III, Elements of quantum optics 3rd edition. Springer, 1999.*

4. *J. C. McGurk, T. G. Schmalz, and W. H. Flygare, J. Chem. Phys, vol. 60, no. 11, pp. 4181–4188, 1974.*

Terahertz induced optical second harmonic generation from dielectric interfaces: mechanism and application

S.B. Bodrov[1,2] Yu.A. Sergeev[2], A.I. Korytin[2], M.Y. Emelin[2], M.Y. Ryabikin[2] and A.N. Stepanov[2]

[1]University of Nizhny Novgorod, Nizhny Novgorod 603950 Russia, bosbor@ufp.appl.sci-nnov.ru
[2]Institute of Applied Physics of the Russian Academy of Sciences, Nizhny Novgorod 603950 Russia

Optical second harmonic (SH) generation from interfaces of different materials is widely used for surface studies. The surface breaks the symmetry allowing SH generation even in isotropic media. The quality of the surface as well as presence of an additional layers on the surface significantly influence on SH generation. Also, it was shown that application of constant external electric field changes the magnitude of the generated SH signal [1]. In Ref. [2] it was proposed to use a weak THz electric field to modulate SH generation from surface of nontransparent optical material (silicon) as a method to measure THz field waveform. Here we propose to use THz induced SH generated by femtosecond laser radiation to detect optically hidden layers (glue) placed not only on the surface but also into a bulk of transparent materials (quartz). We showed that existence of terahertz radiation influences on SH generation only from the interfaces (glue-quartz, air-quartz) and not from the bulk of the quartz. To explain this effect a model based on interaction of electromagnetic radiation with an electron in coulomb potential biased by embedded surface electric field was proposed and analyzed.

A Ti:Sapphire laser system (1 mJ, 1 kHz, 70 fs) was used in our experiment. The optical beam was divided into two parts (see Fig. 1). The first pulse generated THz radiation in a LiNbO3 crystal by the tilted-front technique [3]. The THz pulse (the waveform is shown in Fig. 2(a)) was focused on the sample collinear with a probe (weak) femtosecond optical pulse. The sample was fabricated by cementing of two 0.9 mm fused quartz plates by glue with thickness of about several μm. The generated optical SH was detected by PMT in reflection and transmittance setups. In the first setup the sample was placed at 45° to incident probe pulse and PMT detected reflected optical SH. In the second setup the probe optical pulse propagated normally to the incident surface of the sample and PMT detected transmitted optical SH.

Figure 2(b) shows the SH signal as a function of delay time between optical and THz pulses in the transmittance setup (the similar signal but two orders less magnitude was measured in the reflection setup). Due to different velocities of THz and optical pulses, their interaction occurs at different points inside the sample. The measured SH signal at $t = 0$ corresponds to the signal from the entrance surface of the sample, at $t = 1.4$ ps – from the interface glue-quartz, and at $t = 2.7$ ps – from the output boundary of the sample. The dependence obtained in Fig. 2 (b) demonstrates the possibility of determining the presence of internal boundaries in the material that are not visible in the

optical range. With the known values of the refractive indexes for optical and THz radiation, one can find a depth of internal inhomogeneity.
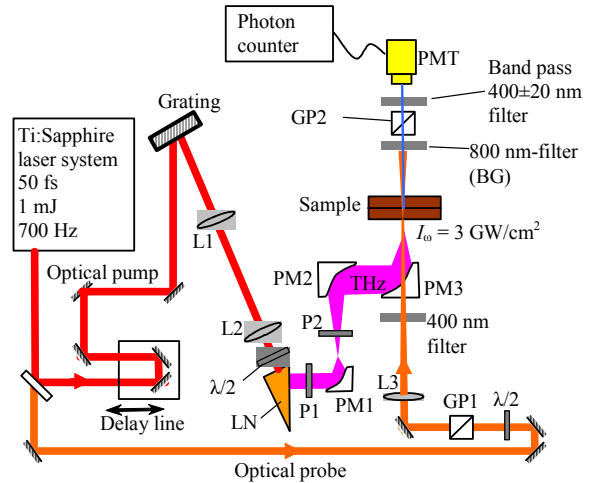
Fig. 1. (a) Experimental setup. LN – LiNbO$_3$ crystal; PM1, PM2 and PM3 – parabolic mirrors; GP1,GP2 – Glan prisms; PMT – photo multiplier tube; P1, P2 – THz polarizers.
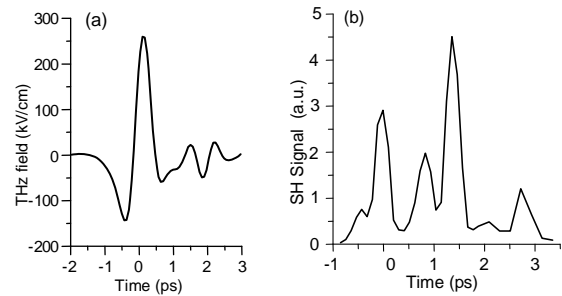
Fig. 2. (a) THz waveform. (b) THz induced optical SH generation from cemented quarts plates.

The fundamental feature of the dependence in Fig. 2(b) is absence (or negligible small value) of SH signal from the bulk. Indeed, the SH in the bulk of isotropic material can be generated by the fundamental harmonic via cubic nonlinearity in the presents of external constant (or low-frequency) field. Thus, the optical and THz pulses should intersect in space. Due to material dispersion the optical and THz pulses interact in the bulk on a walk-off distance $L_w = c\tau / (n_{THz} - n_{opt})$, where τ – THz pulse duration, n_{THz} and n_{opt} – terahertz and optical refraction coefficients, respectively. Taking $\tau = 500$ fs we have for fused quartz $L_w = 300$ μm. Changing the time delay results to moving the position of interaction region inside the sample. If the thickness of the sample (1.8

mm) is more than the walk-off length (as in our experiment) the dependence of SH signal on time delay should have step-like profile with rising and falling times $\tau \approx 0.5$ ps (with possible modulation due to short ~ 10 μm coherent length between first and second optical harmonics). Such signal was not measured in the experiment. At the same time, the signal tracing the form of THz intensity was well observed that indicates the presents of a source of the second harmonic only near the interfaces.

To qualitatively explain the above-discussed experimental result we considered a nonlinear response of hydrogen-like atom in the field of optical and THz radiation. The presence of the interface was modeled by applying additional constant field with corresponding orientation. The simulation was based on 2D and 3D numerical solution of Schrödinger equation. It was shown that near the surface the SH response has a resonance defined by the value of the constant field. Switching-off of the constant field (that corresponds to moving atom into the bulk) leads to a decrease in the second harmonic by several orders of magnitude in agreement with experimental data. This single-particle theory gives a good qualitative explanation of experimental results. For more accuracy (and better quantitative agreement with experimental data) one should take into account the number of atoms in the bulk and near the surface as well as the dynamics of their radiation.

References

[1] O. A. Aktsipetrov, A. A. Fedyanin, A. V. Melnikov, E. D. Mishina, A. N. Rubtsov, M. H. Anderson, P. T. Wilson, M. ter Beek, X. F. Hu, J. I. Dadap, and M. C. Downer. Dc-electric-field-induced and low-frequency electromodulation second-harmonic generation spectroscopy of Si(001)−SiO2 interfaces // Phys. Rev. B. 1999. V. 60. P. 8924.

[2] A. Nahata and T.F. Heinz. Detection of freely propagating terahertz radiation by use of optical second-harmonic generation. // Opt. Lett. 1998. V. 23. P. 67.

[3] S.B. Bodrov, A.A. Murzanev, Y.A. Sergeev, Y.A. Malkov, and A.N. Stepanov. Terahertz generation by tilted-front laser pulses in weakly and strongly nonlinear regimes. // Appl. Phys. Lett. 2013. V. 103. P. 251103.

Coherent control of electron-nuclear states of rare-earth ions in crystals using radio-frequency and microwave radiation

<u>M. R. Gafurov</u>, G.V. Mamin, E.I. Baibekov, I. N. Kurkin,

F.F. Murzakhanov, S.B. Orlinskii

Kazan Federal University, Kazan, Russian Federation, mgafurov@gmail.com

Electron and/or nuclear spin states are well-known for their use as potential qubits for quantum computing [1]. Single-qubit operation on an electron spin-1/2 qubit can be performed by using microwave (mw) pulse with frequency matching the energy of the transition between the two spin states. Double resonance techniques allow one to manipulate more than two quantum states simultaneously during the pulse sequence. Thus, certain two-qubit operations can be implemented [2].

We have performed electron-nuclear double resonance (ENDOR) and double electron-electron resonance (DEER) manipulations of electronic and nuclear spin states of trivalent gadolinium impurity ions in $CaWO_4$ host crystal. The sample of $CaWO_4$:Gd^{3+} (0.01 at. %) single crystal was grown in Kazan Federal University by the Czochralski method. Experimental studies were done by using helium flow cryostats at X-band Bruker Elexsys E580 spectrometer (T = 5-25 K, microwave frequency $\nu \approx 9.7$ GHz). Pulsed electron paramagnetic resonance spectrum of Gd^{3+} ion in $CaWO_4$ host crystal (magnetic field **B** $\parallel c$ axis) is shown in Fig. 1.
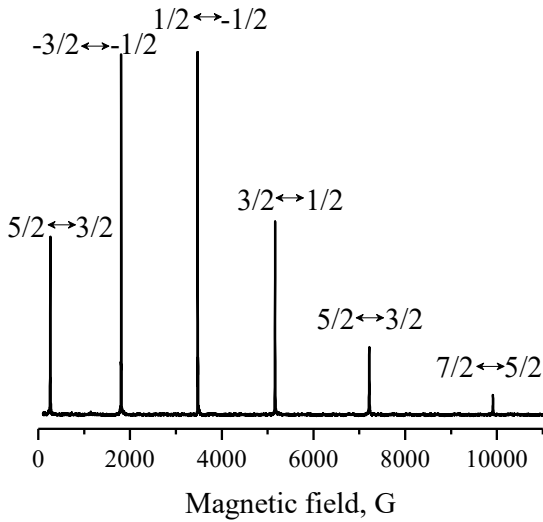

Fig. 1. Pulsed EPR of Gd^{3+} ion in $CaWO_4$ crystal, **B** $\parallel c$ axis

It consists of six resonance lines corresponding to various $S_{z1} \rightarrow S_{z2}$ transitions between the states of the ground spin-7/2 multiplet. Containing 8 lowest-energy spin states ($S_z = -7/2 \div 7/2$), Gd^{3+} ion can be viewed as model three-qubit system. Single-qubit manipulations in this system have been demonstrated in our previous work [3]. There, mw pulse excited one of the six transitions (chosen by appropriately tuned

magnetic field), and the resulting Rabi oscillations were recorded in the time domain of the mw pulse.

Since the impurity gadolinium ions contain odd ^{155}Gd and ^{157}Gd isotopes with nuclear spin $I = 3/2$ (natural abundance 14.8% and 15.6%, respectively), one can use pulsed ENDOR in order to manipulate both the electron and nuclear spin states of these isotopes simultaneously. The total basis of $8 \cdot 4 = 32$ electro-nuclear states would expand the possible quantum algorithm to 5-qubit operations. In order to demonstrate the control of both the electron and nuclear spin states simultaneously, we used Davies ENDOR pulse sequence [4]: an initial mw π pulse is followed by the radiofrequency (rf) π pulse, then the remaining electron state is probed by the mw two-pulse spin-echo sequence. If the rf pulse frequency matches the nuclear transition, the final echo intensity changes. An example of ENDOR spectrum corresponding to $5/2 \rightarrow 3/2$ electronic transition near $B = 244$ G swept in the range 0-50 MHz of the rf pulse is shown in Fig. 2. Here, four peaks corresponding to certain electronuclear transitions (two pairs corresponding to ^{155}Gd and ^{157}Gd nuclear spin flips) are present. The positions of the peaks agree well with our theoretical estimations.
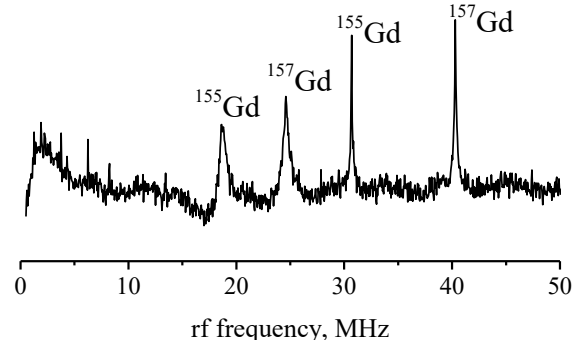
Fig. 2. Pulsed Davies ENDOR of Gd^{3+} in $CaWO_4$ crystal, B = 244 G is directed along the crystal c axis, T = 20 K

Since the positions of the lines in Fig. 1 are orientation-dependent [5], one can choose an appropriate direction of **B** with respect to the crystallographic axes, so that two electronic transitions lie within the 800 MHz bandwidth of the two-frequency DEER equipment. EPR spectrum in certain orientation (13 degrees between **B** and c axis) is shown in Fig. 3. There, two high-field transitions, $5/2 \rightarrow 3/2$ and $7/2 \rightarrow 5/2$, involving three electronic levels, are drawn together, the corresponding resonance fields differ by ≈ 100 G. Then, the following two-frequency pulse sequence has been applied: $\pi/2(\nu_1) - \pi/2(\nu_1) - \pi(\nu_2) - \pi/2(\nu_1)$, where the indices in brackets denote the mw

pulse frequency. There, ν_1 = 9.74 GHz corresponded to the resonant transition 5/2→3/2 at 7210 G, while ν_2 was swept in the range 9.3-10 GHz. When ν_2 did not match any transition, a usual three-pulse stimulated echo for 5/2→3/2 transition was recorded. However, when ν_2 matched either 5/2→3/2 or 7/2→5/2 transition energy, the third (flipping) π pulse inversed the populations of the two involved spin states, so that the echo intensity was decreased.
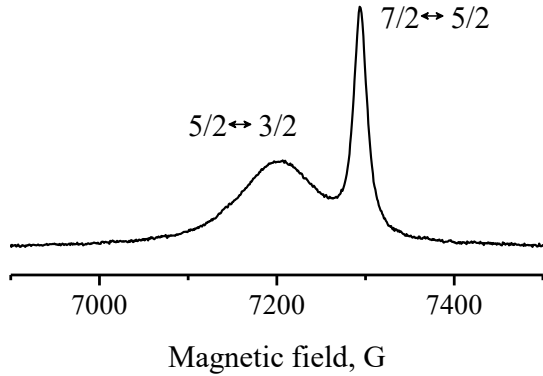
Fig. 3. A part of pulsed EPR spectrum of Gd:CaWO$_4$ when **B** is directed at an angle of 13 degrees with respect to crystal c axis
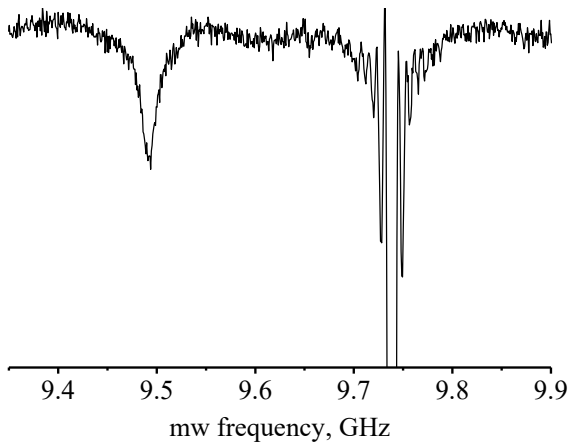

Fig. 4. DEER of Gd^{3+} in CaWO$_4$ crystal, B = 7210 G, T = 20 K, see text for full description

The coherence loss associated with the third pulse resulted in two dips in the echo intensity: at $\nu_2 = \nu_1$ (original 5/2→3/2 transition), and at ν_2 = 9.49 GHz (7/2→5/2 transition), see Fig. 4. An estimated magnitude of the observed hole burnt is ~ 10% of the one at $\nu_2 = \nu_1$, this figure is attributed to the inhomogeneous broadening of the resonance lines. In order to measure the corresponding coherence time of the three-state ensemble (a qutrit), we have recorded the transient

nutation of the 7/2→5/2 coherence. There, the duration of the third ν_2 pulse resonant with 7/2→5/2 transition was varied in the range 0-4 μs, while the duration of the π(ν_2) pulse was ≈ 180 ns. The resultant echo intensity vs. the pulse duration is shown in Fig. 5.
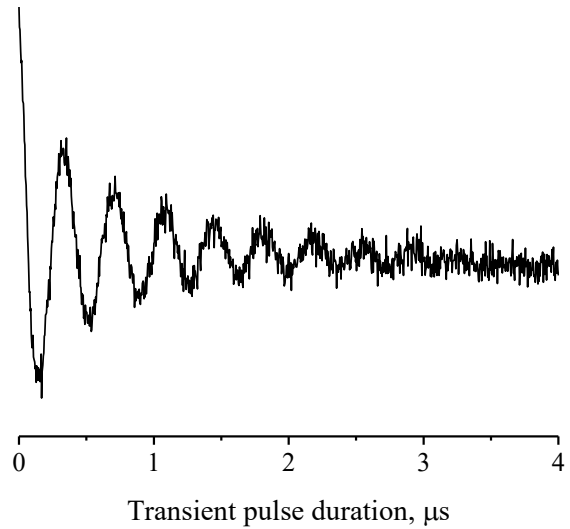
Fig. 5. Oscillations of the 5/2→3/2 transition coherence implemented by pulsed DEER, see text for full description

Finally, we have demonstrated electron-electron and electron-nuclear spin manipulations of Gd^{3+} ion in CaWO$_4$ crystal. The results suggest that the studied system is perspective for multiqubit implementation in quantum computing.

References

1. *DiVincenzo, D. P.* Quantum computation // *Science* 1995. V. 270. P. 255–261.

2. *Jelezko, F., Gaebel, T., Popa, I., Domhan, M., Gruber, A., Wrachtrup, J.* Observation of coherent oscillation of a single nuclear spin and realization of a two-qubit conditional quantum gate // *Physical Review Letters* 2004. V. 93. P. 130501.

3. *Baibekov, E. I., Gafurov, M. R., Zverev, D. G., Kurkin, I. N., Rodionov, A. A., Malkin, B. Z., Barbara, B.* Coherent spin dynamics in a gadolinium-doped CaWO$_4$ crystal // *Physical Review B* 2017. V. 95. P. 064427.

4. *Davies, E. R.* A new pulse ENDOR technique // *Physics Letters A* 1974. V. 47. P. 1–2.

5. *Vazhenin, V.A., Guseva, V.B., Artemov, M.Y.* Effects of averaging of spin packets of interacting resonances in Gd^{3+} EPR spectra of scheelites // *Physics of the Solid State* 2003. V. 45. P. 2271–2275.

Terahertz time-domain spectroscopy of astrophysical ice analogs: A pilot study

A. A. Gavdush[1,2], B. M. Giuliano[3], B. Müller[3], G. A. Komandin[1],
M. E. Palumbo[4], G. A. Baratta[4], C. Sciré[4],
S. O. Yurchenko[2], K. I. Zaytsev[1,2], A. V. Ivlev[3], and P. Caselli[3]

[1]Prokhorov General Physics Institute of the Russian Academy of Sciences, Moscow, Russia, arsenii.a.gavdush@gmail.com
[2]Bauman Moscow State Technical University, Moscow, Russia
[3]Max-Planck-Institute für extraterrestrische Physik, Garching bei München, München, Germany
[4]Osservatorio Astrofisico di Catania, Catania, Italy

Ices are one of the most common kinds of dense matter in the Universe. There are more than 180 various molecular astrophysical ices, including H_2O, CO, CO_2, CH_3OH, etc. [1]. Surface chemical processes on icy mantles of dust particles play an important role in formation of new molecules, including biologically relevant organic species [2, 3]. Therefore, thorough studies of the ice properties may shed light to such astrophysical problem, as understanding the origin of the volatiles and organics – the building blocks of life – in space and then on the early Earth.

Analysis of astronomical observations in different ranges of electromagnetic spectrum is the main tool for experimental studies of ices in the Universe. These observations employ mostly a mid-infrared (IR) range of wavelengths [1, 4], but also cover far-IR and terahertz (THz) ranges, provided by such space telescopes, as Hershel [5] and SOFIA [6]. A cornerstone of proper interpretation of these observations is their comparison to IR and THz spectra of astrophysical ice analogs obtained in laboratory conditions. Recent works were mainly dedicated to the analysis in mid-IR frequency region [1], with only a few works concerned on THz spectroscopy [7, 8]. However, in spite of its importance, the presently available data related to spectroscopy in IR and THz range are still incomplete or even have not been performed for a lot of ice compounds, to our knowledge.

In the present work, we apply previously developed method [9-13] for reconstruction of both real and imaginary parts of dielectric permittivity, using the THz time-domain spectroscopy (TDS). This technique allows us to measure optical properties of astrophysical ice analogs in a broad range of wavelengths, that is required for detailed study of radiative transfer in ice mantles of astrophysical dust particles. We developed an experimental setup allowing simultaneous growth and THz TDS of thin ice films of different molecular compositions.

The experimental setup for the spectroscopic measurements is composed closed-cycle He cryostat and THz time-domain pulsed spectrometer (TPS). The cryostat is mounted on a motor controlled translational stage to tune its position with respect to the THz beam. The cryocooler vacuum chamber is equipped with four ports for optical access and for the gas inlet. Optical windows and a substrate for the ice growing are made of high-resistivity float-zone silicon (HRFZ-Si) with different thickness, the smallest one for the substrate, in order to suppress multiple resonances in the THz spectra. The pumping station that operates with gas mixture for ice sample deposition is composed of a turbomolecular pump combined with a backing rotary pump. The THz TPS used for the present work has been basically purchased from the Batop GmbH, and it is coupled with two photoconductive antennas made of low-temperature grown gallium arsenide and a femtosecond laser with a pulse repetition rate of 100 MHz and an average input power of 65 mW. Further technical details on an experimental setup one can find in the upcoming work at Astronomy & Astrophysics journal [11].

Growth of the ices on the substrate is organized using standard technique using vapor deposition on the cold substrate in the vacuum chamber. To attain ice thickness of a mm order, fast deposition regime is employed. The first experiments were performed with ice of CO, deposited at 14 K in a several deposition regimes, with 4, 5 and 6 min deposition steps, and up to the total 30 min deposition time.

The reconstruction procedure of the optical properties of ice layers is organized in the same manner as in previous works [9-13]. The signal propagated through the empty vacuum chamber at 14 K was used as the reference one for analysis of the sample signal propagated through the chamber with grown ice layers on the substrate. Then, the time-domain signals (reference ballistic and sample satellite pulses) were analyzed to have initial estimations of ice layers' thicknesses and a real part of the sample refractive index, to enhance the accuracy of data post processing. Reliability of the employed approach is confirmed by independent measurements of the sample thickness [15], and observed linear increase of the total initial thickness of ices in different deposition regimes. In result [14], the optical properties of CO ice were measured in the range of 0.3–2.0 THz, with a clearly expressed Lorentz-like peak centered near 1.5 THz, which stands in a good agreement with previous studies [16, 17].

References

1. *Boogert, A. C. A., Gerakines, P. A., and Whittet, D. C. B.* Observations of the icy universe // Annual Review of Astronomy and Astrophysics 2015. Vol. 53, P. 541–581.

2. *Öberg K. I.* Photochemistry and Astrochemistry: Photochemical Pathways to Interstellar Complex Organic

Molecules // Chemical Reviews 2016. V. 116, No 17 P. 9631–9663.

3. *McGuire, B. A., Carroll, P. B., Loomis, R. A.., Finneran, I. A., Jewell, P. R., Remijan, A. J., Blake, G. A.* Discovery of the interstellar chiral molecule propylene oxide (CH3CHCH2O) // Science 2016. V. 352, No. 6292. P. 1449–1452.

4. *van Dishoeck, E. F.* Astrochemistry of dust, ice and gas: introduction and overview // Faraday Discuss. 2014. V. 168, P. 9-47.

5. *Doyle, D., Pilbratt, G. and Tauber, J.* The Herschel and Planck Space Telescopes // Proceedings of the IEEE 2009. V. 97, No. 8. P. 1403-1411.

6 *Gehrz, R. D., Becklin, E. E., de Pater, I., Lester, D. F., Roellig, T. L. and Woodward, C. E.* A new window on the cosmos: The Stratospheric Observatory for Infrared Astronomy (SOFIA) // Advances in Space Research 2009. V. 44, No. 4. P. 413-432.

7. *Allodi, M. A., Ioppolo, S., Kelley, M. J., McGuire, B. A., and Blake, G. A.* The structure and dynamics of carbon dioxide and water containing ices investigated via THz and mid-IR spectroscopy // Physical Chemistry Chemical Physics 2014. V. 16, No. 8. P. 3442-3455.

8. *McGuire, B. A., Ioppolo, S., Allodi, M. A., and Blake, G. A.* THz time-domain spectroscopy of mixed CO2-CH3OH interstellar ice analogs // Physical Chemistry Chemical Physics 2016. V. 18, No. 30. P. 20199-20207.

9 *Zaytsev, K. I., Gavdush, A. A., Lebedev, S. P., Karasik, V. E., and Yurchenko S. O.* A Method of Studying Spectral Optical Characteristics of a Homogeneous Medium by Means of Terahertz Time-Domain Spectroscopy // Optics and Spectroscopy 2015. V. 118, No. 4. P. 552–562.

10. *Zaytsev, K. I., Gavdush, A. A., Chernomyrdin, N. V., and Yurchenko, S. O.* Highly Accurate In Vivo Terahertz Spectroscopy of Healthy Skin: Variation of Refractive Index and Absorption Coefficient along the Human Body //

IEEE Transactions on Terahertz Science and Technology 2015. V. 5, No. 5. P. 817-827.

11. *Yakovlev, E. V., Zaytsev, K. I., Dolganova, I. N., Yurchenko, S. O.* Non-Destructive Evaluation of Polymer Composite Materials at the Manufacturing Stage Using Terahertz Pulsed Spectroscopy // IEEE Transactions on Terahertz Science and Technology 2015. V. 5, No. 5. P. 810 – 816.

12. *Zaytsev, K. I., Kudrin, K. G., Karasik, V. E., Reshetov, I. V., Yurchenko S. O.* In vivo terahertz spectroscopy of pigmentary skin nevi: Pilot study of non-invasive early diagnosis of dysplasia // Applied Physics Letters 2015. V. 106, No. 5 P. 053702.

13. *Zaytsev, K. I., Gavdush, A. A., Karasik, V. E., Alekhnovich, V. I., Nosov, P. A., Lazarev, V. A., Reshetov, I. V., Yurchenko, S. O.* Accuracy of sample material parameters reconstruction using terahertz pulsed spectroscopy // Journal of Applied Physics 2014. V. 115, P. 193105.

14. *Giuliano, B. M., Gavdush, A. A., Müller, B., Zaytsev, K. I., Palumbo, M. E., Baratta, G. A., Sciré, C., Komandin, G. A., Yurchenko, S. O., Ivlev, A. V., and Caselli, P.* Broadband spectroscopy of astrophysical ice analogs. I. Direct measurement of complex refractive index using terahertz pulsed spectroscopy // Astronomy & Astrophysics manuscript.

15. *Baratta, G. A., Palumbo, M. E.* Infrared optical constants of CO and CO2 thin icy films // J. Opt. Soc. Am. A 1998. V. 15, No. 12. P. 3076-3085.

16. *Anderson, A., Leroi, G. E.* Far-Infrared Spectra of Crystalline Nitrogen and Carbon Monoxide // The Journal of Chem. Phys. 1966. V. 45, P. 4359.

17. *Ron, A., Schnepp, O.* Lattice Vibrations of the Solids N_2, CO_2, and CO // The Journal of Chem. Phys. 1967. V. 46, No. 10 P. 3991-3998.

Accurate broadband THz molecular spectroscopy

Krupnov A.F., Belov S.P., Tretyakov M.Yu., Golubiatnikov G.Yu., Parshin V.V.,
Koshelev M.A., Serov E.A., Vilkov I.N., Makarov D.S., Bubnov G.M.,
Leonov I.I., Chernova A.I., Andriyanov A.F., Shkaev A.P.

Institute of Applied Physics RAS, Nizhny Novgorod, Russia, koma@ipfran.ru

Teraherz (THz) molecular spectroscopy is a powerful instrument for solving both fundamental and applied problems. Molecular physics, remote sensing, chemical and isotopic analysis, medicine (breath analysis) are among the applied problems which can be solved using molecular spectroscopy methods.

Sensitivity, resolution and operating pressure range are the most crucial parameters of any spectrometer. High resolution of gas spectrometers allows observing the lines that uniquely as fingerprints characterize molecules, opening up vast possibilities, on the one hand, for the outlook at the molecular level, and, on the other hand, for qualitative and quantitative analysis of gas mixtures. High sensitivity of the spectrometer allows the significant expand of the range of the studied objects. The higher the sensitivity, the greater the number of lines which can be observed in the experiment. Finally, the wider the pressure range, the extensively the knowledge about intermolecular interaction which is required for adequate interpretation and modeling of the molecular spectra. However, use of only type one spectrometer cannot guarantee the data reliability. Use of several instruments of the different principal of operation allows obtaining more information on molecular spectra with higher accuracy and reliability.

In this report we present a complex of broadband THz/subTHz spectrometers (see [1] and references therein) with complementary abilities developed in IAP RAS. The complex consists of three spectrometers with different methods of spectra recording covering the widest pressure range from a part of mTorr to a few atmospheres. All of them utilize backward wave oscillator (BWO) as a radiation source which frequency is stabilized by a phase lock loop (PLL) against a harmonic of a microwave frequency synthesizer and cover a frequency range from 30 GHz to about 1 THz.

The first spectrometer is a conventional video spectrometer [2] operating in a pressure range from a part of mTorr to about 1 Torr. The principle of its operation consists in detection of a change of radiation power passed through the gas cell filled with the gas investigated. A spectrometer cell is a 2 m long and 113 mm diameter stainless-steel tube with polished internal cell surface. Optical vacuum windows are made of high-density polyethylene and are cone-shaped to reduce the standing-wave amplitude between them. The spectrometer allows accurate measurement of line frequency, intensity, pressure broadening and shifting parameters. For precise measurement of line positions with subkHz uncertainty, method of nonlinear coherent spectroscopy (Lamb-dip method) was implemented in the spectrometer. A typical line recording obtained using video spectrometer is presented in Fig. 1.
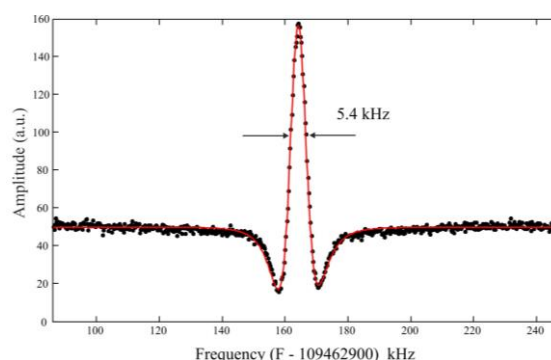

Fig. 1. Lamb-dip observed in OCS rotational transition J=9-8. Frequency detuning is shown from 109463.063 MHz. Collisional line width (HWHM) obtained from the fit to the Lorentz shape is 6.56(3) kHz. Doppler width is 81 kHz.

The second instrument of the spectroscopic complex is a spectrometer with radio-acoustic detector of absorption signal [3]. The output signal of the RAD spectrometer is proportional to the radiation power absorbed by the gas. It brings us to two main advantages of the RAD method: i) almost zero baseline (comparing to a video spectrometer); ii) the spectrometer sensitivity is increased as radiation power increases. The operating pressure range of the spectrometer is in interval from 10 mTorr to 10 Torr. The spectrometer is the best suited for the line shape analysis and measuring pressure broadening and shifting parameters of the lines and their speed-dependence in a wide temperature range. One more advantage of the RAD spectrometer is high enough sensitivity at rather compact size of the gas cell (10 cm long and 2 cm in diameter). It allows easy shielding of the gas cell from the ambient magnetic fields that is important for studying the paramagnetic lines, e.g., for the lines of oxygen spectra. Typical recordings of oxygen lines obtained using RAD spectrometer are shown in Fig. 2.

At the present level of sensitivity of THz spectrometers most of spectroscopic studies are aimed at refinement of the spectroscopic information. Expanding the range of the studied objects requires significant improvement of the sensitivity. In THz range radio-acoustic detection is seemed to be the only method allowing reaching high sensitivity at reasonable recording time by increasing radiation power. It was demonstrated in our earlier study [4] that the use

of the high power coherent THz radiation of the gyro-tron allows increase of the RAD spectrometer sensitivity by at least three orders of magnitude. This opens up possibility of investigating, for example, the forbidden spectra of molecules.
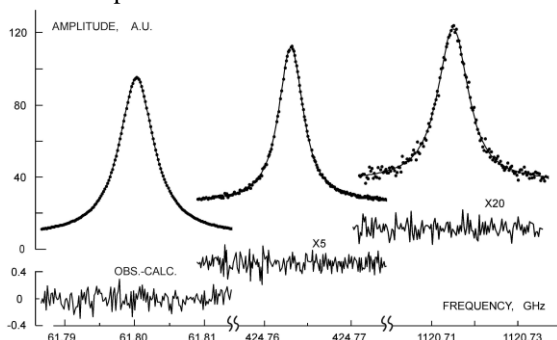
Fig. 2. Lines of the oxygen molecule obtained using RAD spectrometer (from left to right): a) fine-structure line 11+; b) rotational line (N,J)=(3,2)-(1,2); c) rotational line (N,J)=(7,6)-(5,6). The result of the line fitting to Voigt profile is shown by solid line. The residue of the fit is shown in the lower part of the figure.

In third, the resonator spectrometer [5,6] operating in a pressure range from 10 Torr up to a few atmospheres gas absorption is measured sequentially at each eigen-frequency as a change of the Q-factor of the Fabry-Perot resonator filled with the studied and non-absorbed gases, respectively. The PLL system provides fast phase-continuous frequency scan, resulted in significant progress in the spectrometer sensitivity (which now reaches $4 \cdot 10^{-9}$ cm^{-1} in terms of the absorption coefficient). A part of the atmospheric absorption spectra observed using resonator spectrometer is presented in Fig. 3. It is worth noting, that the line intensity measurements performed using the resonator spectrometer are supposed to be the most accurate comparing to other methods.
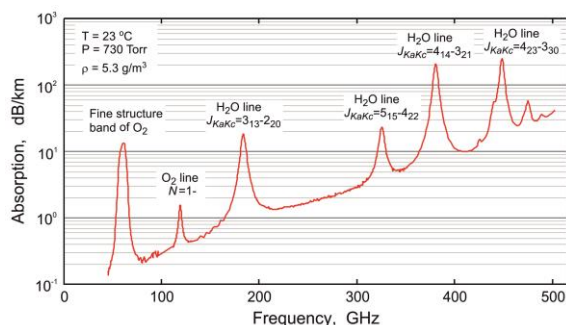
Fig. 3. Broadband experimental recording of atmospheric air spectrum obtained using resonator spectrometer.

Use of the complex of THz spectrometers allows determination of possible systematic errors. This is confirmed by a series of complementary experiments in which parameters of spectral lines measured by one spectrometer were revised by a spectrometer of another type. Coincidence of the values of the parameters measured by different spectrometers means high accuracy and reliability of the data obtained. As an example, results of the pressure broadening study for 118-GHz oxygen line [7] (RAD and resonator) and

22-GHz water line [8] (RAD and video) are presented in Fig. 4.
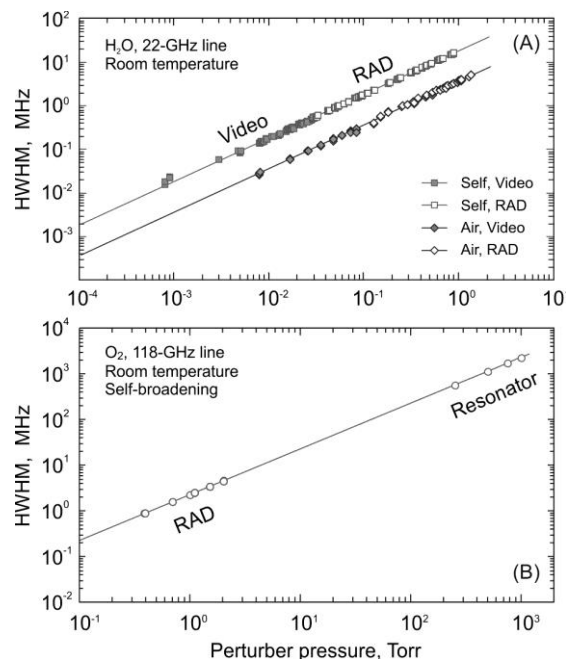
Fig. 4. Pressure dependence of the width of the (A) 22-GHz water line measured using video and RAD spectrometers and (B) 118-GHz oxygen line measured using RAD and resonator spectrometers.

References

1. *Krupnov A.F., et al.* Accurate broadband rotational BWO-based spectroscopy // J. Molec. Spectrosc. 2012. V. 280 P.110-118.

2. *Golubiatnikov G.Yu., et al.* Precision Sub-Doppler Millimeter and Submillimeter Lamb-Dip Spectrometer // Radiophysics and Quantum Electronics. 2014. V 56. N. 8–9. P. 599–609.

3. *Tretyakov M.Yu., et al.* Precise Measurements of Collision Parameters of Spectral Lines with a Spectrometer with Radioacoustic Detection of Absorption in the Millimeter and Submillimeter Ranges // Instrum. Exp. Tech. 2008. V. 51. P. 78–88.

4. *Koshelev M.A., et al.* Molecular Gas Spectroscopy Using Radioacoustic Detection and High-Power Coherent Subterahertz Radiation Sources // J. Molec. Spectrosc. 2017. V. 331 P. 9–16.

5. *Parshin V.V., et al.* Modern resonator spectroscopy at submillimeter wavelengths. // IEEE Sensors Journal. 2013 V.13. N. 1. P. 18-23.

6. *Koshelev M.A., et al.* New frontiers of modern resonator spectroscopy // submitted in IEEE Trans. THz Sci. Technol. 2018.

7. *Koshelev M.A., et al.* Accurate modeling of the diagnostic 118-GHz oxygen line for remote sensing of the atmosphere // J. Quant. Spectrosc. Radiative Transfer 2017. V. 196 P. 78-86.

8. *Koshelev M.A., et al.* Line shape parameters of the 22-GHz water line for accurate modeling in atmospheric applications // J. Quant. Spectrosc. Radiative Transfer 2018. V. 205 P. 51-58.

Pulsed magnets with high field intensity for laser-plasma experiments and TDS spectroscopy

T. Krapivnitskaia, A. Luchinin, V. Malyshev, M. Morozkin, M. Starodubtsev, M. Proyavin, A. Fokin, and M. Glyavin

Institute of Applied Physics, 46 Ulyanov Street, 603950 Nizhny Novgorod, Russia

The studies of different physical processes in presence of strong magnetic fields are one of the ever-lasting problems in experimental physics. Development of techniques and investigation of complex dynamics leads to the implementation of magnetic systems with fields more than 20 T. The laser-plasma experiments [1] and time-domain spectroscopy [2] are one of the outstanding applications for strong magnetic fields. Conventional magnetic systems based on large superconducting magnets are not convenient for ultrafast spectroscopy due to remote access to the magnet coil and unavoidable dispersive elements. The solution is to use the small-scale pulsed systems, which provide easy alignment and strong field at the same time.

Magnets for time-domain spectroscopy

Terahertz time-domain spectroscopy (THz-TDS) is ideally suited for the study of coherent low-energy dynamics in condensed matter, determining the complex conductivity of material. The terahertz frequency range is rich in collective and elementary excitations in solids, many of which have magnetic origins such as cyclotron resonance, electron spin resonance, and magnon excitations. An external magnetic field provides a powerful tool for tuning these magnetic THz excitations through Landau and Zeeman quantization of electrons' orbital and spin energies. Probing these excitations through THz-TDS in high magnetic fields can provide valuable insight into the dynamics of interacting electrons. Therefore, there is a need for developing a source of strong magnetic field, suitable for TDS.

The IAP RAS has great experience in development and production of pulsed magnetic systems, which were mainly used for high-frequency gyrotrons [3]. The record magnetic field of 50 T in a bore of 9 mm (Fig. 1) was produced for the gyrotron with 1.3 THz frequency [4] along with a number of 30 T magnets with 2 cm bore. The developed technology is based on copper magnets encased in fiberglass body with liquid nitrogen as a coolant. The cooling to cryogenic temperatures reduces the resistance of copper, lowers the heating of the coil during the pulse and provides better pulse-to-pulse stability. Resulting coil operated with 1 Hz repetition rate and successfully produced more than 3000 pulses with field > 30 T and more than 100 pulses with field > 45 T without any degradation. The magnets of this type surely can find their application in experiments with time-domain spectroscopy in strong magnetic fields.

Fig. 1. The 50 T Pulsed magnet

Magnets for laser-plasma experiments

The studies on the formation of different plasma structures in strong magnetic field are of great interest for astrophysics and inertial fusion. Different astrophysical objects could be modeled in such down-scaled laboratory experiments. Such astrophysical objects characterizes by the perturbation of the magnetic field structure and development of different magneto-hydrodynamic instabilities, which could not be studied analytically and should be studied through laboratory modeling [5].

The specially designed magnetic coil provides the needed conditions for investigation of plasma dynamics in magnetic field. The principal scheme of the setup and coil photo are presented in Fig. 2. To satisfy the requirements for the plasma formation and diagnostics the coil must have three mutually perpendicular apertures of free space inside the coil, that provide the possibility of positioning the target, irradiating the target with powerful nanosecond laser beam and observing the dynamics of plasma expansion perpendicular to the main axis of the direction of propagation of the plasma stream.
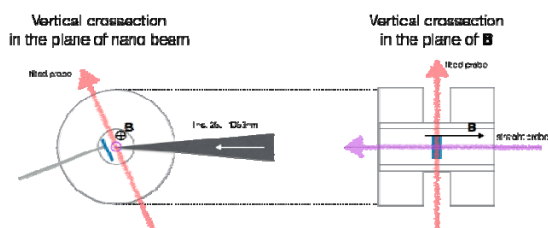

Fig. 2a. General view of the experimental setup.

Fig. 2b. The pulsed magnet photo.

In order to satisfy the requirements, the Helmholtz magnetic coil was developed and manufactured by the IAP RAS. The coil current is controlled by a capacitor discharge unit with maximum current up to 8 kA, ensuring the maximum magnetic field of 15 T. The discharge of the coil occurred over times of the order of several milliseconds. The field was considered stationary at time scales of the order of several microseconds, much larger than the times of the investigated plasma dynamics of the order of 100 ns. The magnetic field was practically uniform in the axial and radial directions at scales of the order of 20 mm, which exceeded the characteristic scales of the investigating plasma (~ 10 mm). The repetition of the magnetic field amplitude and profile was ensured by cryogenic cooling of the system with liquid nitrogen. Typically, the coil can operate with repetition rate of 1 shot per 10 minutes. The construction of the magnet allowed switching of the direction of both coils, providing the co- and counter-directional setup of the magnetic field and opening up the possibility of investigation of plasma dynamics in different conditions. The measured profiles of magnetic field for both configurations are presented on Fig. 3. The magnet

was already used in successful experiment, carried out on PEARL facility [6].
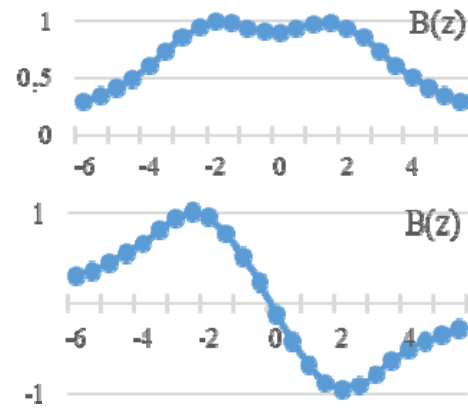
Fig. 3. Magnetic field profiles for co and counter-directional setup of coils.

Conclusion

The developed pulse magnets with fields up to 50 T and complex magnetic field structure open up the possibilities for investigation of properties of materials and laboratory modeling of astrophysical phenomena.

References

1. *Albertazzi, B. et al.* Laboratory formation of a scaled protostellar jet by coaligned poloidal magnetic field // Science, 2014, V. 346, Vol. 346, No 6207, P. 325-328.

2. *G. Timothy Noe et al.* Single-shot terahertz time-domain spectroscopy in pulsed high magnetic fields // Optics Express, 2016, V. 24, No 26, P. 30328-30337.

3. M. Glyavin et al. A pulse magnetic field generator for terahertz gyrodevices // Instruments and Experimental Techniques, 2011, V. 54, No. 1, P. 77-80

4. Glyavin M.Y., Luchinin A.G., Golubiatnikov G.Y. Generation of 1.5-kW, 1-THz Coherent Radiation from a Gyrotron with a Pulsed Magnetic Field // Phys. Rev. Lett. 2008. V. 100, No 1. P. 15101.

5. M. Starodubtsev et al. Laboratory investigation of magnetized laser plasmas expansion into the vacuum, ICONO/LAT 2016, Minsk, Belarus

6. Kurbatov, E.P. et al. Comparison of Dimensionless Parameters in Astrophysical MHD Systems and in Laboratory Experiments // Astronomy reports, 2018, V. 62, No. 8, P. 483–491

Single-color pump-probe setup at the NovoFEL facility for measurements of carrier relaxation dynamics in semiconductors

V. D. Kukotenko[1,3], Y. Y. Choporova[1,2], Boris A. Knyazev[1,2], V. V. Gerasimov[1], R. K. Zhukavin[4], K. A. Kovalevsky[4]

[1]Budker Institute of Nuclear Physics, Novosibirsk, Russia, kukotenkovaleria@gmail.com
[2]Novosibirsk State University, Novosibirsk, Russia
[3]Novosibirsk State Technical University, Novosibirsk, Russia
[4]Institute for Physics of Microstructures, Nizhny Novgorod, Russia

The understanding of carrier dynamics in semiconductors is of prime importance for applications but also interesting from a fundamental point of view. As a basic example the speed of semiconductor-based photodetectors is determined by the capture time of free charge carriers. When a semiconductor like Si or Ge is doped with shallow impurities (As, Ga, Sb) the excess electrons or holes behave almost as in a hydrogen atom. However, Bohr radii and energy levels are scaled according to the effective masses and dielectric constants of their host lattice. The perturbation from there ground state and their relaxation back to equilibrium can be directly investigated by the "pump-probe" method.

To selectively excite excitation lines a monochromatic radiation source is needed. For impurities in Ge and Si these lines are in the terahertz frequency range. Temporal information is obtained using short pulses and the time resolution is determined by the pulse duration. The Novosibirsk free-electron laser (NovoFEL) facility is ideally suited for this purpose. NovoFEL generates monochromatic radiation with a tunable wavelength in the range of 6-240 μm. The radiation is emitted in a train of 40 - 100 picosecond pulses with a repetition rate of 5.6 MHz. The spectral width is typically 1%.

The idea of the pump-probe method follows a basic principle: a pump beam with a wavelength equal to a certain energy transition excites a sample. During the passage of the pump pulses, the sample becomes partially transparent as carriers are lifted into an excited state. The relaxation back to the ground state occurs on a characteristic timescale, the lifetime. A second beam, the probe beam, measures the recovery of the transmittance in time as its optical path is changed with respect to the pump pulse.

We use a wire grid polarizer to divide the initial beam into a pump beam and a probing beam. The optical path difference between both pulses can be varied by an optical delay line up to 5 ns. Both beams are then focused onto the sample by off-axis parabolic mirrors (Fig. 1). A sample, e.g. germanium doped with arsenic (Ge:As), is placed in a liquid-He flow cryostat. The temperature of the sample can be varied from 4-200 K. As a detector, we use two Golay cells for the probe and the pump beam. The probe signal is a function of the delay between the two beams and called the pump-probe signal.

The second golay cell in the pump beam acts as a reference signal. To increase the signal-to-noise ratio, the continuous train of the NovoFEL radiation allows us to use a synchronous detection circuit (Lock-in), typically with a frequency of 15 Hz. This frequency is given by the maximum sensitivity of the Golay cells.
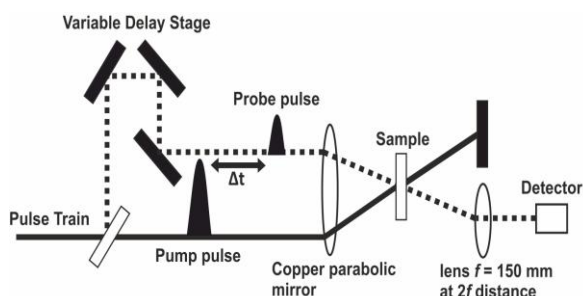
Fig. 1. Optical scheme of the "pump-probe" system at the NovoFEL.

A typical pump probe signal for a Ge:As sample is shown in figure 2. Here, the FEL radiation was tuned to the $1s \rightarrow 2p_0$ transition. The decay of the signal can be fitted by a single exponential function. The exponential time constant τ corresponds to the relaxation time of the energy transition and was found to be $\tau = 1035 \pm 12$ ps. The temperature was kept constant at T = 5 K, the average pump radiation power was 90 mW, the probe radiation power was 2.5 mW, and the wavelength was $\lambda = 131.2$ μm.
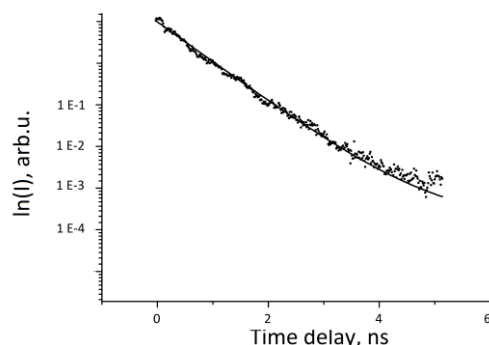
Fig. 2. Pump probe signal for a Ge:As sample at the wavelength was $\lambda = 131.2$ μm.

References

1. *N. Deßmann, S. G. Pavlov.* Time-resolved electronic capture in n-type germanium doped with antimony// Physical review. 2014. V. 89, No. 3. P. 1–8.

2. *R. Kh. Zhukavin, K.A. Kovalevsky.* The times of low-temperature intracenter relaxation of small donors in Ge// Letters to JETP. 2017. V. 789, No. 9. P. 555 – 560.

Generation of terahertz pulses from the island films of topological insulator $Bi_{2-x}Sb_xTe_{3-y}Se_y$

<u>K.A. Kuznetsov</u>[1], G.Kh. Kitaeva[1], P.I. Kuznetsov[2], and G.G. Yakushcheva[2]

[1]M.V. Lomonosov Moscow State University, 119991 Moscow Russia, kirill-spdc@yandex.ru
[2]Kotelnikov IRE RAS (Fryazino branch), 141190 Fryazino, Russia

A great interest to topological matter is stimulated by the study of the THz response to laser radiation. Angle-resolved photoemission spectroscopy (ARPES) indicates the presence of Dirac electrons in many topological insulators (TI) [1] Besides of fundamental aspects, TI's are very perspective objects for practical purposes both THz detectors as THz emission sources.

In this work, we perform a study of the THz emission properties of $Bi_{2-x}Sb_xTe_{3-y}Se_y$ thick films with thickness of hundreds nm and one island film with total thickness about 40 nm grown by MOCVD method on sapphire substrate. Rhombohedral $Bi_{2-x}Sb_xTe_{3-y}Se_y$ films were grown on (0001) Al2O3 substrates with thin (10 nm) ZnTe buffer layer with orientation (111) at atmospheric pressure of hydrogen in horizontal quartz reactor. An example of AFM scan of thin island film surface is shown in Fig. 1.
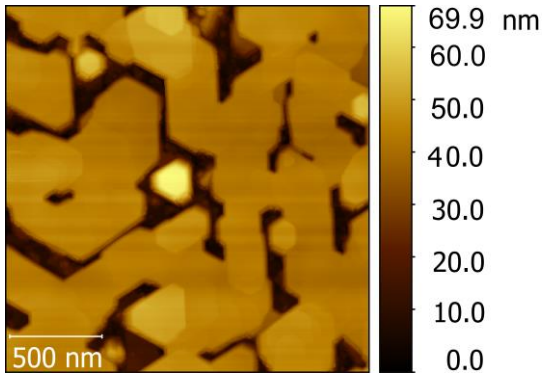

Fig. 1. AFM scan of the TI island film's surface

We use experimental setup for the terahertz emission time-domain spectroscopy (TDS) in the backward geometry. The pump is realized by the Erbium fiber laser in the Q-switched mode locking near a threshold regime at 1.56 μmm wavelength. Er+-laser laser operated in the picosecond mode, generating optical pulses of 2.5 ps duration with the repetition rate of 70 MHz. The pump bam was divided into two unequal parts with a mean power of 100 and 20 mW, respectively. The low-power beam was focused on a photoconductive dipole antenna. The high-power beam, after propagation through the delay line and an optical chopper, was focused by the through a hole in the parabolic mirror onto the TI sample. The angle of incidence was 15°. The sample was in contact with copper electrodes (the distance between them was 0.5 mm) so that external voltage could be applied. The THz radiation generated in the sample in the backward direction was collected by four parabolic mirrors and focused on the commercial THz antenna. The

antenna was oriented to register vertical components of the THz field collinear with the polarization of the pump. Thus, the electric field of THz waves generated in the direction opposite to pumping was measured at different times after the arrival of the pump pulse.

We have shown that the intensity of the THz signal from the island film is 25 times greater than that in "thick" TI samples. In order to demonstrate the amplification effect for THz radiation using an external electric field, we applied a voltage between the electrodes in contact with a surface of the island film. Fig.2 shows the waveforms of THz radiation from an island film with a bias voltage. When the polarity of the bias voltage changed, the THz signal also changed its phase by 180 degrees. Thus, for the first time, the mode of the radiating antenna in a topological insulator was demonstrated.

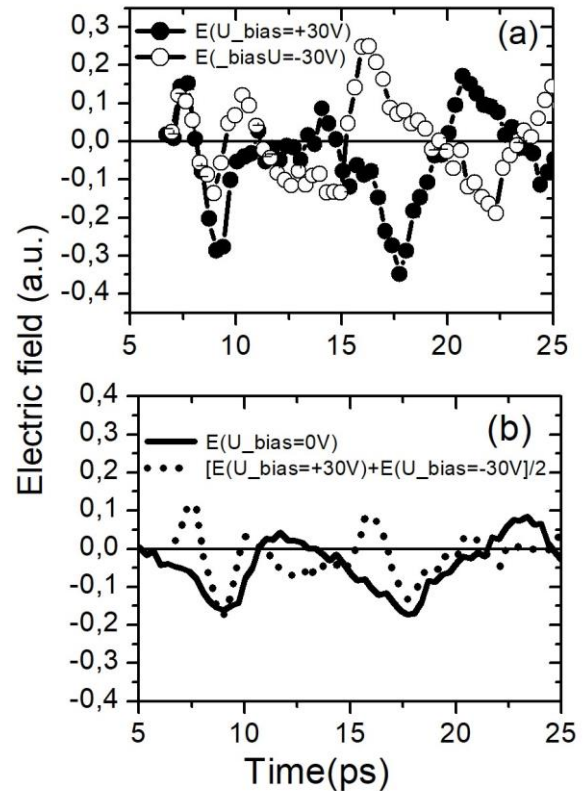**Fig. 2.** Waveforms of the THz pulses

The observed waveforms contain some additional signal, which does not change its polarity with the voltage. To reveal this part we have summarized the signals, observed with +30 V and -30V voltages. Half of this sum is shown in Fig.2b (see the dotted line). The opposite-sign parts of the signals from Fig.2a almost canceled each other, so that one could expect

to observe the residual constant part of the same shape as the zero-voltage signal. However, this is not true. For comparison, we repeat the zero-voltage signal together with this residual signal. One can see that the antenna pulses contain additional parts corresponding to higher modulation frequencies. This fact is illustrated in Fig.3 where the spectra of the both waveforms are shown.
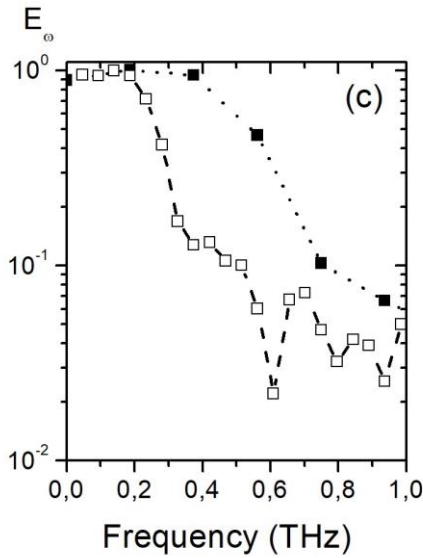
Fig. 3 Spectrum of zero-voltage signal (hollow squares) and spectrum of half-sum of signals at external bias (filled squares).

The spectrum of the residual part of the antenna signal is about two-times broader than the spectra of all the other signals, i.e. the zero-voltage signal, and the polarity-sensitive parts of +30 V and -30V voltages signals. The peak frequency corresponds to times that are of order or even less than the pump pulse duration. It means that some carrier relaxation effects proceed at considerably shorter relaxation times, than it is usually assumed to describe the THz emission of free TI samples. We believe that this effect arises from the relaxation of fast non-equilibrium charge carriers accelerated by an external field. Probably electrons are captured by the traps that are p-type impurities with energy above the bulk valence band maximum in the energy of 3-6 meV or other defects.

References

1. *M. Z. Hasan and C. L. Kan.* Colloquium: Topological insulators // Rev. Mod. Phys. 2010, V.82,P. 3045.

Aligned planar-wire zero-index metamaterial for terahertz frequency range

E.A. Litvinov[1], P. S. Demchenko[1], E.B. Sheklanova[2], M.K. Khodzitsky[1]

[1]Terahertz Biomedicine Laboratory, Saint-Petersburg, Russia, thzbiomedicine@corp.ifmo.ru
[2] International Laboratory "Nonlinear optical molecular crystals and microlasers", Saint-Petersburg, Russia

Introduction

Demonstrations of specific class of materials with extremely small (near zero) values of permittivity have attracted attention of scientific community[1]. These unique materials have the refractive index equal to zero what causes almost constant spatial distribution of the electric field of the propagating wave inside these media[2].

Considering its extreme properties, ENZ-material can also be used as delay line that brings no phase delay in propagating wave[3], as ideal coupler between waveguides of the same diameter and can find effective application in cloaking[4]. It should be mentioned that ENZ-, MNZ- ("mu near zero") and LH- ('left-handed') materials can be designed using transformation optics approximation[5–7].

ENZ or MNZ coating may be used to radically enhance transmission through subwavelength aperture in planar ideally opaque screen which allow to overcome the diffraction limit. In general, isolated subwavelength aperture can't provide enough transfer of energy, but with ENZ coating the transfer increases by several orders of magnitude[8].

This work is dedicated to zero-index (ZI) terahertz metamaterial designed with one-layer aligned planar aluminum wires on dielectric PET substrate and acting like epsilon-near-zero (ENZ) medium.

Metal stripes on dielectric substrate can be easily manufactured. The idea is that metal stripes may have permittivity described by Drude model in terahertz frequency range, what gives the opportunity to design ENZ-material.

Numerical simulation of the structure

To prove that such structure can act like ENZ-material, number of numerical simulations was done with the periodic boundary conditions. Simulations were done also in two steps: the first is for the unit cell and the second is for the one-layered structure.
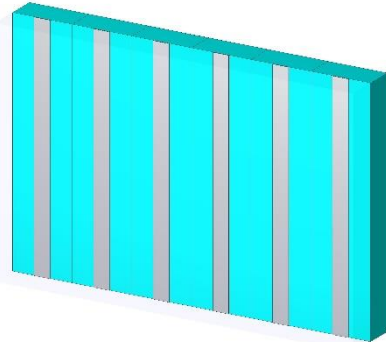
Fig. 1. The investigated structure: dielectric PET (Polyethylene terephthalate) substrate and parallel aluminum stripes.

(a)

(b)
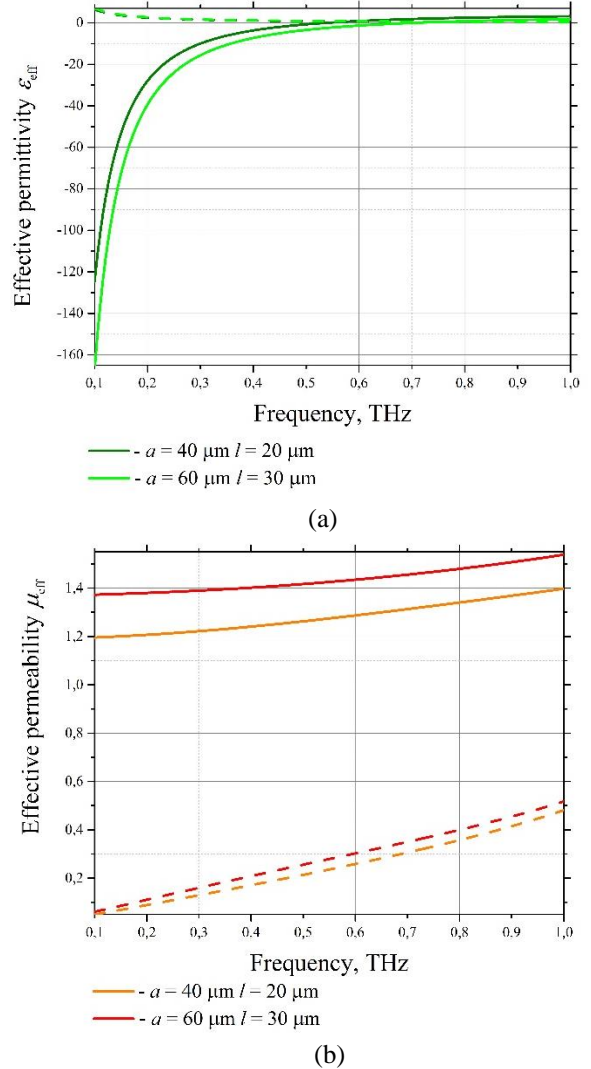
Fig. 1. Results of numerical simulations of the striped metamaterial (a is the lattice constant, l is the width of the stripe). 'Electric' plasma frequency for $l = 20$ μm is 0,641 THz and for $l = 30$ μm is 0,562 THz.

Experimental verification

The material was made by laser ablation method using LaserGraver LG2500 SP47. Two samples were used for the experiment: ones with $l = 20$ μm $a = 40$ μm and $l = 30$ μm $a = 60$ μm. Examined samples were measured using time-domain terahertz spectroscopy in 0,1-1 THz frequency range in transmission mode.
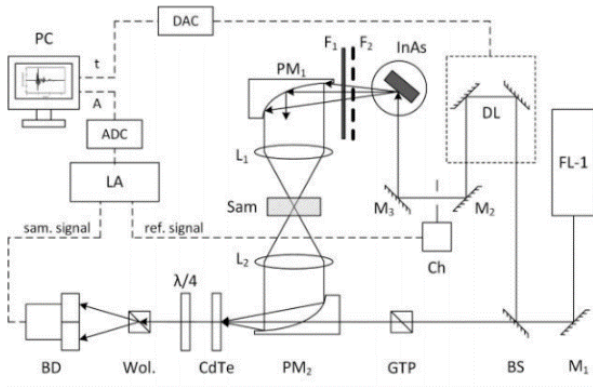
Figure. 1. Experimental THz TDS setup[9] in transmission mode (FL-1 – femtosecond laser based on potassium-yttrium tungstate crystal activated with ytterbium (Yb: KYW), generating femtosecond pulses; F1,2 – teflon filters for IR wavelength range cutting off, BS – beamsplitter, DL – optical delay line, M1,2,3 – mirrors, Sam – investigated sample, Wol. – Wollaston prism, CdTe – electro-optical cadmium-telluric crystal, BD – balanced detector, LA – lock-in amplifier, PC – personal computer, GTP – Glan-Taylor prism, PM1,2 – parabolic mirrors, Ch – chopper, DAC – digital to analog converter, ADC – analog to digital converter)

The experiment showed that samples have the dispersion of refractive index according to Drude model (Figure 8). In a little area near plasma frequencies samples behave 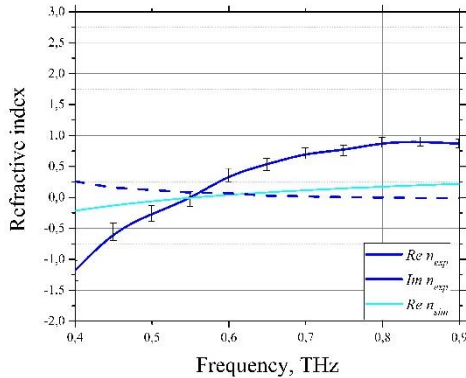as ENZ-material. It should be mentioned that below plasma frequencies medium shows left-handed properties in materials previously designed[10,11].
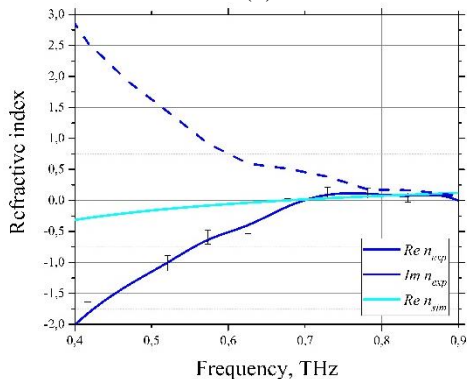

Figure 2. Experimental (blue) and calculated (cyan) effective permittivity and permeability of two striped metamaterial samples. (a) is the data on s ample with $l = 20$ μm $a = 40$ μm and (b) is the data on sample with $l = 30$ μm $a = 60$ μm. Plasma frequencies are approximately 0,556 THz for (a) and 0,648 THz for (b).

Conclusion

This paper showed the possibility of designing ZI-materials for terahertz frequency range using one-layered copper wire or aluminum stripe lattices. Copper-wired medium can be manufactured using electrochemical etching or electron-beam lithography. Aluminum-striped material was made from metallized PET substrate using laser ablation. ENZ properties of metal-striped materials were showed using numerical simulation and verified experimentally. Two striped-material samples were about to have effective plasma frequency in terahertz frequency range and showed left-handed properties below the plasma frequency.

References

[1] Engheta, N. and Liberal, I., "The rise of near-zero technologies," Science **358**(6370), 1540–1541 (2017).

[2] Ziolkowski, R. W., "Propagation in and scattering from a matched metamaterial having a zero index of refraction," Physical Review E **70**(4) (2004).

[3] Enoch, S., Tayeb, G., Sabouroux, P., Guérin, N. and Vincent, P., "A Metamaterial for Directive Emission," Physical Review Letters **89**(21) (2002).

[4] Alu, A., Engheta, N., Erentok, A. and Ziolkowski, R., "Single-Negative, Double-Negative, and Low-index Metamaterials and their Electromagnetic Applications," IEEE Antennas and Propagation Magazine **49**(1), 23–36 (2007).

[5] Islam, S. S., Faruque, M. R. I. and Islam, M. T., "An Object-Independent ENZ Metamaterial-Based Wideband Electromagnetic Cloak," Scientific Reports **6**(1) (2016).

[6] Javani, M. H. and Stockman, M. I., "Real and Imaginary Properties of Epsilon-Near-Zero Materials," Physical Review Letters **117**(10) (2016).

[7] Kyoung, J., Park, D. J., Byun, S. J., Lee, J., Choi, S. B. and Park, S., "Epsilon-Near-Zero meta-lens for high resolution wide-field imaging," Optics Express **22**(26), 31875 (2014).

[8] Shi, K. and Lu, Z., "Field-effect optical modulation based on epsilon-near-zero conductive oxide," Optics Communications **370**, 22–28 (2016).

[9] Bespalov, V. G., Gorodetskiĭ, A. A., Denisyuk, I. Y., Kozlov, S. A., Krylov, V. N., Lukomskiĭ, G. V., Petrov, N. V. and Putilin, S. é., "Methods of generating superbroadband terahertz pulses with femtosecond lasers," Journal of Optical Technology **75**(10), 636 (2008).

[10] Khodzitsky, M. K., Tarapov, S. I., Belozorov, D. P., Pogorily, A. M., Tovstolytkin, A. I., Belous, A. G. and Solopan, S. A., "Negative permittivity and left-handed behavior of doped manganites in millimeter waveband," Applied Physics Letters **97**(13), 131912 (2010).

[11] Khodzitsky, M. K., Kharchenko, A. A., Strashevskyi, A. V. and Tarapov, S. I., "Left-Handed Properties of Metal-Ferrite Composites Placed into Waveguide in Millimetric Wave Range," Telecommunications and Radio Engineering **68**(7), 561–566 (2009).

Angle-Susceptible Sensing Metasurface in Terahertz Regime

N. A. Nikolaev[1, 2], S. A. Kuznetsov[3, 4], M. Beruete[5]

[1]Institute of Automation and Electrometry SB RAS, Novosibirsk, Russia, Nazar@iae.nsk.su
[2]Institute of Laser Physics SB RAS, Novosibirsk, Russia
[3]Rzhanov Institute of Semiconductor Physics SB RAS, Novosibirsk Branch "TDIAM", Novosibirsk, Russia
[4]Novosibirsk State University, Novosibirsk, Russia
[5]Public University of Navarra, Pamplona, Spain

Introduction

Nowadays thin-film coatings and structures are widely used in advanced industrial and scientific applications that makes the tasks of thin-film sensing highly demanded in practice. Last decade, stimulated by progress in terahertz (THz) instrumentation, a keen interest has been attracted to the THz spectral range to develop its potential for detecting and measuring properties of thin films. The THz radiation can be an alternative to visible and IR waves when examining optically opaque coatings. Meanwhile, due to a relatively large wavelength λ, the conventional spectroscopic methods (TDS-, FDS-, FTIR-, BWO-based) are ill-suited for direct characterization of films with the thickness d of about 2–4 orders of magnitude smaller than λ. This problem can be solved with metamaterials, in particular, with plasmonic metasurfaces (PMSs) [1–5]. The plasmonic resonance exhibits a high sensitivity of its spectral response to the dielectric environment due to a strong field localization what makes possible measuring of analyte layers satisfying $d << \lambda$ condition.

The traditional approach of THz thin-film sensing with PMSs is based on detecting a frequency shift of the resonance when the analyte is deposited onto the PMS. In this work, we present the idea to substitute THz spectral measurements for tracking the PMS response at a fixed wavelength upon changing the incidence angle θ of the exciting THz beam. This concept works well for the PMS with a narrowband resonance sensitive to θ.

The results of the numerical investigations and experimental study of such PMS designed as a single-layer array of hexagon-shaped annular slots (Fig. 1) with angle-susceptible resonant transmission near 0.85 THz are presented.

Metasurface design

Originally, the proposed PMS was intended for band-pass filtering applications in experiments on studying sub-THz emission from hot dense plasma during relativistic electron beam-plasma interaction [6, 7]. The listed PMS dimensions provide a resonant pass band centered at 0.5 THz with the relative bandwidth of 63%. Later, when inspecting the angular performance of the PMS of this kind, a higher-frequency "spurious" narrow-band resonance susceptible to the angle of incidence was revealed in the vicinity of 0.8–0.9 THz. A detailed study of this resonance for the purpose of its applicability to thin-film sensing became the essence of the current work.

To pattern the PMS, we employed a contact photolithography technique [8, 9] which was specifically adapted to flexible solid film substrates, such as PP, whose industrial production does not allow obtaining a liquid material suitable for posterior film deposition via spin coating.
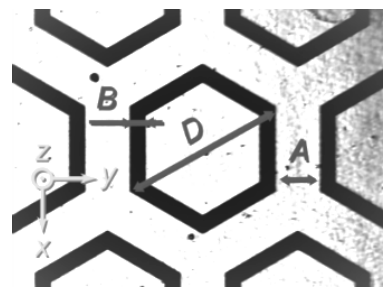
Fig. 1. Reflection-mode microphotograph of the fabricated plasmonic metasurface. The metallic area is light-colored. The slots are patterned in a 0.35 μm thick aluminum layer deposited on a 15 μm thick polypropylene film. D = 220 μm, B = 20 μm, A = 20 μm. The coordinate system xyz is introduced to show the structure orientation relative to the incident wave vector $k = (k \cdot sin\,\theta \cdot cos\,\phi,\ k \cdot sin\,\theta \cdot sin\,\phi,\ k \cdot cos\,\theta)$.

Experimental setup

The transmission spectra of the designed metasurface were measured on a custom-made THz time-domain spectrometer (TDS) described in Refs. [10, 11]. The PMS prototype under study was mounted on a manually controlled rotary stage capable of tilting the prototype both in TE and TM planes. The measurements were carried out by varying the incidence angle θ of the probing THz beam within 0°–55° with 5° incremental step. The THz-TDS signals were acquired with the time resolution of 125 fs in the range of 100 ps. This corresponds to the resolution of ~10 GHz in the frequency spectrum. The transmission was calculated as the ratio of the Fourier-transform spectra for the time-domain signals registered with and without the PMS prototype. The resulting experimental spectra were averaged over four independent measurements.

Results

Fig. 2 illustrates the typical spectral behavior of the angle-susceptible PMS resonance for different thicknesses d of the analyte overlayer plotted at a fixed angle of incidence θ. A photoresistive material was used as the analyte, whose dielectric permittivity $\varepsilon = 2.7 - j \cdot 0.25$ was retrieved from direct transmission measurements of a 100 μm thick liquid cell.

To elucidate the idea of replacing THz spectral measurements by tracking the PMS response at a fixed λ upon changing the incidence angle θ, the PMS transmittance as a function of θ is plotted in Fig. 3. The latter corresponds to the frequency of 830 GHz chosen as an example.
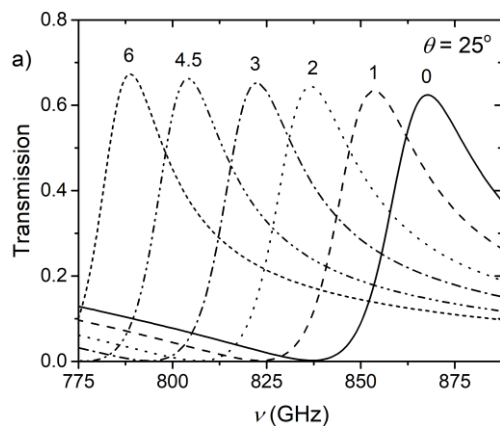
Fig. 2. Transmission spectra for the PMS covered with the analyte of different thicknesses d simulated at $\theta=25°$.
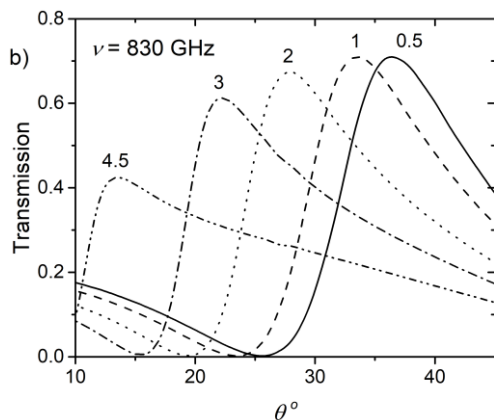
Fig. 3. PMS transmission at 830 GHz as the function of the incident angle θ modelled for different thicknesses d of the analyte overlayer. The numbers indicate the values of d in micrometers.

The presented data remarkably demonstrate the expected effect of shifting the angular peak due to thickening the analyte. Note, the resonance peak amplitude decreases and its bandwidth increases when the analyte thickness d changes from 0.5 to 4.5 μm. This means that the method sensitivity degrades for the thicknesses larger than 4.5 μm. Nevertheless, the peak remains almost stable in amplitude for the thicknesses $d < 1$ μm and the angles of both maximum and minimum transmission can be used to evaluate the analyte thickness. Thus, the proposed approach is estimated to be promising for THz sensing of sub-μm-thick analyte layers, thereby capable of detecting the level of $d/\lambda \sim 10^{-3}$ at least.

References

1. M. Tonouchi Cutting-edge terahertz technology // *Nature photonics*. 2007. V. 1, No. 2. P. 97-105.

2. M. Perenzoni and D. J. Paul, Eds. Physics and applications of Terahertz radiation, Dordrecht, Netherlands: Springer, 2014.

3. D. M. Mittleman Perspective: Terahertz science and technology // *J. Appl. Phys.* 2017. V. 122, No. 23, P. 230901.

4. F. F. Sizov Infrared and terahertz in biomedicine // *Semiconductor Physics, Quantum Electronics & Optoelectronics.* 2017. V. 20, No. 3. P. 273-283.

5. H. J. Song and T. Nagatsuma, Eds. Handbook of terahertz technologies: devices and applications, Boca Raton, U.S.: CRC press, 2015.

6. A. V. Arzhannikov, A. V. Burdakov, V. S. Burmasov, et al. Observation of spectral composition and polarization of sub-terahertz emission from dense plasma during relativistic electron beam-plasma interaction // *Phys. Plasmas.* 2014. V. 21, No. 8. P. 082106.

7. A. V. Burdakov, A. V. Arzhannikov, V. S. Burmasov et al. Microwave generation during 100 keV electron beam relaxation in GOL-3 // *Fus. Sci. Technol.* 2013. V. 63, No. 1T. P. 286-288.

8. M. Navarro-Cía, S. A. Kuznetsov, M. Aznabet et al. Route for bulk millimeter wave and terahertz metamaterial design // *IEEE J. Quantum Electron.* 2011. V. 47, No. 3. P. 375-385.

9. S. A. Kuznetsov, A. V. Arzhannikov, V. V. Kubarev et al. Development and characterization of quasi-optical mesh filters and metastructures for subterahertz and terahertz applications // *Key Eng. Mat.* 2010. V. 437, P. 276-280.

10. Mamrashev A. A., Maximov L. V., Nikolaev N. A., Chapovsky P. L. Detection of nuclear spin isomers of water molecules by terahertz time-domain spectroscopy // *IEEE transactions on terahertz science and technology.* 2018. V. 8, No. 1. P. 13–18.

11. Antsygin V.D., Mamrashev A.A., Nikolaev N.A., Potaturkin O.I., Bekker T.B., Solntsev V.P. Optical properties of borate crystals in terahertz region // *Optics Communications.* 2013. V. 309. P. 333–337.

Far IR continuum absorption of $H_2^{16}O$ and $H_2^{18}O$

T.A. Odintsova[1], M.Yu Tretyakov[1], A.O. Zibarova[1,2], O. Pirali[3], P. Roy[3] and A. Campargue[4]

[1]Institute of Applied Physics, Russian Academy of Sciences, Nizhniy Novgorod, Russia, odintsova@ipfran.ru
[2]Lobachevsky State University of Nizhny Novgorod, Nizhny Novgorod, Russia
[3]SOLEIL Synchrotron, L'Orme des Merisiers, Saint-Aubin 91192, Gif-Sur-Yvette, France
[4]Univ. Grenoble Alpes, CNRS, LIPhy, 38000 Grenoble, France

Water vapor is the main greenhouses gas and it is responsible for about 70% of solar radiation absorption by the Earth atmosphere. Water vapor absorption consists of resonance absorption (sum of water lines) and continuum absorption (smoothly varying with frequency). Even though continuum is several orders of magnitude weaker than absorption at the center of absorption lines, its integrated contribution to total atmospheric absorption is significant and exceeds contribution of other greenhouse gases, such as CO_2 and CH_4. Thus, appropriate calculation of radiation balance, modeling of global climate changes and atmosphere remote sensing require accounting of the water vapor continuum.

Nowadays the semi-empirical MTCKD model [1] is the standard model implemented in radiative transfer codes to describe the water absorption continuum. This model is a far wing model constrained on experimental data obtained in the IR frequency range mainly at room or elevated temperatures. Extrapolation of this model to other frequency ranges (including terahertz region) and atmospheric temperatures are hazardous and might deviate from new experimental data [2].

Appropriate description of water vapor continuum absorption requires development of physically based model. In spite of long history of theoretical and experimental investigation of the continuum, it remains poorly characterized and understood. Its nature is not fully settled yet. Nevertheless, it was established, that the continuum originates from nonideality of water vapor and its magnitude is quadratic function of pressure (self continuum). There are several possible sources of continuum: intermediate wings of resonance lines, bound and quasi-bound water dimer absorption and collision induced absorption.

Our investigation of the continuum absorption in the frequency range of water molecule rotational band is motivated by: (i) filling the spectral gap on the continuum data, and (ii) determination of water dimer and intermediate wings contributions to the continuum.

The weakness of the continuum makes to use a spectrometer with a high sensitivity and a high stability. In the current study the continuum was measured using high resolution Fourier transform spectrometer IFS-125HR equipped with multipass gas absorption cell with total pathlength of 151 m, that allowed to distinguish weak continuum absorption even at few mbar of water vapor pressure. The measurements were performed at the AILES beamline of SOLEIL synchrotron. The high power and high stability of the synchrotron radiation allows increasing sensitivity of the spectrometer up to 15 times in comparison with standard laboratory sources. To cover the frequency range of the rotational band, the coherent (15-35 cm⁻¹) and standard (50-500 cm⁻¹) radiation modes of the synchrotron were used. In order to refine the magnitude and clarify the physical origin of the continuum, spectra of the two major water isotopologues, $H_2^{16}O$ and $H_2^{18}O$, were considered. Recordings at several water vapor pressures were used to check the expected quadratic pressure dependence of the continuum.

The continuum was obtained by difference between experimental absorption α_{EXP} and modeled resonance absorption α_{WML}:

$$\alpha_C = \alpha_{EXP} - \alpha_{WML}.$$

Resonance absorption was modeled as sum of all significant lines of 7 most abundant water isotopologues:

$$\alpha_{WML}(\nu) = \sum_{j=1}^{7} \sum_{i} S_i^j \cdot \Phi(\nu),$$

where $\Phi(\nu)$ is Van Vleck - Weisskopf profile with commonly accepted wings cut off at 25 cm⁻¹ and line shape parameters (including line strength S_i, center frequency and collisional broadening coefficient) from HITRAN 2016 database [3].

The continuum cross-section was determined as

$$C(\nu,T) = \frac{\alpha_C(\nu) \cdot k_B T}{P^2}$$

where T is temperature, k_B - Boltzmann constant and P - water vapor pressure.

Water vapor absorption spectra in the frequency range of 15-35 cm⁻¹ were recorded at two pressures (11 and 16 mbar of natural water and 13 and 16 mbar of water sample enriched with O^{18}). The coincidence of the continuum cross-sections corresponding to two pressures is a validation of the pressure squared dependence. Fig.1. compares our results to literature measurements [4-10] in the range up to 60 cm⁻¹ together with a calculated spectral function of $(H_2^{16}O)_2$ dimer [11]. The experimental data show a good agreement with the frequency dependence of the function. The $H_2^{18}O$ continuum shows a similar spectrum in this range (Fig.2.). These facts confirm the dominating contribution of water dimer absorption to the observed continuum. It should be mentioned, that the MTCKD model does not account satisfactorily of the observed frequency dependence in this region (see Fig. 1).

In the 50-500 cm⁻¹ range, $H_2^{16}O$ and $H_2^{18}O$ continuum spectra were recorded for a number of pressures between 2 and 6 mbar. The very good quadratic pressure dependence of the measured continuum was obtained. The continuum absorption corresponding to $H_2^{16}O$ and $H_2^{18}O$ molecules are similar in shape and

magnitude. Non-smooth frequency dependence of the $H_2^{16}O$ and $H_2^{18}O$ continua is observed between retrievals performed in nearby micro-windows (Fig.3). Inadequate modern line shape modeling in the range of intermediate wing (detuning of 5-10 cm^{-1} from line center) is believed to be responsible of the obtained fluctuations. We believe that investigation of isotopic dependence of the continuum could help to determine contribution of intermediate wings of resonance lines.
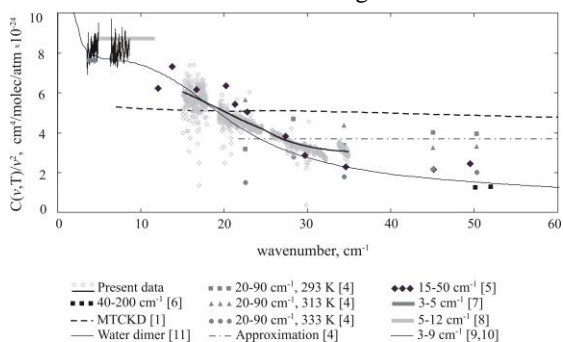
Fig. 1. Calculated water dimer spectral function [11], water vapor ($H_2^{16}O$) self-continuum cross-section normalized by frequency squared: obtained data, results of previous measurements.
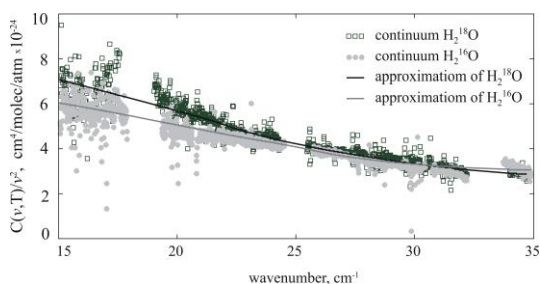
Fig. 2. Water vapor ($H_2^{16}O$ and $H_2^{18}O$) self-continuum cross-section normalized by frequency squared.

The new data on $H_2^{16}O$ continuum are in a good agreement with results of our previous measurements in the range of 40-200 cm^{-1} [6] and with results obtained by Burch in the range of 350-800 cm^{-1} [5]. New data filled the 200-350 cm^{-1} "gap" where the continuum was not measured before (Fig.3). The data confirmed that the widely used in atmospheric applications MT-CKD model [1] overestimates the continuum amplitude by about 30% in the whole range of the rotational band of H_2O (Fig.3).
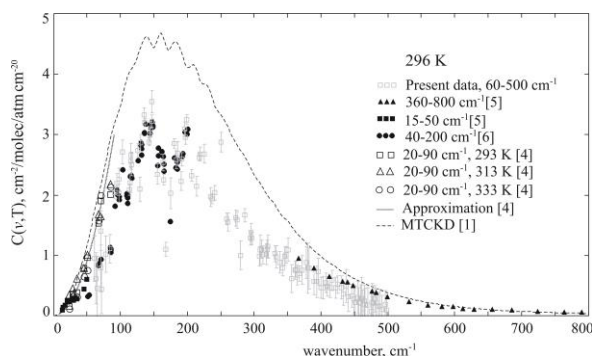
Fig. 3. Comparison of our data on the continuum with results of previous experimental studies [4-6] and MTCKD model [1].

References

1. *Mlawer E. J., et al.* Development and recent evaluation of the MT_CKD model of con-tinuum absorption // Philos. Trans. R. Soc. A. 2012. No. 370. P. 2520 – 56.

2. *Campargue A., et al.* Accurate laboratory determination of the near infrared water vapor self-continuum. A test of the MT_CKD model. J. Geophys. Res. Atmos. 2016. No. 13. P. 180 - 203.

3. *Gordon I. E., et al.* The HITRAN2016 Molecular Spectroscopic Database. J. Quant. Spectrosc. Rad. Trans. 2017. No. 203. P. 3–69.

4. *Podobedov V. B.,et al.* New measurements of the water vapor continuum in the region from 0.3 to 2.7 THz. J. Quant. Spectrosc. Rad. Trans. 2008. No. 109. P. 458 – 67.

5. *Burch D.E.* In: Continuum absorption by H2O. 1982. Report No. AFGL-TR-81-0300

6. *Odintsova T. A. et al.* Water Vapor Continuum in the Range of Rotational Spectrum of H2O Molecule: New Experimental Data and Their Comparative Analysis. J. Quant. Spectrosc. Rad. Trans. 2017. No.187. P. 116–123

7. *Koshelev M. A., et al.* Millimeter Wave Continuum Absorption in Moist Nitrogen at Temperatures 261–328 K. J. Quant. Spectrosc. Rad. Trans. 2011. V. 112. No. 270. P. 4 – 12.

8. *Kuhn T., et al.* Water vapor continuum: absorption measurements at 350 GHz and model calculations. J. Quant. Spectrosc. Rad. Trans. 2002. No. 74. P. 545 – 62.

9. *Tretyakov M. Yu., et al.* Water Dimer Rotationally Resolved Millimeter-Wave Spectrum Observation at Room Temperature. Phys. Rev. Lett. 2013. No. 110. P. 093001

10. *Serov E. A., et al.* Rotationally Resolved Water Dimer Spectra in Atmospheric Air and Pure Water Vapour in the 188–258 GHz Range. Phys. Chem. Chem. Phys. 2014. V. 16. No. 47. P. 26221 – 33.

11. *Scribano Y., Leforestier C.* Contribution of water dimer absorption to the millimeter and far infrared atmospheric water continuum. J. Chem. Phys. 2007. No. 126. P. 234301.

Oxide nonlinear crystals: optical properties and phase-matching for terahertz wave generation

O. I. Potaturkin[1], V. D. Antsygin[1], A. A. Mamrashev[1], N. A. Nikolaev[1],
Yu. M. Andreev[2,3], G. V. Lanskii[2,3], V. A. Svetlichnyi[3], K. A. Kokh[4]

[1]Institute of Automation and Electrometry SB RAS, Novosibirsk, Russia, potaturkin@iae.nsk.su
[2]Institute of Monitoring of Climatic and Ecological Systems SB RAS, Tomsk, Russia
[3]Siberian Physical Technical Institute of Tomsk State University, Tomsk, Russia
[4]Institute of Geology and Mineralogy SB RAS, Novosibirsk, 630090, Russia

Introduction

Oxide nonlinear crystals such as beta-barium borate (β-BaB$_2$O$_4$ or β-BBO), potassium titanyl phosphate (KTiOPO$_4$ or KTP), potassium titanyl arsenate (KTiOAsO$_4$ or KTA) are widely used for efficient harmonic, difference frequency and optical parametric generation/oscillation in the visible and near-infrared ranges [1]. The crystals have wide transparency range stretching from 0.19 μm for β-BBO, 0.35 μm for KTP and KTA to near-IR or even mid-IR range. They also have moderate nonlinear coefficients and high optical damage threshold.

Recently these crystals attracted attention as prospective materials for terahertz applications. Several studies were devoted to measuring their optical properties (refractive index and absorption coefficient) in the terahertz domain [2–5]. Different schemes for IR-to-THz and THz-to-THz conversion were investigated [6–9]. Besides nonlinear crystals another attractive materials such as metals and semi-metals were considered for efficient conversion of near-IR femtosecond pulses to terahertz radiation on their surface [10].

In this study we measure terahertz optical properties and discuss possibilities of applying oxide nonlinear crystals, metals and semi-metals for terahertz wave generation.

Selected results

Absorption coefficient and refractive index dispersions in the THz range for all axes of nonlinear oxide crystals were measured at the room (RT), liquid nitrogen (LN), and liquid helium (LH) temperatures within the range of 0.2-2.5 THz using custom-made terahertz time-domain spectrometer (THz-TDS) described elsewhere [2].

Absorption coefficient and refractive index of β-BBO crystals for ordinary and extraordinary waves were measured at RT and LN temperatures of 293 K and 81 K, respectively. Sellmeier equations for both o- and e-waves were formulated. Dispersion equations for at RT valid in the range of 187–10000 μm:

$$n_o^2 = 2.040 + \frac{0.816\,\lambda^2}{\lambda^2 - 12815}, \quad n_e^2 = 2.478 + \frac{0.160\,\lambda^2}{\lambda^2 - 15598} \quad (1)$$

Dispersion equations at LN temperature valid in the range of 182–3530 μm for o- and 144–2727 μm for e-wave:

$$n_o^2 = 4.612 + \frac{3.117\,\lambda^2}{\lambda^2 - 16175}, \quad n_e^2 = 5.970 + \frac{0.800\,\lambda^2}{\lambda^2 - 16659} \quad (2)$$

Using resulting dispersion curves we were able to find phase-matching (PM) for down-conversion or difference frequency generation of near-IR radiation into the THz range was found possible by o–o→e, e–e→o and original e–e→e types (Fig. 1) of three-wave interactions.

It was found that despite the significant decrease in the absorption coefficient at LN temperature, refractive index components and birefringence did note change a lot keeping PM conditions favorable for efficient down-conversion into the THz range.
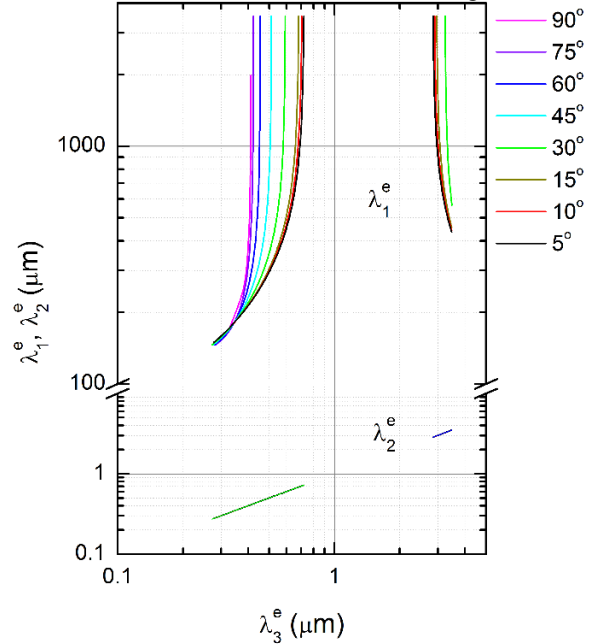
Fig. 1. Phase-matching curves for type I (e–e→e) three-wave interactions in β-BBO at RT. θ angles are shown in the figure inset

In a similar manner, terahertz optical properties of KTP crystals were measured at three temperatures. The refractive index for all three optical axes of KTP crystal was approximated in the form of Sellmeier equations. Here is a set of equations for LH temperature of 5.3 K where λ is in μm:

$$n_x^2 = 8.67715 + \frac{1.34263\,\lambda^2}{\lambda^2 - 11458}$$

$$n_y^2 = 8.86222 + \frac{1.22979\,\lambda^2}{\lambda^2 - 12045}$$

$$n_z^2 = 13.18625 + \frac{0.86157\,\lambda^2}{\lambda^2 - 21447} \quad (3)$$

Using dispersion equations for the visible, infrared and terahertz ranges we obtained comprehensive results for phase-matched difference frequency generation in KTP crystals at different temperatures and different wavelengths presented in the Fig. 2.
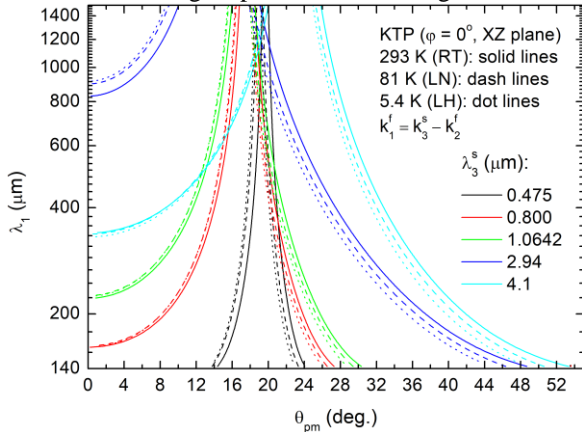
Fig. 2. Phase-matching curves for $s - f \rightarrow f$ type of difference frequency generation in the *XZ* principle plane of KTP crystal at RT (bold lines), LN (dash lines) and LH (dot lines) temperatures for different λ from 0.475 to 4.1 μm

KTA refractive index measured at RT was approximated in the form of the following Sellmeier equations in the range from 132 μm (n_x), 155 μm (n_y), 313 μm (n_z) to 3200 μm:

$$n_x^2 = 9.70796 + \frac{1.24017\,\lambda^2}{\lambda^2 - 12935}$$

$$n_y^2 = 9.62652 + \frac{1.44084\,\lambda^2}{\lambda^2 - 17674} \qquad (4)$$

$$n_z^2 = 16.6706 + \frac{0.12511\,\lambda^2}{\lambda^2 - 85811}$$

Analogous phase-matching curves for DFG of Nd:YAG laser in KTA crystals is shown in the Fig. 3.
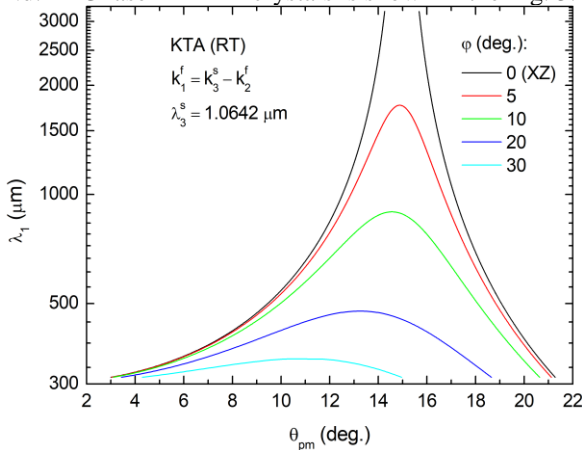
Fig. 3. Phase-matching curves for $s - f \rightarrow f$ type of difference frequency generation in KTP crystal at RT for the wavelength of Nd:YAG lasers

A common feature of all three abovementioned crystals was that cooling them down did not significantly affect phase-matching conditions. At the same time their absorption coefficient lowered drastically making cooled crystals more effective for terahertz wave generation.

The crystals were tested as narrowband THz radiation sources for a homemade spectrometer described elsewhere [11] having a long (>1 km) measuring path which consists of a transceiver adopted from a lidar complex [12].

We also studied terahertz generation on the surface of metals (Ti, Ni, Au, Cu) and their alloys ($Ti_{50.5}Ni_{49.5}$) pumped by femtosecond Ti:Sapphire laser. The power of generated radiation was measured using Golay cell. Fig. 4 shows that the output signal is linearly depends on the pump pulse energy. We also found that the efficiency of optical-to-terahertz conversion is proportional to the material conductivity.
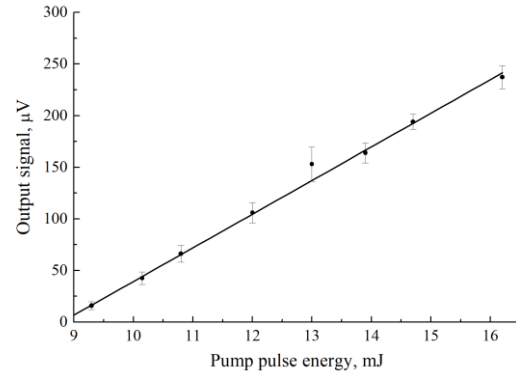
Fig. 4. Dependence of Golay cell signal proportional to the terahertz power generated on the surface of $Ti_{50.5}Ni_{49.5}$ alloy on the pump pulse energy

References

1. *Nikogosyan D.* Nonlinear optical crystals: a complete survey. New York: Springer, 2005.

2. *Antsygin V.D. et al.* Optical properties of borate crystals in terahertz region // Optics Communications. 2013. Vol. 309. P. 333–337.

3. *Antsygin V.D. et al.* Terahertz optical properties of potassium titanyl phosphate crystals // Optics Express. 2014. Vol. 22, Is. 21. P. 25436.

4. *Andreev Y.M. et al.* Observation of a different birefringence order at optical and THz frequencies in LBO crystal // Optical Materials. 2017. Vol. 66. P. 94–97.

5. *Nikolaev N.A. et al.* Terahertz optical properties of LBO crystal upon cooling to liquid nitrogen temperature // Quantum Electronics. 2018. Vol. 48, Is. 1. P. 19–21.

6. *Huang J.-G. et al.* Phase matching in RT KTP crystal for down-conversion into the THz range // Laser Phys. Lett. 2018. Vol. 15, Is. 7. P. 075401.

7. *Mamrashev A.A. et al.* Optical Properties of KTP Crystals and Their Potential for Terahertz Generation // Crystals. 2018. Vol. 8, Is. 8. P. 310.

8. *Nikolaev N.A. et al.* Optical properties of β-BBO and potential for THz applications // Journal of Physics: Conference Series. 2018. Vol. 951. P. 012003.

9. *Nikolaev N.A. et al.* Temperature dependence of terahertz optical properties of LBO and perspectives of applications in down-converters // Journal of Physics: Conference Series. 2018. Vol. 951. P. 012005.

10. *Mironov V.A., Oladyshkin I.V., Fadeev D.A.* Optical-to-THz radiation conversion on a semi-metal surface // Quantum Electronics. 2016. Vol. 46, Is. 8. P. 753–758

11. *Huang J.-G. et al.* Remote imaging by nanosecond terahertz spectrometer with standoff detector // Russian Physics Journal. 2018. Vol. 60, Is. 9. P 1638-1643.

12. *Andreev Yu. M., Geiko P.P., Sherstov I.V.* Development and testing of the lidar gas analyzing complex // Proc. SPIE. 1999. Vol. 3983, P. 386-394.

Terahertz induced optical second harmonic generation from silicon surface

S.B. Bodrov[1,2], A.I. Korytin[1], Yu.A. Sergeev[1], A.N. Stepanov[1]

[1]Institute of Applied Physics of the Russian Academy of Sciences, Nizhny Novgorod, Russia, yas@ufp.appl.sci-nnov.ru
[2]University of Nizhny Novgorod, Nizhny Novgorod, Russia

Second harmonic generation (SHG) of optical radiation from surface is one effective technique for surface diagnostics [1]. It is well known, that in bulk media with inversion center the second harmonic generation is prohibited in the dipole approximation. However, the surface breaks the symmetry and allows SHG. In this regard, the second harmonic (SH) signal is extremely sensitive to the state of the surface. The SHG technique allows to measure inhomogeneities of the surface, dynamics of fast processes, such as fast melting under the action of femtosecond laser pulses, contains information about the surface states of the material. An application of the external field on the surface can significantly change the second harmonic signal [2,3].

In this work, we investigated influence of intense THz field on SHG from the silicon surface (111).

A Ti:Sp femtosecond laser system at 795 nm with energy of 0.7 mJ, duration of 70 fs and repetition rate of 700 Hz was used in the experiment. Optical radiation was divided into two beams (see Fig.1). The pump beam was used to generate THz radiation by the tilted intensity front technique in a LiNbO3 crystal
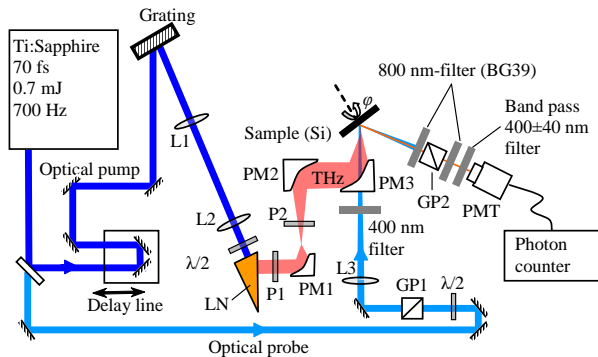
[4,5]. The terahertz radiation was

Fig. 1. Experimental setup (L1, L2, L3- lenses; PM1, PM2, PM3 – parabolic mirrors; LN – LiNbO3; GP1, GP2 – Glan-Taylor prism; P1,P2 – THz polarizer)

focused on the sample using a system of off-axis parabolas. The maximum THz field in focus reached a value of 300 kV/cm. For the attenuation of THz fields were used two THz polarizer. A probe laser pulse focused on the sample in the spot of about 100 μm (smaller than the size of the THz spot). The second harmonic radiation generated from the surface was detected by the PMT connected to the pulse counting system. The polarization properties of the SH was controlled by polarizer GP2. The special filters was used to block laser radiation.

In the course of the experiment, the generation of second harmonic at different combinations of polari-

zation of optical and THz radiation was investigated. Under application of THz field, the SH signal was significantly increased when second harmonic and THz electric fields were parallel. In the case when THz, first and second harmonic electric fields have *s* polarization, the SH signal increased by 30 times. The dependences of the SH signal on the energy of optical and THz pulses, on the delay time between them, and the dependence on the azimuthal angle (rotation angle of the sample) were investigated. In Fig. 2 an example of angular dependence is presented, where all fields (THz field, field of the first and second harmonics) have *p* polarization.
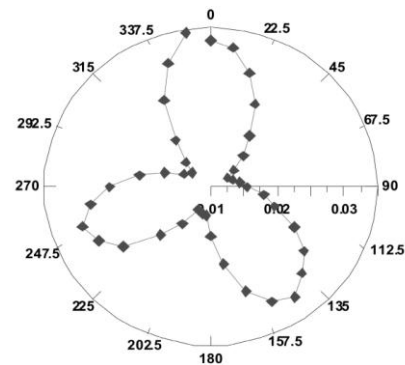
Fig. 2. Angular dependence of SH intensity: optics P-polarization, THz field P-polarization, SH P-polarization

To describe the experimental results, the phenomenological theory of second harmonic generation from (111) silicon surface was developed with account of presents of THz field. By comparison with experimental data, it was found that THz induced source of SH is in phase with the source of SH without THz field.

References

1. *Bloembergen, N., Chang, R. K., Jha, S. S., Lee, C. H.* Second-harmonic generation of light in reflection from media with inversion symmetry // Phys. Rev. 1966. V. 16, No. 22. P. 986-989.

2. *Nahata, A., Heinz, T.F.* Detection of freely propagating terahertz radiation by use of optical second-harmonic generation // Opt. Letters, 1998. V. 23, No. 1. P. 67-69.

3. *Lee, C. H., Chang, R. K., Bloembergen N.* Nonlinear electroreflection in silicon and silver// Phys. Rev. Lett. 1967. V. 18, No 5. P. 167-170.

4. *Fulop, J. A., Palfalvi, L., Almasi, G., Heblin, J.* Design of high-energy terahertz sources based on optical rectification // Opt. Express, 2010. V. 18, No. 12. P. 12311-12327

5. *Bodrov, S. B., Murzanev, A. A., Sergeev, Y.A., Malkov, Y.A., Stepanov A.N.* Terahertz generation by tilted-front laser pulses in weakly and strongly nonlinear regimes // Applied Physics Letters. 2013. V.103, No. 25. P. 251103

Dielectrics for output windows of medium power gyrotrons

Evgeny Serov[1], V. V. Parshin[1], S. V. Egorov[1], A. N. Konovalov[2], A. I. Makarov[1], K. V. Vlasova[1]

[1]Institute of Applied Physics of the Russian Academy of Sciences, Nizhny Novgorod, Russia, serov@ipfran.ru
[2]Quartz technologies Ltd, Shilovo, Ryazan' region, Russia

For achieving optimal characteristics of gyrotron it is necessary to choose a suitable material for output window. Balance of relatively low dielectric losses, slowly dependent on temperature, and relatively high thermal conductivity are required for good heat removal. Certainly, modern low loss CVD diamond windows meet these requirements, but their price is too expensive for wide application.

In this paper we present an analysis of properties of several dielectric materials: boron nitride (BN), which is currently widely used for gyrotron output windows production, crystal Quartz, and Spinel.

Basing on experimentally measured dielectric losses of these materials and on their thermal properties we made a calculation of maximal achievable output power that can be transmitted through disks made of such materials.

Boron nitride

Most of currently produced medium power (~10−100 kW) gyrotrons have output windows made of hexagonal pyrolytic BN. Its dielectric properties in sub-THz range were studied in our previous works [1,2]. Usual samples of BN have $\tan\delta \approx 10^{-3}$ at 140 GHz which is higher in comparison with other investigated materials. But the loss tangent temperature dependence is rather weak: it increases by only about 40% with temperature increasing from 25 to 700°C.

Another important characteristic is thermal conductivity of BN. Usual value used as estimate in practice is 45 W/m·K for the direction parallel the layers. However, according to the available publications [3,4], thermal conductivity of BN can reach at least 220 W/m·K for samples with high crystal perfection.

Spinel

Spinel ($MgAl_2O_4$) is ceramic material with relatively low dielectric loss which is resistant to high temperatures. In our work we studied spinel samples obtained by microwave heating of ultrafine powder components [5].

Measurements of dielectric parameters (n and $\tan\delta$) were made using high-Q resonator technique (see [1] and Refs. therein) in the frequency range 50–300 GHz at temperatures 20–200°C. Unlike BN, spinel demonstrates rather strong temperature dependence of dielectric loss. It is illustrated in Fig. 1. At temperature of about 400°C dielectric losses in spinel become higher than that in BN.
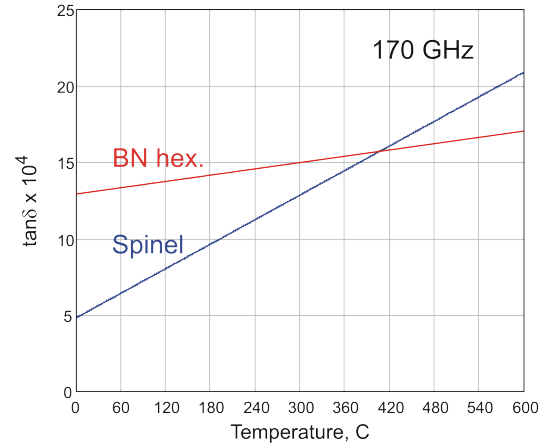
Fig. 1. Linear approximations of $\tan\delta$ temperature dependencies at f = 170 GHz based on experimental data for spinel and hexagonal BN.

Thermal properties of spinel were taken from [6]. In comparison with BN it has several times lower thermal conductivity (18 W/m·K at room temperature).

Quartz

Crystal quartz produced by Quartz Technologies Ltd was grown by the method of hydrothermal synthesis on the own raw material base of the deposit "Zhelannoe". The total concentration of impurities including alkali, gas-liquid and mineral elements does not exceed 2-3 ppm (chemical composition studies were carried out at the G.G. Devyatykh Institute of High-Purity Chemistry, ANZAPLAN analytical laboratories and QSIL laboratories). It has extremely low absorption coefficient in the optical range ($\leq 10^{-6}cm^{-1}$ at $\lambda = 1\mu m$).

Investigation of quartz sample dielectric properties was made in frequency range 65–200 GHz at room temperature. Due to specific geometric sizes of the sample only n_o component and corresponding value of $\tan\delta$ were measured. Fig. 2 demonstrates experimentally measured frequency dependence of dielectric losses in quartz along the main axis. The losses in this sample are practically the lowest ones in comparison with earlier measured samples [1].

Thermal conductivity in quartz was taken from paper [7]: 6 W/m·K for [010] direction and 13 W/m·K for [001] direction at room temperature.
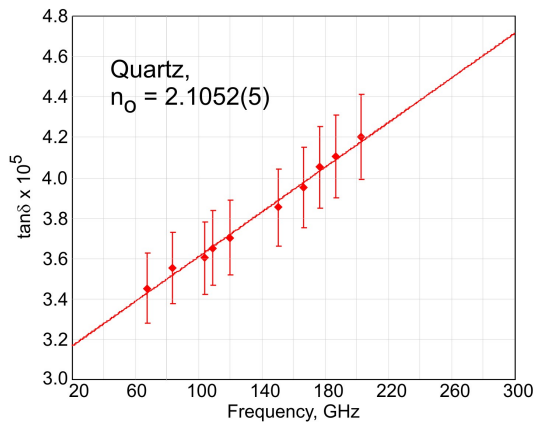
Fig. 2 Experimentally measured frequency dependence of dielectric losses in quartz for the direction parallel to the main crystal axis. Line is the linear regression.

Thermal calculation and discussion

Using data on dielectric losses and thermal properties of the samples we made a calculation of temperature distribution for a disks used as gyrotron output windows in the continuous-wave operation (CW). The calculation was made in a similar way as in [8]. We used Newton's law of cooling as the boundary condition on the perimeter. The coolant temperature was 30°C, and the coefficient of heat removal from the window perimeter was 4 W/cm^2·K. Heat flows from the window-vacuum and window-air boundaries were neglected.

The maximal output power for gyrotron windows made of BN and spinel was found as maximal beam power for which the temperature of the disk did not exceed 600°C. The thermal conductivity of BN was taken as 45 W/m·K. For quartz window the calculation is more estimative because we do not have information about the temperature dependence of tanδ. Besides, it is unlikely that quartz disk will withstand a large temperature gradient arising when the temperature of the disk center rises to 600°C. Thus, in our estimation of maximal power we limited maximal temperature of quartz to 300°C. For more strict calculation additional factors should be taken into account.

The window thickness was resonant, i.e., the optical thickness was equal to an integer number of half-wavelengths. The number of the half-wavelengths was chosen for the reason of the window strength. For disks with diameters of about 100 mm, the thicknesses ranged from 3 to 4 mm, and for disks with diameters of 30 mm (for f ~ 30 GHz), the thicknesses was 2-2.5 mm. Fig. 3 shows the maximal power transmitted through the window.

On the basis of Fig. 3 we can conclude that MgAl$_2$O$_4$ spinel is not optimal material for gyrotron output windows. Crystal quartz is a more suitable one, comparable to boron nitride in terms of maximum power level and even surpassing it at high frequencies. However, some problems associated with the use of crystal quartz may occur due to difficulty of soldering and possible mechanical stresses. Additional data on temperature dependence of tanδ are required.

Comparison of Fig. 3 (above) and Fig. 5 from [8] leads us to the conclusion that 6H-SiC disk can

transmit several times more powerful beam than BN or quartz disks. But if we use BN with high crystal perfection and high thermal conductivity then such material can also provide several hundred kilowatts level for the CW mode in the sub-THz range.
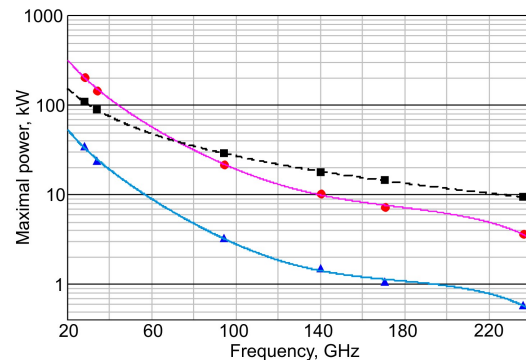
Fig. 3 Maximal output power for hexagonal BN (circles), spinel (triangles) and quartz (squares). Curves are smooth approximations. See text for details.

References

1. *Parshin, V. V., Tretyakov, M. Yu., Koshelev, M. A., Serov, E.A.* Instrumental complex and the results of precise measurements of millimeter- and submillimeter-wave propagation in condensed media and the atmosphere // Radiophys. & Quant. Electron. 2009, V. 52, No. 8. P. 525–535.

2. *Parshin, V. V.* Dielectric materials for gyrotron output windows // International Journal of Infrared and Millimeter Waves. 1994, V. 15, No. 2. P. 339–348.

3. *Sichel, E. K., Miller, R. E., Abrahams, M. S., Buiocchi, C. J.* Heat capacity and thermal conductivity of hexagonal pyrolytic boron nitride // Phys. Rev. B. 1976, V. 13, No. 10. P. 4607–4611.

4. *Duclaux, L., Nysten, B., Issi, J-P.* Structure and low-temperature thermal conductivity of pyrolytic boron nitride // Phys. Rev. B. 1992, V. 46, No. 6. P. 3362–3367.

5. *Egorov, S. V., Bykov, Yu. V., Eremeev, A. G., Sorokin, A. A., Serov, E.A., Parshin, V. V., Balabanov, S. S., Belyaev, A. V., Novikova, A. V., Permin, D. A.* Millimeter-Wavelength Radiation Used to Sinter Radiotransparent MgAl$_2$O$_4$ Ceramics // Radiophys. & Quant. Electron. 2017, V. 59, No. 8–9. P. 690–697.

6. *Harris, D. C., Linda F. Johnson, L. F., Seaver, R., Lewis, T. Turri, G., Bass, M., Zelmon, D. E., Haynes, D. N.* Optical and thermal properties of spinel with revised (increased) absorption at 4 to 5 μm wavelengths and comparison with sapphire // Optical Engineering. 2013, V. 52, No.8. 087113.

7. *Kanamori, H., Fujii, N., Mizutani, H.* Thermal Diffusivity Measurement of Rock-Forming Minerals from 300° to 1100° K // Journal of Geophysical Research. 1968, V. 73, No. 2. P. 595–605.

8. *Parshin, V., Serov, E., Denisov, G., Garin, B., Denisyuk, R., V'yuginov, V., Klevtsov, V., Travin, N.* Silicon carbide for high-power applications at MM and THz ranges // Diamond & Related Materials. 2017, V. 80, P. 1–4.

Effect of MIT in epitaxial VO$_2$ films on THz transmittance

D. I. Sharovarov[1,2], F. Ya. Akbar[1], D. P. Lelyuk[3], A. M. Makarevich[4], O. V. Boytsova[1,5], A. R. Kaul[2,4]

[1]Department of Material Science, Lomonosov Moscow State University, Moscow, Russia, dmitrii.sharovarov@gmail.com
[2]Oxyfilm LLC, Moscow, Russia
[3]Institute for Theoretical and Applied Electromagnetics RAS, Moscow, Russia
[4]Department of Chemistry, Lomonosov Moscow State University, Moscow, Russia
[5]Kurnakov Institute of General and Inorganic Chemistry RAS, Moscow, Russia

The development of THz technologies (communication, imaging, spectroscopy etc.) requires the design of materials for high-speed modulation of radiation in THz range. For such applications, the thin films based on oxides showed a metal-insulator transition (MIT) are interesting due to large different of optical transmittance before and after critical point. Among the oxide materials with MIT vanadium dioxide, which has a transition temperature the closest to the room temperature (68°C for bulk samples), is of particular interest, with the MIT characterized by a record speed (<1 ps) and a large amplitude (a change in the conductivity is 10^5 times for single crystals). It is known that the MIT transition in VO$_2$ is accompanied by a first-order phase transition, while the crystalline structure from the monoclinic (crystal type MoO$_2$) with the properties of the semiconductor transforms into a tetragonal (rutile type) with metallic conductivity. The electronic transition in the vanadium dioxide can be caused by the temperature, the electric field and laser radiation. A set of these unique properties makes vanadium dioxide a promising key component of optoelectronic devices (switches, modulators, lenses, etc.) for the THz range controlled by thermal action, electric voltage or laser pulse.

Recently the efforts of numerous researches were directed to the vanadium dioxide in the form of thin epitaxial films of thickness (100-500 nm) on optically transparent single-crystal substrates (Al$_2$O$_3$, TiO$_2$). The epitaxial VO$_2$ films exhibit the sharp transition with an amplitude changes in conductivity up to four orders of magnitude and showed above 90% change of THz transmission.
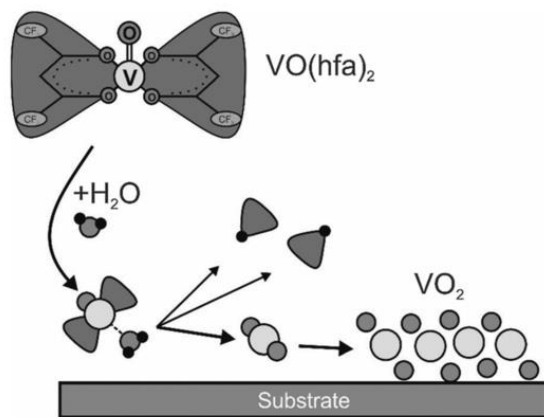
Fig. 1. The scheme of reaction between VO(hfa)$_2$ molecule and water resulted to formation of VO$_2$.

The properties of vanadium dioxide are very sensitive to the concentration of defects, morphology, contact between crystallites, impurities of other elements. The synthesis of epitaxial films of vanadium dioxide, extremely limited by a narrow region of homogeneity and a high sensitivity to the partial pressure of oxygen, is a complex problem, which resulted in a low reproducibility of the composition and properties of films obtained in different scientific groups.

The method of chemical vapor deposition is a promising method for the production (on an industrial scale) of vanadium dioxide films demonstrating the properties of an optical switch in the THz range, however, provided a simple and effective process for obtaining high-quality samples that are not contaminated with impurity phases. In the case of materials sensitive to the oxygen partial pressure, the use of water vapor for destruction of the vanadium containing molecules makes possible to obtain stoichiometric VO$_2$ due to stabilization of vanadium oxidation state +4 and to carry out the deposition process at low temperatures (> 350°C) without carbon contamination of the film. In our work we performed the deposition of epitaxial (001)VO$_2$ films on r-Al$_2$O$_3$ substrates (diameter 1-3 inches) by gas-phase reaction between vapors of vanadyl diketonates VO(dik)$_2$ (dik$^-$ = acac$^-$, thd$^-$, hfa$^-$) and water in argon atmosphere at temperature range 350-600°C.
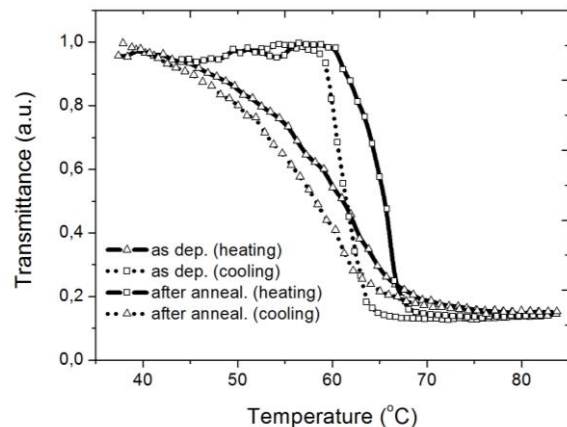
Fig. 2. The THz transmittance of VO$_2$/r-Al$_2$O$_3$ (as deposited and after annealing) films at different temperature.

Among the many factors that influences on the nature of the MIT in vanadium dioxide, the film microstructure plays one the most important role. Fine-grained films that have a large number of partially oxidized grain boundaries show a diffuse hysteresis

loop and a smaller amplitude of the resistance change. The increase of the grain size can be achieved either by increasing the substrate temperature, or by using an additional heat treatment. In the first case, the formation of a partially oxidized grain surface is not prevented, whereas additional annealing successfully solves this problem due to the peritectic decomposition of the oxidized phases occurs to VO_2 and trace amounts of the melting phases promoting recrystallization process. The samples obtained by MOCVD process were annealed under conditions of controlled oxygen partial pressure at temperature range 550-650°C resulted in increasing of grain size, changing of morphology, electrical and optical properties. It was investigated the films composition, structure, morphology and physical properties.

Measurements of the THz transmission as a function of temperature were carried out on a pulsed THz spectrometer. It was demonstrated the effect of films synthesis on the contrast of transmission in the dielectric and conducting state. The shape of the hysteresis loop differs from the resistance curve and is somewhat shifted downward in temperature associated with percolation of conductive grains into the insulation matrix. For large-scale substrates the maps of THz amplitude change were analyzed.

Moreover most of practical applications require non-trivial shape and design of functional optical elements, then it is important to have possibility to realize the chemical lithography operations that accurately was demonstrated in this work.
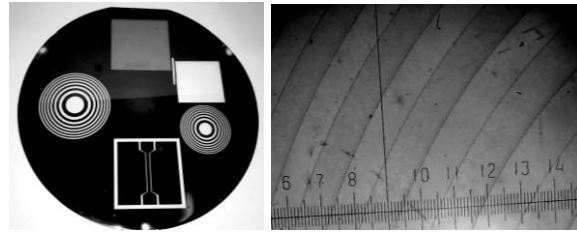
Fig. 4. The different patterns on 3-inch VO_2 film/Al_2O_3 obtained by photolitographic etching process.

Fig. 3. The THz transmittance of 3-inch VO_2 films on r-Al_2O_3 at different position from the center (10 mm).

44

Investigation of the properties of a 3-level broadband antireflective structure on silicon by THz time-domain spectroscopy

I. A. Tzibizov[1], G. I. Kropotov[1], V.S. Pavelyev[2,3], K. N. Tukmakov[2,3], A. S. Reshetnikov[2]

[1]Tydex LLC, 16, Domostroitelnaya st., 194292, St. Petersburg, Russia
[2]Samara University, 34, Moskovskoe shosse, Samara, 443086, Russian Federation
[3]Image Processing Systems Institute of the Russian Academy of Sciences, 151, Molodogvardejskaya st., Samara, 443001, Russian Federation

The realization of a broadband antireflective coating in the THz range has been an urgent problem for many years. At present, only narrow-band antireflection coatings made on the basis of a single-layer coating are commercially available [1].

Here we want to present the results of the study of properties of a 3-level broadband antireflective (BBAR) structure on low-resistance silicon by THz time-domain spectroscopy (THz-TDS). BBAR structure was developed as a part of the manufacturing of a broadband THz radiation absorber, which can be used as a sensitive element of THz radiation detectors [2].

Since low-resistance silicon has a high absorption in the THz range, it was decided to use it as a substrate for a THz. To increase the amount of absorption, it is necessary to reduce losses associated with Fresnel reflection. For this, it was decided to create an antireflection coating on one side of the silicon substrate [3, 4].

To provide broadband antireflection effect, on the one side of the substrate a 3-level structure has been realized by use of reactive ion etching (Bosch process) [3, 5].

Sample device was fabricated from p-type $\rho=0.54$ Ohm·cm silicon substrate with a diameter of 50 mm and thickness of 500 μm (Fig. 1).
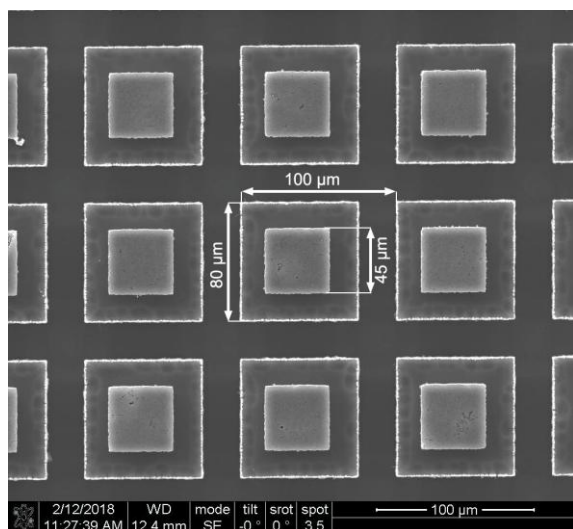
Fig. 1. Scanning electron microscope (SEM) images of the produced sample

To characterize the antireflection properties of the produced sample, the transmission and reflection measurements were carried out on the Tera K8 te-rahertz time-domain spectroscopy (THz-TDS) system (produced by Menlo Systems Gmbh).
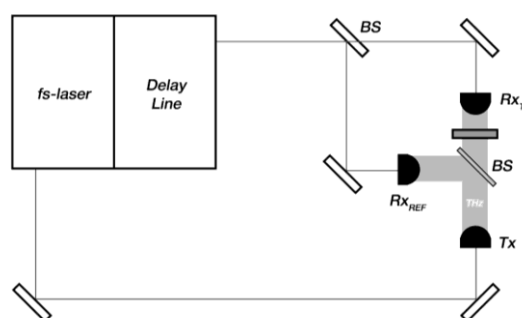
Fig. 2. Experimental setup

Tera K8 spectrometer operates in 0.2-2.5 THz range. Spectral resolution – 5 GHz. The experimental setup is shown on Fig. 2. Both, bare silicon substrate and fabricated sample with 3-level antireflection structure were measured. Reflectance was measured under the normal angle of incidence. The value of Fresnel reflection decreased from 28-30% to less than 3% in 0.5 – 2 THz range (Fig. 3).
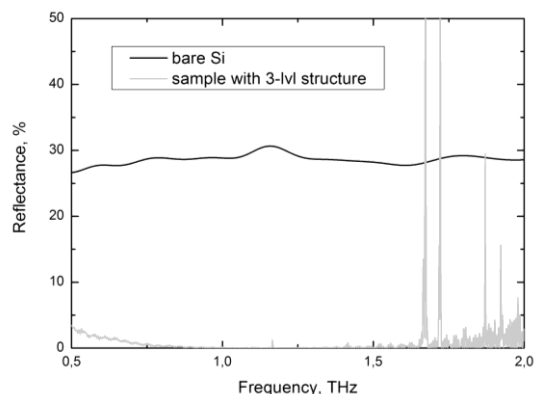
Fig. 3. Reflectance spectra of the fabricated sample

It can be concluded that fabricated structure can be used for reducing of reflection losses at the air-silicon interface of transmissive silicon optical elements in the broad range of the THz range frequencies. Also, it could be optimized for the certain frequency range.

References

1. *A. J. Gatesman, J. Waldman, M. Ji, C. Musante, and S. Yngvesson*, An Anti-Reflection Coating for Silicon Optics at Terahertz Frequencies // IEEE Microwave and Guided Wave Letters, 10, 7, pp 264 – 266 (2010).

2. *J. Lehman, A. Sanders, L. Hanssen, B. Wilthan, J. Zeng, C. Jensen*, Very black infrared detector from vertically aligned carbon nanotubes and electric-field poling of lithium tantalite // Nano Letters, 10, 3, P. 3261 (2010).

3. *A.N. Agafonov, B.O. Volodkin, A.K. Kaveev, B.A. Knyazev, G.I. Kropotov, V.S. Pavel'ev, V.A. Soifer, K.N. Tukmakov, E.V.Tsygankova, Yu.Yu. Choporova*, Silicon diffractive optical elements for high-power monochromatic terahertz radiation, Optoelectronics, Instrumentation and Data Processing, 49, pp. 189-195 (2013)

4. *C. Brückner, T. Käsebier, B. Pradarutti, S. Riehemann et al*., Broadband antireflective structures applied to high resistive float zone silicon in the THz spectral range, Optics Express, 17, 5, P. 3064 (2009).

5. *A.N. Agafonov, B.O. Volodkin, D.G. Kachalov, B.A. Knyazev, G.I. Kropotov, K.N. Tukmakov, V.S. Pavelyev, D.I. Tsypishka, Yu.Yu. Choporova, A.K. Kaveev*, Focusing of Novosibirsk Free Electron Laser (NovoFEL) radiation into paraxial segment, Journal of Modern Optics, 63, 11,pp. 1051-1054 (2016)

Recent results on THz gyrotron-based molecular spectroscopy

Golubiatnikov G.Yu., Koshelev M.A., Tsvetkov A.I., Fokin A.P., Glyavin M.Yu., and Tretyakov M.Yu.

Institute of Applied Physics RAS, Nizhny Novgorod, Russia, koma@ipfran.ru

Method of opto-acoustic (also called radio- or photo-acoustic) molecular spectroscopy is a powerful tool for both fundamental studies and applications. In this method the result of the interaction of the radiation with matter is detected by the change of the parameters of the matter and not of the radiation. It is likely the only method allowing reaching high sensitivity at reasonable recording time by increasing radiation power. This was particularly demonstrated in the teraherz (THz) region in our recent work [1] using spectrometer with radio-acoustic detection of absorption (RAD spectrometer) [2] and radiation of the free-running 263-GHz gyrotron operating in continuous wave regime with up to 1 kW output power [3].

Further improvement of the spectrometer sensitivity and its use for spectroscopy requires precise control of the gyrotron radiation frequency. A phase-locked loop (PLL) against a signal of the reference oscillator was used in order to control the gyrotron modulating anode voltage [4]. The PLL system, which block diagram is presented in Fig. 3, is similar to that used for backward wave oscillator (BWO) [5]. A specially designed fast voltage control unit can vary voltage within 0-1 kV with a speed of somewhat faster 1 kV/μs. Preliminary testing of the control system showed a modulation bandwidth of 150 kHz, defined by the time constant of the gyrotron anode circuit.
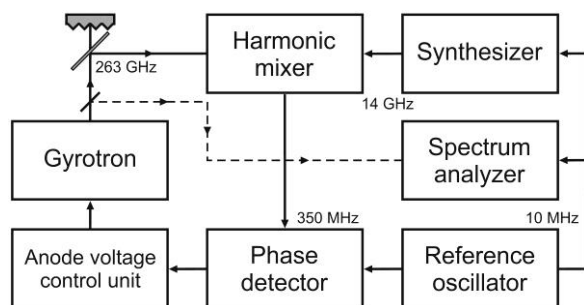
Fig. 1. Block diagram of the phase-locked loop units for a sub-THz gyrotron.

The principle of its operation is following. Part of the output radiation of the 263-GHz gyrotron is transmitted to the harmonic mixer, where it is mixed with the a harmonic of the signal from a microwave synthesizer with a frequency of about 14 GHz. The resulting signal at an intermediate frequency of 350 MHz is then directed to the phase detector for a frequency-phase comparison with the harmonic of a quartz clock serving as the reference oscillator. The error signal from the phase detector is then used as a control signal for the anode voltage control unit. In addition, the radiation spectrum was analized by

Keysight spectrum analyzer N9010A equipped with an external mixer. Phase-locking the gyrotron frequency reduced the radiation spectrum width from 0.5 MHz for a free-running gyrotron down to about 1 Hz for the stabilized gyrotron (Fig. 2) which corresponds to relative frequency stability $\Delta f/f \sim 3 \cdot 10^{-12}$ for a measurement time of a few seconds.
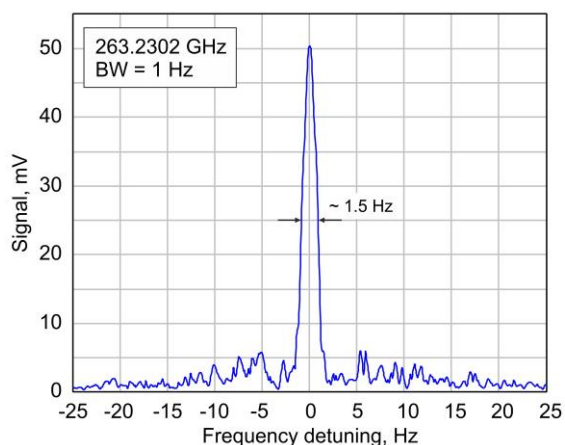
Fig. 2. Frequency spectrum of the gyrotron observed at 263.2302 GHz with phase-locked loop. Bandwidth of the spectrum analyzer was 1 Hz.

Our recent spectroscopic study using RAD method and a free running gyrotron facility [1] revealed the necessity for modulation of the gyrotron frequency aimed at reduction of the spectrometer baseline. It became possible by implementation of the PLL system of the gyrotron. Typical recordings of SO_2 line obtained using RAD spectrometer and gyrotron radiation at approximately 1 W power are shown in Fig. 3. Modulation of either radiation power (Fig. 3A) or its frequency along with synchronous signal detection at the first (Fig. 3B) and second (Fig. 3C) harmonic of the modulation frequency were applied for spectra recording. The line asymmetry due to baseline is clearly observed from the experimental spectra in case of power modulation in Fig. 3A. The situation is even worse if a weaker line is studied. Use of the frequency modulation decreases influence of the baseline on the line shape which is seen in Figs. 3B and 3C.

Experimental spectrum of a mixture of SO_2 (0.027 Torr) and Ar (0.26 Torr) was registered in the frequency range 263-264 GHz using RAD method and gyrotron radiation of about 0.5 W power (Fig. 4A). Calculated spectrum shown in Fig. 4B was modeled using Lorentz profile and line parameters from HITRAN and JPL catalogs.
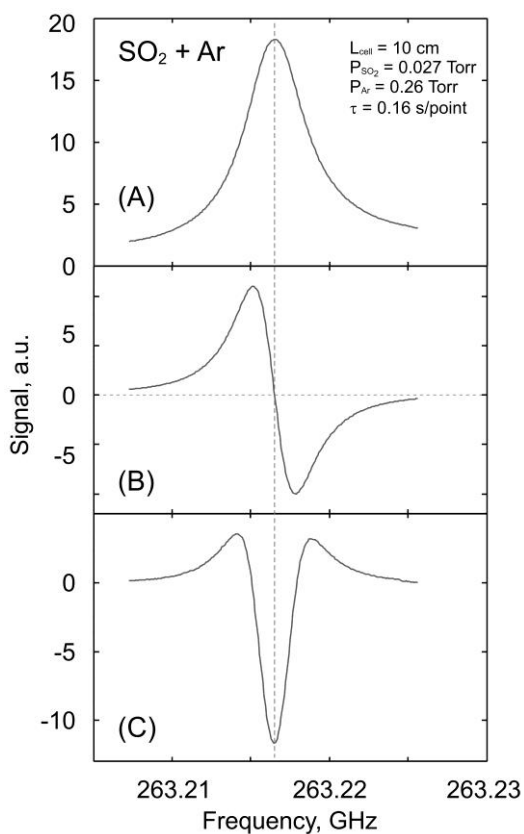
Fig. 3. Experimental recordings of the $44_{6,38} - 45_{5,41}$ line of $^{32}S^{16}O_2$ in a mixture with argon obtained using RAD spectrometer and gyrotron radiation (~ 1 W). (A) - modulation of the radiation power; (B) and (C) - modulation of the radiation frequency and signal detection at first (B) and second (C) harmonic of the modulation frequency (180 Hz).

It follows from the comparison of these two spectra that only some of the observed lines of the well-studied spectrum of SO_2 can be assigned to the tabulated ones. Futher analysis of the experimental spectra revealed that unassigned lines are narrower than the assigned ones. This may indicate that these lines arise from an interaction of absorbing molecules with radiation at second, third, etc. harmonics of the fundamental frequency. Calculated specta in the 526-528 GHz and 789-791 GHz ranges are shown in Fig. 4B and 4C, respectively (note frequency scales normalized by the corresponding harmonic number). Comparison of the calculated spectra with the experimental one confirmes presence of radiation at second and third harmonics of the gyrotron fundamental frequency. Using known parameters of SO_2 lines we estimated relative fraction of the radiation power coming to the gas cell at second harmonic as ~ 1% of the full power and ~ 0.1% for the third harmonic. Routine sensitivity of the spectrometer was determined from spectra analysis as ~ $8 \cdot 10^{-10}$ cm^{-1} (at 2-s time constant), which is limited by the power saturation effect of the molecular transition.

Results were confirmed by the high resolution spectra obtained using a BWO-based video spectrometer.
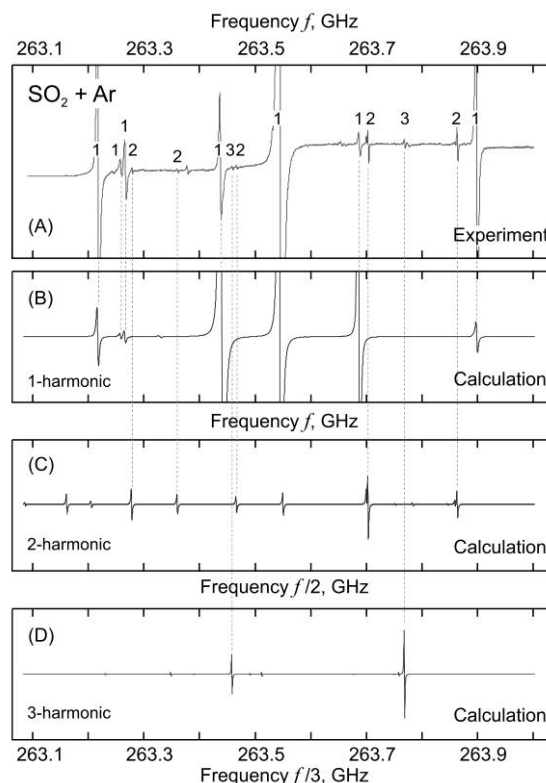
Fig. 4. (A) Experimental spectrum of a mixture of SO_2 and Ar obtained using RAD and gyrotron radiation of ~ 0.5 W power. Lines belonging to the 1st, 2nd and 3rd harmonics of radiation frequency are denoted by the corresponding numbers. (B,C and D) Calculated spectra of SO_2. Frequency scales are normalized by the corresponding harmonic number.

References

1. *Koshelev M.A., et al.* Molecular Gas Spectroscopy Using Radioacoustic Detection and High-Power Coherent Subterahertz Radiation Sources // J. Molec. Spectrosc. 2017. V. 331, P. 9-16.

2. *Tretyakov M.Yu., et al.* Precise Measurements of Collision Parameters of Spectral Lines with a Spectrometer with Radioacoustic Detection of Absorption in the Millimeter and Submillimeter Ranges // Instrum. Exp. Tech. 2008. V. 51. P. 78–88.

3. *Glyavin M.Yu., et al.* Experimental tests of a 263 GHz gyrotron for spectroscopic applications and diagnostics of various media // Rev. Sci. Instr. 2015. V. 86 N. 5 P. 054705.

4. *Fokin A. et al.* High-power sub-terahertz source with a record frequency stability at up to 1 Hz // Scientific Reports. 2018. V. 8. P. 4317.

5. *Krupnov A.F.* Phase Lock-In of MM/SUBMM Backward Wave Oscillators: Development, Evolution, and Applications // Int. J. IR MM Waves. 2001. V. 22. P. 1-18.

H₂O Molecules Hosted By A Crystalline Matrix – New State Of Water?

Elena S. Zhukova[1], M. A. Belyanchikov[1], M. Savinov[2], P. Bednyakov[2], V. G. Thomas[3],
L. S. Kadyrov[1], E. A. Simchuk[1], Z. V. Bedran[1], V. I. Torgashev[4], A. Dudka[5], M. Dressel[1,6],
B. P. Gorshunov[1].

[1] Moscow Institute of Physics and Technology, Dolgoprudny, Moscow Region, 141700 Russia, zhukova.es@mipt.ru
[2] Institute of Physics AS CR, Na Slovance 2, 18221 Praha 8, Czech Republic
[3] Institute of Geology and Mineralogy, RAS, 630090 Novosibirsk, Russia
[4] Faculty of Physics, Southern Federal University, 344090 Rostov-on-Don, Russia
[5] Shubnikov Institute of Crystallography, Federal Scientific Research Centre "Crystallography and Photonics", Russian Academy of Sciences, 119333 Moscow, Russia
[6] 1. Physikalisches Institut, Universität Stuttgart, 70569 Stuttgart, Germany

Along with the liquid and solid phases of water, there are many natural and artificial systems and objects - biological, geological, meteorological, physical, chemical, etc., in which water molecules are found in nano-confined state. As in the case of any other material, in such conditions water must acquire qualitatively new characteristics and properties that it did not possess in its macroscopic liquid state. Currently, there is a surge of active research on such properties, which is stimulated by the importance of obtaining new knowledge about the environment, the need to solve actual problems of medicine and public health, the creation of qualitatively new devices, mechanisms and technologies, materials with new characteristics that are promising for use in bio-sensors, diagnostics and in many other applications. It is known that the properties of liquid water remain less understood in comparison with other liquids, which is largely due to the ability of H₂O molecules to form hydrogen bonds with each other. Under the conditions of a nano-confinement these properties will become even more exotic, diverse and complex, especially in complex systems such as biological. Therefore, the most effective would be to study first as simple system as possible. We have studied an array of *single* H₂O molecules distributed over a periodical matrix of nano-sized cages inside the crystal lattice of dielectrics, see Fig.1. The advantages of such objects are the absence of short-range intermolecular hydrogen bonds (the distance between the pores is 5-10 Angstroms), the complete certainty of the spatial arrangement of the cages, and hence the H₂O molecules, as well as the known type and magnitude of the interaction of molecules with the environment (weak van der Waals bonds) and between themselves (long-range electric dipole-dipole interaction). Importantly, these factors are essential from the point of view of simplifying and hanging the accuracy of the model analysis (molecular dynamics, density functional methods, ...) of the properties of the subsystem of water molecules.

Using broad-band spectroscopy (frequencies from ~1 Hz up to the visible, temperatures from 300 K down to 0.3 K) we have studied specific single-particle and collective excitations of water molecular ensemble hosted by dielectric crystalline matrices of hexagonal beryl Be₃Al₂Si₆O₁₈ and orthorhombic cordierite

$(Mg,Fe)_2Al_4Si_5O_{18}$. Experiments on dehydrated crystals allowed to identify spectral features connected exclusively with the response of water molecular subsystem. We observe well-known H₂O intramolecular modes together with librational and rattling-like translational excitations of separate water molecules confined within the nano-cages. Using density-functional and molecular dynamics approaches allowed us to identify the origin of the single-particle modes. In crystals of beryl containing both, regular and heavy water molecules we discovered an incipient ferroelectric state within water molecular subsystem that manifests itself in the form of a Curie-Weiss temperature dependence of quasi-static permittivity

$$\varepsilon'(T) = \varepsilon_\infty + C(T - T_C)^{-1},$$

where ε_{inf} is the high-frequency dielectric constant, C and T_C are the Curie constant and Curie temperature, respectively. Below ≈10 K the behavior $\varepsilon'(T)$ saturates that can be described by the Barrett expression [1]
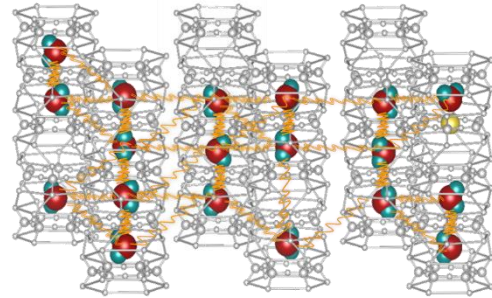
Fig. 1. Schematic view of a crystal lattice of beryl with nano-sized cages formed by ions of crystal lattice. The cages are arranged in channels that are elongated along crystallographic c-axis. Single water molecules are captured within the cages during crystal growth. The distance between H₂O molecules along the channels is about 5 Angstroms and between H₂O molecules in neighboring channels about 10 Angstroms. Orange lines denote intermolecular electric dipole-dipole interaction.

$$\varepsilon' = \varepsilon_\infty + \frac{C}{\frac{T_1}{2}\coth\frac{T_1}{2T} - T_c}$$

where C is constant and T_1 gives the energy scale of quantum fluctuations that are suppressing the macroscopic ferroelectric phase transition. We suggest that
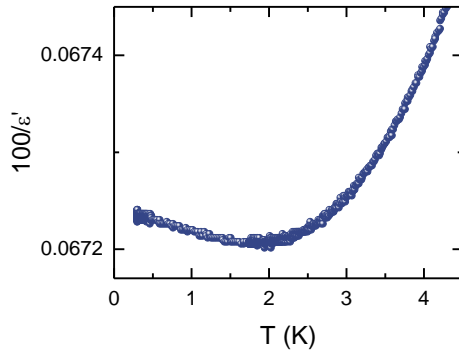
quantum tunneling is responsible for the suppression of ferroelectric phase transition, as confirmed by neutron experiments [2].

Fig. 2. Temperature-dependent inverse dielectric permittivity of an array of nano-confined water molecules in beryl crystalline matrix measured at 1 kHz.

As seen from Fig.2, the inverse dielectric permittivity displays weak minimum at the lowest temperatures. This effect can be considered as either coming from onset of short-range spatial ferroelectric (antiferroelectric) correlations between the dipole moments or signs of quantum critical behavior of water molecular electric dipoles. Further experiments are needed to clarify this point.

The specific potential profile experienced by the water molecules localized within the nano-cages of cordierite leads to emergence of an overdamped temperature dependent relaxation at radiofrequencies and a rich set of excitations in the terahertz range. The origin of both types of excitations needs detailed investigation.

In conclusion, spectroscopic studies of an array of dipole-dipole interacting water molecules localized within nano-sized cages of crystal lattice of dielectrics demonstrate a rich set of excitations that are not observed in liquid water. The corresponding H_2O molecular network can thus be considered as a model system whose studies will allow to proceed to investigations of more complicated water-containing objects.

References

1. *Barrett, J. H.* Dielectric constant in perovskite type crystals // Phys. Rev. 1952. V. 86, P. 118–120.
3. *Kolesnikov A. I.* et al. Quantum tunneling of water in beryl: a new state of the water molecule // Phys. Rev. Lett. 2016. V. 116, P. 167802.

Millimeter-Wave Spectroscopy of Weakly Bound Molecular Complexes and Small Clusters

L. A. Surin[1,2]

[1]Institute of Spectroscopy, Troitsk, Moscow, Russia, surin@isan.troitsk.ru
[2]I. Physikalisches Institut, University of Cologne, Cologne, Germany

Currently, there are a number of international projects on a full-scale study of the infrared and submillimeter-wave (SMMW) radiation in space, such as the Space Observatory "Herschel" (mission is completed, analysis of the data is in progress), the Stratospheric Observatory "SOFIA" based on a Boeing-747SP wide-body aircraft, astronomical interferometer of MMW and SMMW telescopes in the Atacama Desert of northern Chile "ALMA", and many others. The demand of high-level spectroscopic data, including the parameters of interaction between abundant in the interstellar space molecules and atoms, is extremely high, because it is necessary for the interpretation of the information coming from the radio telescopes. Many laboratory and theoretical research directed on the understanding of the interaction between ammonia (NH_3), water (H_2O), carbon monoxide (CO), nitrogen (N_2), etc. and their main partners by the collisions in the interstellar medium - molecular hydrogen H_2 and atomic helium He [1, 2]. These data are then used to test intermolecular interaction potentials, and they provide the necessary background for the development for the astrophysical models.

Another application, in which the intermolecular interactions with He and H_2 play an important role, is the doping of helium or *para*-hydrogen clusters with a probe molecule to perform high resolution spectroscopy. Such experiments are directed on the detection of superfluid response of molecular rotation in the He and *para*-H_2 clusters [3].
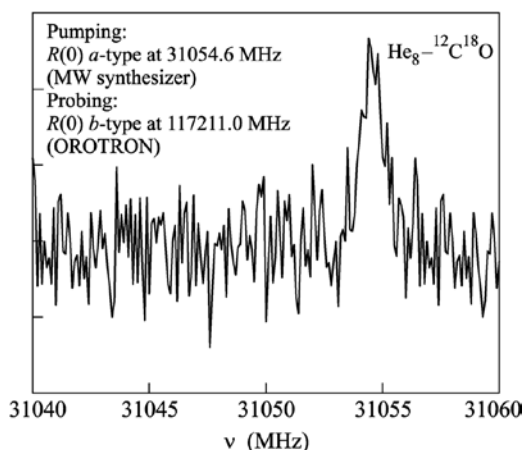
Typically, microwave (MW) spectra provide information about ground state *end-over-end* pure rotational energy levels of the complexes, MMW spectra give access to their internal rotor states, and SMMW or THz wavelengths probe intermolecular vibrations. Gas phase high resolution spectroscopic data give unambiguous information on the dynamics, composition, and structure of the complexes, because their bound states are very sensitive to the interaction potential.

The overview of the spectroscopic methods as well as recent results on molecular complexes and small clusters are presented.

OROTRON Spectrometer with Supersonic Jet

In OROTRON, the MMW radiation is produced by interaction of an electron beam with the electromagnetic field of an open Fabry-Perot resonator. The principal scheme of the spectrometer is shown in Fig. 1. In order to allow the measurements in the molecular jet expansion, the entire OROTRON is placed into a vacuum chamber. The high vacuum part of the OROTRON includes the cathode, the collector and the fixed plane mirror with a periodic structure ruled on its surface. This part is separated from the rest of the resonator by a thin mica window, which is transparent to the MMW radiation. The second part of the OROTRON consists of a movable spherical mirror. These two parts are connected to each other by a hollow brass cylinder with two openings for the propagation of a molecular jet through the resonator.

Absorption inside the resonator is sensitively detected by measuring the appropriate change of the electron current in the collector circuit. The principle of the method is that a change in the quality factor of the resonator due to the absorption in the gas will cause a change in the velocity distribution of the electrons and thus in their passage to the collector [4].

The double resonance option strongly helps in the identification of complex spectra. If one of the two transitions in a three level system is saturated, the populations of the levels and, correspondingly, the radiation absorption intensity in the second transition change. Therefore, the absorption of radiation from an additional source in the first transition can be detected in a change in the signal of the spectrometer tuned to the second transition. As shown in Fig. 1, the OROTRON spectrometer assumes the role of signal detection, while the microwave pump radiation is delivered by a microwave synthesizer followed by a high power broadband amplifier (2-110 GHz). The molecular beam travels perpendicular to both MMW and MW radiation beams and interacts simultaneously with them.

Fig. 1. Schematic diagram of the OROTRON jet spectrometer (100-150 GHz) with MW–MMW double resonance arrangement.

This technique was applied to study many weakly bound van der Waals systems [5]. Fig. 2 shows one example of a 20 MHz survey for $R(0)$ transitions of the He_8–$^{12}C^{18}O$ cluster [3].

Pumping:
$R(0)$ a-type at 31054.6 MHz
(MW synthesizer)
Probing:
$R(0)$ b-type at 117211.0 MHz
(OROTRON)

He_8–$^{12}C^{18}O$

Fig. 2. Record of the $R(0)$ transition in the He_8–$^{12}C^{18}O$ cluster by the double resonance method with OROTRON.

Supersonic Jet Spectrometer for Terahertz Applctions (SuJeSTA)

For measurements of the weakly bound van der Waals NH_3–H_2 complexes the SuJeSTA spectrometer (150-800 GHz) [6] was applied. Details of the current experimental setup used in the Astrophysics group of the University of Kassel for carbon clusters experiments are shown in Fig. 3. A microwave synthesizer is used as a radiation source, followed by a frequency multiplier. The SMMW radiation intersects a pulsed supersonic jet ~5 cm downstream in a perpendicular configuration.

A multi-pass optics is used to further enhance the signal-to-noise ratio. The absorption signal is detected by a low-noise liquid-He cooled hot electron bolometer. The frequency of the synthesizer is modulated at 40 kHz, and phase sensitive detection of the signal is achieved by a lock-in amplifier in $2f$-mode operation. In addition to the frequency modulation of the radiation source, an on–off modulation of the jet is used for background subtraction through a pair of boxcar integrators. The combination of frequency and source modulation substantially improves the S/N ratio and at the same time suppresses standing wave effects.
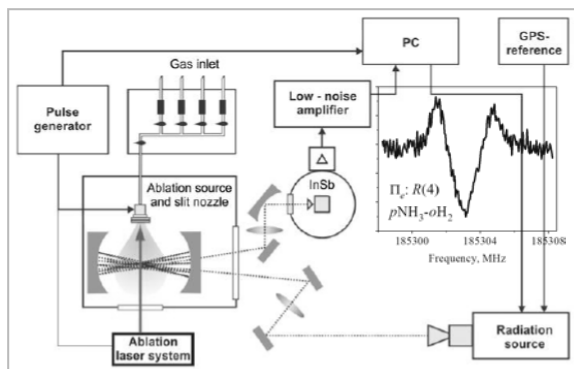

Fig. 3. SuJeSTA spectrometer (150-800 GHz) with multi-pass cell and recorded line of the pNH$_3$–oH$_2$ complex.

Double Resonance Spectroscopy with Cryogenic Ion Trap Apparatus

A novel action spectroscopic method for rotational spectroscopy of weakly bound complexes, which has been recently developed in the Spectroscopy group of the University of Cologne. This method uses a double resonance consisting of a rotational transition (MMW) followed by a predissociating transition (IR), and uses the final destruction of the complex as the spectroscopic action signal. This approach was applied to obtain high-resolution rotational data of the He–HCO$^+$ complex. HCO$^+$ is particularly interesting because it is probably the most abundant molecular ion in dense cores of interstellar molecular clouds and its complex with He is regarded as reaction intermediate of the proton exchange reaction.

The experiments have been carried out in the 22-pole ion trap machine COLTRAP [7]. The spectroscopic parameters of the ground state have been determined to microwave precision, thus providing the most reliable reference data for testing available He–HCO$^+$ interaction potentials.
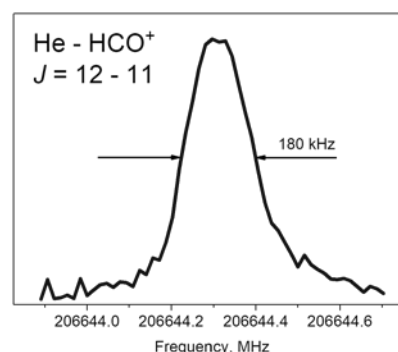
He - HCO$^+$
$J = 12 - 11$
180 kHz

Fig. 4. Example for the double resonance technique applied to the He–HCO$^+$ complex.

References

1. *Green S., Thaddeus P.* Rotational excitation of CO by collisions with He, H, and H$_2$, under conditions in interstellar clouds // Astrophys. J. 1976. V. 205, P. 766-785.

2. *Chefdeville S., Stoecklin T., Naulin C., et. al.* Experimental and theoretical analysis of low-energy CO + H$_2$ inelastic collisions // Astrophys. J. Lett. 2015. V. 799, L9.

3. *Surin L.* Nonclassical rotations of single molecule in small helium and hydrogen clusters: manifestation of "microscopic superfluidity" // JETP Lett. 2013. V. 97, P. 57-65.

4. *Surin L.A., Dumesh B.S., Lewen F., Roth D.A., et. al.* Millimeter-wave intracavity-jet OROTRON-spectrometer for investigation of van der Waals complexes // Rev. Sci. Instrum. 2001. V. 72, P. 2535-2542.

5. *Dumesh B.S., Surin L.A.* Unusual rotations in helium and hydrogen nanoclusters and "nanoscopic" superfluidity // Physics-Uspekhi. 2006. V. 49, P. 1113-1129.

6. *Surin L.A., Tarabukin I.V., Schlemmer S., Breier A.A., Giesen T. F., et. al.* Rotational spectroscopy of the NH$_3$–H$_2$ complex // Astrophys. J. 2017. V. 838, Art. 27.

7. *Salomon T., Töpfer M., Schreier P., Schlemmer S., Asvany O., Kohguchi H., Surin L.* Double Resonance Rotational Spectroscopy of He–HCO$^+$ // Phys. Chem. Chem. Phys. 2018.

Nonlinear quantum interferometry in terahertz spectroscopy

E.I. Malkova[1], S.P. Kovalev[2], K.A. Kuznetsov[1], G.Kh. Kitaeva[1]

[1]M.V. Lomonosov Moscow State University, Moscow, Russia, 119991
[2]Helmholz Zentrum Dresden Rossendorf, Dresden, Germany, 01328

At present time, biphoton fields are widely studied both in quantum optics and spectroscopy. There are many experimental and theoretical works devoted to nonlinear interferometers [1-5]. However, there is a lack of studies of generation for optical-terahertz biphotons in nonlinear interferometers. The goal of this work to analyze the possibility of observation for interference of the optical-terahertz biphoton fields in Young and Mach-Zehnder schemes, and calculating the angular-frequency intensity patterns at the output of the interferometers.

Earlier a special approach was applied for measuring of the dielectric function imaginary part at THz frequencies, based on the analysis of visibility of three-wave interference under spontaneous parametric down-conversion (SPDC) in the Young scheme [6]. The experiments were performed using SPDC-based three-wave interferometric technique in geometry of near-forward Raman scattering by phonon polaritons. This technique provides measuring absorption coefficients at frequencies of infrared and terahertz phonon polaritons using crystal samples of any arbitrary length with respect to propagation depth of absorbed waves.

In this paper, we calculated the frequency-angular spectrum of the biphoton field at the output of the nonlinear Mach-Zehnder interferometer in the regime of strongly frequency-non-degenerate parametric light scattering. The lithium niobate crystal doped by magnesium ($LiNbO_3$: Mg) was considered as a model of a nonlinear interferometer (Fig.1), as two plates of thickness L with a layer L ' of the other medium being placed between them. The scattering geometry was chosen as follows: x(y,y) xz.
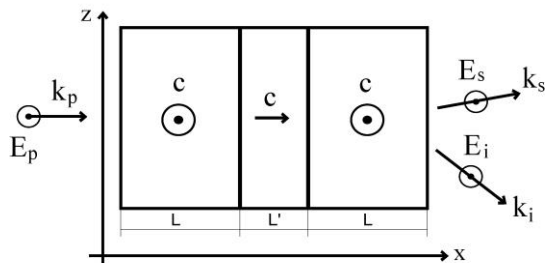
Fig. 1. The geometry of the nonlinear Mach-Zehnder interferometer, c - the optical axes of lithium niobate crystals.

It is well known that frequency-angular SPDC spectrum from one $LiNbO_3$ crystal can be written as:

$$I_1(\theta_s, \omega_i) \propto \left(\frac{\sin(\delta_x / 2)}{\delta_x / 2} \right)^2 \cdot \left(\frac{\sin(\delta_z / 2)}{\delta_z / 2} \right)^2 \qquad (1)$$

where δ_x, δ_z – longitudinal and transversal wave mismatches, respectively. According to [4], the modulation function of the middle layer was calculated as:

$$m(\theta_s, \omega_i) = \cos^2 \left(\frac{\delta_x + \delta'_x}{2} \right) \qquad (2)$$

The resulting interference pattern is described by the following expression:

$$I(\theta_s, \omega_i) \propto I_1(\theta_s, \omega_i) m(\theta_s, \omega_i) \qquad (3)$$

Two lithium niobate plates of 0.023 cm thickness with Mg content 5.1 mol% MgO were oriented as in Fig.1. The axes of the crystals are perpendicular to the wave pump vector, so eee- interaction was realized. In order to avoid the total internal reflection of idler wave at the boundary of a lithium niobate crystal, a material with a sufficiently high refractive index (~6) should be used as an intermediate layer. Between the plates of the interferometer is placed another plate of $LiNbO_3$: Mg with a thickness of 0,007 cm with a Mg content of 4.1 mol% MgO. The optical axis of this layer was parallel to the wave pump vector.
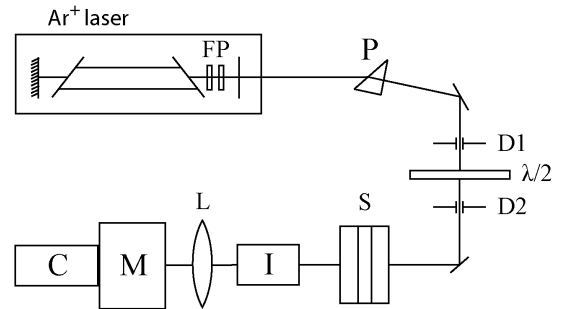

Fig. 2. Schematics of the experimental setup.

Measurements were carried out using Ar+-laser generating a single-longitudinal mode at a wavelength of 514.5 nm. To enable the subsequent attenuation of the pump by an iodine chamber, an additional Fabri-Perot interferometer was placed in the laser resonator, separating one longitudinal mode and significantly reducing the spectral width of the generation so that it does not exceed the spectral band of the absorption line of the iodine cell. The radiation power of one longitudinal mode was about 100 mW. To rotate the polarization of the pump we used a λ/2 plate. Heated up to temperature of 75°C an iodine vapor cell has many absorption lines near the generation frequency of the argon laser, so an iodine cell was used to filter the pump radiation. The signal radiation is eight orders of magnitude weaker than the pump radiation and is shifted from the pump frequency by 0.1-7 THz, so the use of an iodine cell makes it possible to detect the frequency-angular spectrum of the signal radiation

without the parasite background of the laser pump. Using a system of three lenses, the signal radiation was focused on the entrance slit of the MDR-41 monochromator. CCD-camera Proscan HS-101H with a Hamamatsu matrix recorded resulting interference patterns; the size of one pixel of the matrix was 24 microns.

Calculated and measured frequency-angular spectra are shown in Fig.3, one can see a good agreement between them. We suppose, that interferometry of optical-terahertz biphoton fields in the scheme of the Mach-Zehnder can be used as a method of spectroscopy for various substances in the terahertz range.
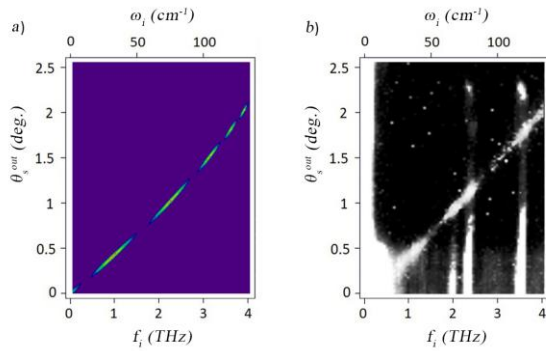
Fig. 3. a) calculated frequency-angular spectrum, b) experimental frequency-angular spectrum

References

1. *Chekhova M.V. and Ou Z.Y.* Nonlinear interferometers in quantum optics // *Advances in Optics and Photonics.* 2016. V. 8. No. 1. P. 104-155.

2. *A.V. Burlakov, Yu.B. Mamaeva, A.N. Penin, M.V. Chekhova* Three-wave interference with participation of polaritons// *J. Exp. Theor. Phys.* 2001. v.93. p.55

3. *Korystov D.Y., Kulik S.P., Penin A.N.* Rozhdestvenski hooks in two-photon parametric light scattering //, *JETP Letters.* 2001. V. 73, No. 5, P. 214-218.

4. *Korystov D.Y., Kulik S.P., Penin A.N.* Interferometry of spontaneous parametric light scattering // *Quantum Electronics.* 2000. V.30, P.922-926.

5. *Kalashnikov D.A., Paterova A.V., Kulik S.P., Krivitsky L.A.* Infrared Spectroscopy with Visible Light // *Nature Photonics.* 2016. V.10, P.98-102.

6. *Kuznetsov K.A., Kitaeva G.Kh, Kovalev S.P., Germansky S.A., Buryakov A.M., Tuchak A.N., Penin A.N.* Complex extraordinary dielectric function of Mg-doped lithium niobate crystals at terahertz frequencies // *Applied Physics B: Lasers and Optics.* 2016. V. 122. P. 223-232.

Terahertz Range Surface-Wave Bragg Resonators with Optimized Ratio between Ohmic and Radiative Losses

Andrey M. Malkin, N.S. Ginzburg, S.E. Fil'chenkov, A.S. Sergeev, and V.Yu. Zaslavsky

Institute of Applied Physics RAS, Nizhny Novgorod, Russia, malkin@appl.sci-nnov.ru

Finite grating area at the surface of a metal plate can form a highly selective surface-wave Bragg resonator which can be used for sensing in the THz range, among other applications [1]. For 1D and 2D structures, we describe surface modes confined at a metallic plate. For a given material conductivity and grating dimensions, an optimum corrugation depth can be determined that provides the maximum value of the fundamental mode quality factor due to the interplay between radiative and Ohmic losses.

Surface electromagnetic waves confined at the interface of metal and dielectric have been widely studied [2] since they possess a number of unique features making them useful for various applications, including antenna applications Raman scattering, etc. Since the evanescent waves are decelerated, Cherenkov devices based on interaction of electron beams with surface modes of the corrugated structures is of special interest in the short wavelength radiation bands, including the terahertz band [3]. These devices allow to solve the problem of longitudinal and transverse mode selection in oversized electrodynamical systems.

In this paper, we consider a periodically corrugated section of a metallic plate as a surface-wave resonator (see Fig.1) in a dielectric media with a permittivity of ε. We obtain the equations of wave coupling with Ohmic losses taken into account and derive an integral equation describing the eigenmodes. Based on this equation, we find the optimum values of the corrugation depth providing the maximum Q factor of the fundamental mode dependent on the ε. We also discuss the 2D variant of a surface-wave resonator.
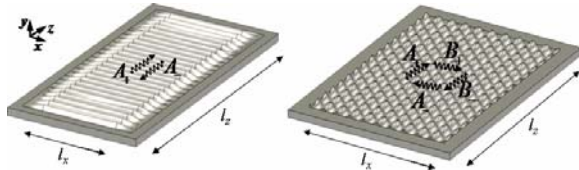

Fig. 1. 1D (left) and 2D (right) surface-wave resonators.

In the case when the depth of sinusoidal corrugation $b(z) = (b_0 / 2)\cos \overline{h}z$ is small in the scale of wavelength and of the structure period d the electromagnetic field of the surface mode existing near the 1D corrugated metal plate can be presented as a sum of two quasi-optical wavebeams with slowly varying amplitudes $A_{\pm}$ which can be characterized by the magnetic field

$$H_x = \mathrm{Re}\left[A_{+}\left(z, y, t\right)e^{i\left(\omega_0 t - h_0 z\right)} + A_{-}\left(z, y, t\right)e^{i\left(\omega_0 t + h_0 z\right)} \right],$$

where $h_0 = \overline{h} / 2$, $\omega_0 = c\varepsilon^{-1/2}h_0$ is the Bragg frequency. Propagation of electromagnetic field in the vicinity of the Bragg resonance can be described by a system of coupled parabolic wave-beam equations which take into account the diffraction in y direction [2],

$$\pm \frac{\partial A_{\pm}}{\partial z} + \sqrt{\varepsilon}\frac{\partial A_{\pm}}{c\partial t} + \sigma\delta(y)A_{\pm} + \frac{i}{\overline{h}}\frac{\partial^2 A_{\pm}}{\partial y^2} = i\alpha\delta(y)A_{\mp} \quad (1)$$

At the edges of the corrugation we set non-reflection boundary conditions: $A_{+}(z = 0) = 0$, $A_{-}(z = l_z) = 0$. Here $\alpha = \overline{h}b_0 / 8$ is the coupling parameter, $\delta(y)$ is the delta function. Parameter $\sigma = \sqrt{i / 2}\varepsilon k d_{skin}$ describes the Ohmic losses in the metal corresponding to the Leontovich boundary condition, d_{skin} is the skin depth of the metal.

Equations (1) applied to a system infinite in z direction lead to the existence of a surface wave $A_{\pm} \sim e^{i\Gamma z - g_{\pm}y + i\Omega t}$ with a dispersion law which in the lossless case can be put down as

$$\varepsilon\left(\frac{\Omega}{c}\right)^2 - \Gamma^2 = \overline{h}^2\alpha^4 \quad (2)$$

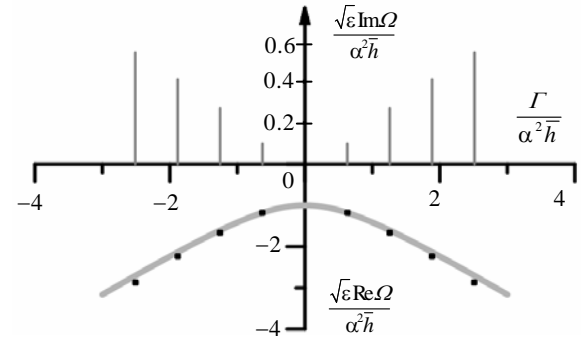Dispersion characteristic corresponding to (2) is shown in the lower part of Fig. 2.

Fig. 2. Dispersion curve of the surface wave. Dots mark the surface-wave resonator modes at $\alpha^2\overline{h}l_z = 5$, lines in the upper part indicate the losses of these modes.

In the case when the length l_z of the structure is finite, a set of longitudinal modes can be found. Seeking modes of (1) at an eigenfrequency of Ω, and using the Fourier transform, one can obtain an integral equation equivalent to system [5] which possesses an infinite discrete eigenmode spectrum. Frequencies and spatial profiles of eigenmodes can be found numerically. Real parts of the eigenfrequencies of the first several modes are marked with dots close to the dispersion in lower part of Fig.2 for $\alpha^2\overline{h}l_z = 5$ while the imaginary parts of these modes are shown as vertical lines in the upper part of the same figure. It can be seen that the $\mathrm{Im}\,\Omega$ increases almost linearly. Quality factor $Q = \omega_0\left(2\,\mathrm{Im}\,\Omega\right)^{-1}$ of the fundamental mode is about 3 times higher than that the next (second mode). It demonstrates the high selective properties of

55

surface wave resonator. Making use of the fact that according to the exact solution of (3), the longitudinal field structure of the mode tends to sine shape with increasing parameter $\alpha^2 \overline{h} l_z$, an asymptotic formulas for the fundamental mode eigenfrequency and Q factor can be obtained in the following form:

$$\text{Re}\,\omega_1 \approx \frac{c\overline{h}}{\sqrt{\varepsilon}}\left(\frac{1}{2}-\alpha^2\left(1+\frac{2\pi^2}{\alpha^4 \overline{h}^2 l_z^2}\right)\right) \qquad (3)$$

$$Q = \frac{1}{Q_{diff}^{-1}+Q_{Ohm}^{-1}}, Q_{diff}=\frac{\alpha^4 \overline{h}^3 l_z^3}{5\pi^2};\ Q_{Ohm}=\frac{2}{\alpha\,Re\,\sigma}$$

Note the sensitivity of the eigenmode position to the value of ε. According to (3), the precision of dielectric sensing by such structure can be roughly estimated as Q^{-1}. It is important that the two Q terms in (3) demonstrate different behavior at varying parameter α that is proportional to the corrugation depth b_0. Total Q factor has a maximum in its α dependence for each l_z. This maximum can be found from expressions (4) as

$$Q_{max}=\left(\frac{2^4}{5^6\pi^2}\frac{l_z^3}{\overline{h}\varepsilon^4 d_{skin}^4}\right)^{1/5} \approx 0.16\frac{l_z^{3/5}}{\overline{h}^{1/5}\varepsilon^{4/5}d_{skin}^{4/5}}$$

reached at

$$\alpha_{opt}=\left(\frac{10\pi^2}{\overline{h}^4 l_z^3 \varepsilon d_{skin}}\right)^{1/5} \approx \frac{2.5}{\overline{h}^{4/5}l_z^{3/5}\varepsilon^{1/5}d_{skin}^{1/5}}. \qquad (4)$$
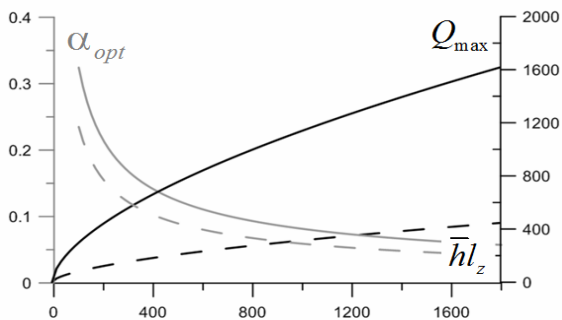
Fig. 3. Optimal α (gray) and maximum Q (black) and vs. length of the resonator. Solid lines correspond to copper structure in vacuum, dashed lines correspond $\varepsilon = 5$.

The optimum Q and α values vs. length of the resonator are depicted in Fig.3 for a structure with a Bragg frequency of about 1 THz (d=150 μm) made of copper ($d_{skin} \approx 0.065\ \mu m$) for a structure in vacuum (solid lines) and in a dielectric with $\varepsilon = 5$. According to (4), in this parameter area the small corrugation approximation is validated for structures of several dozen periods or longer. For instance, for a structure with a length of 100 periods ($\overline{h}l_z \approx 630$, see dotted line in Fig.5), a corrugation depth of 1/10 wavelength provides an optimal Q factor of about 1000 for copper at normal temperature. In a dielectric with $\varepsilon = 5$, Q value is much lower while the optimum corrugation depth remains almost the same.

Theory of 1D surface-wave resonators given above is applicable only at moderate (in the sense of Fresnel scales) transverse (x) sizes of the system, as it describes, in fact, a single transverse mode approximation. At larger x-dimensions of the system, various transverse modes with close Q factors would compete with each other. In [5], 2D surface-wave resonators were introduced to provide a means for synchronization of radiation from wide electron beams into the evanescent wave. For a 2D resonator (see Fig.1) with a corrugation of

$$l(z,x)=l_{2D}/4\left[\cos(\overline{h}_{2D}(z-x))+\cos(\overline{h}_{2D}(z+x))\right],$$

we use the time-domain simulation to find the fundamental mode. In this case, four partial quasi-optical wave-beams take part in formation of a surface mode, two of which ($A_{\pm}$) are propagating in $\pm z$ directions and the other two ($B_{\pm}$) are propagating in $\pm x$ directions. For 2D Bragg structures, Bragg frequency and wavenumber are defined as $\omega_0 = ch_0, h_0 = \overline{h}_{2D}$.

Wavebeam coupling is described by the following system of equations [5]:

$$\pm\frac{\partial A_{\pm}}{\partial z}+\frac{\partial A_{\pm}}{c\partial t}+\sigma\delta(y)A_{\pm}+\frac{i}{2k}\frac{\partial^2 A_{\pm}}{\partial y^2}=i\alpha_{2D}\delta(y)(B_{+}+B_{-}),$$

$$\pm\frac{\partial B_{\pm}}{\partial x}+\frac{\partial B_{\pm}}{c\partial t}+\sigma\delta(y)B_{\pm}+\frac{i}{2k}\frac{\partial^2 B_{\pm}}{\partial y^2}=i\alpha_{2D}\delta(y)(A_{+}+A_{-}).$$

Here $\alpha_{2D}=\overline{h}_{2D}l_{2D}/8$. To complete the 3D non-stationary model, we also set an "ideal metal" condition $\partial A_{\pm}/\partial y=0, \partial B_{\pm}/\partial y=0$ at some point $y=l_y$ with l_y much larger than the scale of decay of the fields. These equations were simulated with random initial conditions set at t=0 for the parameters of $\alpha_{2D}^2 h_0 l_z=4.4, \alpha_{2D}^2 h_0 l_x=3.14$. In simulation, a single mode with highest quality factor survived at $\alpha_{2D}^2\omega_0 t>100$. This fundamental mode is confined at the corrugation and possesses a bell-shaped structure in (z-x) plane. Q factor of this mode is about $15\alpha^{-2}$. Thus we have shown that a 2D surface-wave resonator with shallow corrugation is a highly selective structure with respect to three coordinates.

References

1. B. Ng, J. Wu, S.M. Hanham, et al., Spoof Plasmon Surfaces: A Novel Platform for THz Sensing // Advanced Optical Materials 1(8), 2013.

2. W.L. Barnes, A. Dereux, and T.W. Ebbesen, Surface plasmon subwavelength optics // Nature, v. 424, pp. 824–830, 2003.

3. N.S. Ginzburg, A.M. Malkin, A.S. Sergeev, V.Yu. Zaslavsky, Quasi-optical theory of relativistic submillimeter surface-wave oscillators // Appl. Phys. Lett. 2011, v. **99**, p. 121505.

4. N.S. Ginzburg, A.M. Malkin, A.S. Sergeev, V.Yu. Zaslavsky, Powerful surface-wave oscillators with two-dimensional periodic structures // Appl. Phys. Lett. 2012, v. **100**, p. 143510.

5. N.S. Ginzburg, A.M. Malkin, A.S. Sergeev, S.E. Fil'chenkov, V.Yu. Zaslavsky, "Highly selective surface-wave resonators for terahertz frequency range formed by metallic Bragg gratings", // Phys. Lett. A, v. 382, p. 925, 2018.

Study of influence of densification on control of conductivity and spectral characteristics of thin films of carbon nanotubes in terahertz frequency range

P. Demchenko[1], D. Gomon[1], I. Anoshkin[1,2], S. Smirnov[2],
D. Lioubtchenko[1,2], M. Khodzitsky[1]

[1]Department of Photonics and Optical Information Technologies, ITMO University, Saint Petersburg, Russian,
pert.s.demchenko@gmail.com
[2]Department of Micro and Nanosystems, KTH Royal Institute of Technology, Stockholm, Sweden.

The terahertz (THz) frequency range has a large number of potential applications. Terahertz radiation interacts with rotational and vibrational transitions of organic molecules, thus, this one can be used for spectroscopy of small organic molecules, for example glucose [1], water [2], macromolecules, cells [3], biological _tissues and medicines is possible. Also, the terahertz frequency band can be used in quality control of electrical circuits, drugs and product, astronomy, security systems and communications [4].

Each application requires components for generation, detection, polarization, amplification, and modulation of terahertz radiation. Currently, devices are being developed, the parameters and properties of which can be controlled. Several materials are capable of changing the properties and characteristics in the terahertz frequency range one of them is single-walled carbon nanotubes (SWCNTs). So, in our last article [5] we showed that the complex dielectric permittivity of a thin film of carbon nanotubes under the influence of optical pumping varies in the terahertz frequency range. Such thin layers of nanostructures readily absorb various liquids. Therefore, such samples can be processed in various ways. One of them is densification. This is the process of compacting the material. In this paper, we investigated the optical properties of thin SWCNT layers before and after densification, and how the optical properties change under the influence of infrared pumping at wavelength of 980 nm.

SWCNT film was made by chemical vapor deposition (CVD) [6] on nitrocellulose filter. This film was examined with scanning electron microscope (SEM) (Fig. 1(a)) and transmission electron microscope (TEM) to determine dispersion of length of nanotubes, their diameter and film's thickness.
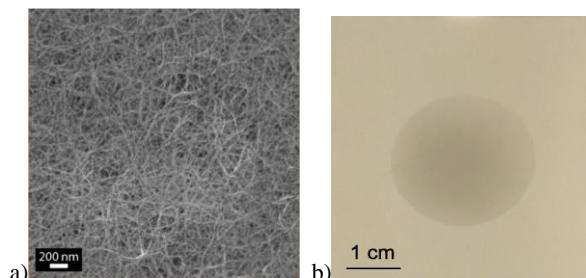

Fig. 1. a) Sample image of a SWCNT film obtained using a scanning electron microscope, b) Photo of sample

Characteristics of SWCNT film:

Nanotubes's length	~15 um
Diameter of nanotubes	1.3 – 2 nm
Film's thickness	55 nm

After that, SWCNT film was moved on teflon (PTFE) substrate with thickness of 350 um (Fig. 1(b)). The sample was studied using terahertz time-domain spectrometer (THz-TDS) [7] with additional 980 nm infrared laser for optical pumping (up to 0.7 W/cm^2). Scheme of THz-TDS is shown in Fig. 2.
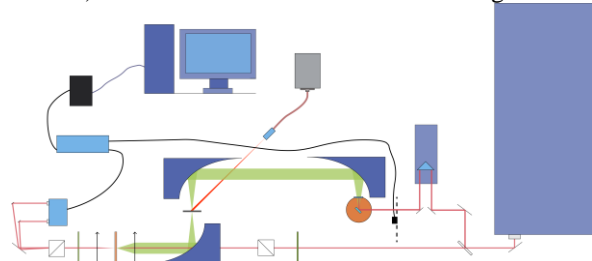
Fig. 2. Scheme of THz-TDS

THz waveforms were obtained before densification and after, with and without optical pumping (Fig. 3).
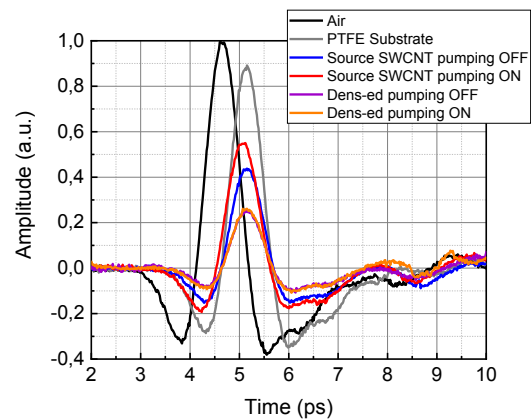

Fig. 3. Typical THz waveforms

To calculate a complex conductivity of the sample, the thin-film method [8] was used

$$\hat{\sigma}(f) = \frac{1}{Z_0}\left(\hat{n}_{Sub}(f)+1\right)\left(\frac{\hat{E}_0(f)}{\hat{E}(f)}-1\right), \qquad (1)$$

were Z_0 – impedance of free space, f - frequency, n_{Sub} – refractive index of substrate, $\hat{E}_0(f)$ and $\hat{E}(f)$ – the Fourier transforms of the detected THz wave

transmitted through the SWCNT layer on the PTFE substrate, and the PTFE alone, respectively.

Spectra of complex conductivity calculated by the formula (1) are shown in Figure 4.

a)

b)
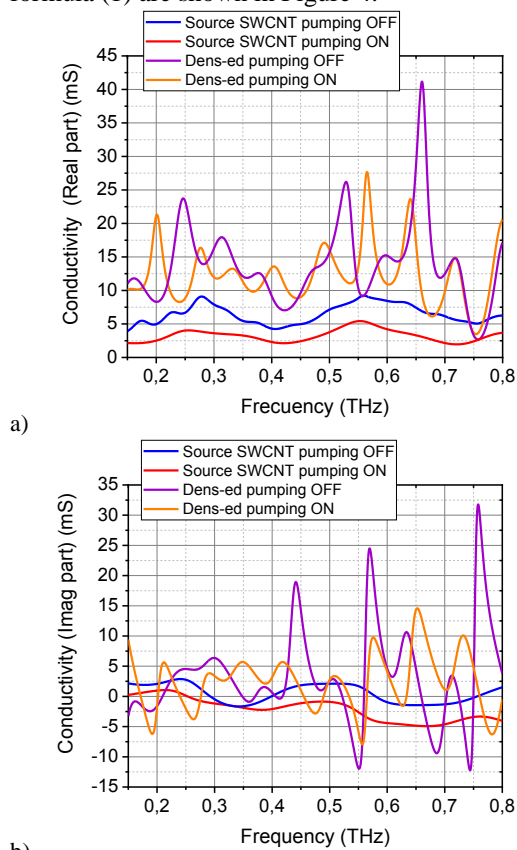
Fig. 4. Real part (a) and Imaginary part (b) of complex conductivity of thin-film SWCNT

The sample before densification has the effect of changing the complex conductivity (as in article 4). One explanation for this effect is that the nanotubes in the original sample are relatively free of each other, like "wool." Upon irradiation of a sample, the SWCNT oscillates more strongly; therefore, the contact area between adjacent nanotubes decreases and the conductivity of the sample decreases. During the process of densification the distance between the nanotubes decreases, the overall density of the film increases, hence the contact area between the tubes increases and the conductivity increases. This is confirmed in our work. After densification, the conductivity increased and does not change upon optical pumping. In addition, peaks appeared on the spectra after sample processing, presumably due to the uneven compaction of a thin-film and a decrease in the signal-to-noise ratio for densified sample.

According to the result of the work, it was obtained that after densification, the sample began to pass less (increased losses / increased the real part of the conductivity), the real part of the refractive index slightly increased. At the same time, the ability to control explicitly is almost imperceptible. This can be used in terahertz antennas and integrated circuits for the terahertz frequency range, where part of the nanotubes are densified to attenuate control by optical pumping.

References

1. *Gusev S., Demchenko P., Cherkasova O., Fedorov V., Khodzitsky M.* Influence of Glucose Concentration on Blood Optical Properties in THz Frequency Range // Chinese Optics 2018. V 11. No. 2. P. 182–189.

2. *Borovkova M., Khodzitsky M., Demchenko P., Cherkasova O., Popov A., Meglinski I.* Terahertz time-domain spectroscopy for non-invasive assessment of water content in biological samples // Biomedical Optics Express 2018. V. 9. No.5. P. 2266.

3. *Borovkova M., Serebriakova M., Fedorov V., Sedykh E., Vaks V., Lichutin A., Salnikova A., Khodzitsky M,* Investigation of terahertz radiation influence on rat glial cells // Biomed. Opt. Express, BOE 2017. V. 8. No. 1. P. 273–280.

4. *Federici J., Moeller L.* Review of terahertz and subterahertz wireless communications // Journal of Applied Physics 2010. V. 107. No. 11. P. 111101.

5. *Smirnov S., Anoshkin I., Demchenko P., Gomon D., Lioubtchenko D., Khodzitsky M., Oberhammer J.* Optically controlled dielectric properties of single-walled carbon nanotubes for terahertz wave applications// Nanoscale 2018. V. 10. No.26. P. 12291–12296.

5. *Anoshkin I., Nasibulin A., Tian Y., Liu B., Jiang H., Kauppinen E.* Hybrid carbon source for single-walled carbon nanotube synthesis by aerosol CVD method // Carbon 2014. V. 78. P. 130–136.

6. *Bespalov, V., Gorodetskiĭ, A., Denisyuk, I., Kozlov, S., Krylov, V., Lukomskiĭ, G., Putilin, S.* Methods of generating superbroadband terahertz pulses with femtosecond lasers //Journal of Optical Technology. 2008. V. 75. No. 10. P. 636-642.

7. Tinkham M. Energy Gap Interpretation of Experiments on Infrared Transmission through Superconducting Films // Physical Review 1956. V. 104. No. 3. P. 845–846